Design of a miniaturised diode laser with integrated frequency stabilisation

by

Janka Söhn

Bachelor thesis in physics
presented to the faculty of physics, mathematics and computer science (FB 08)
at the Johannes Gutenberg-Universität Mainz
August 2, 2021

1st Examiner: Prof. Dr. Patrick Windpassinger
2nd Examiner: Prof. Dr. Klaus Wendt

ABSTRACT

Frequency-stabilised lasers are widely used in modern scientific experiments, with applications ranging from spectroscopy, optical clocks, and even fundamental physics and physics beyond the standard model. For example, the space experiments conducted by the QUANTUS (Quantengase Unter Schwerelosigkeit) project use frequency-stabilised lasers to perform research in the field of ultra-cold atoms and Bose-Einstein condensates. The aim of this thesis is to design and characterise a frequency-stabilised laser module of a compact size for applications in which portability is required. This module can then be used for testing the hardware in the collaborating universities. We use saturated absorption spectroscopy to stabilise the laser frequency onto hyperfine structure atomic transitions, which are used in the experimental procedure to generate ultra-cold atoms, Bose-Einstein condensates, and for interferometry. We take measurements for different frequency modulation spectroscopy and modulation transfer spectroscopy setups. By comparing the occurring error signals, as well as the power and spacial requirements, we optimise the frequency stabilisation, which is then implemented into the design of the miniaturised setup. The design is generated using the computer-aided design software Autodesk Inventor. The miniaturised setup is divided into two different modules: one containing the fibre-coupled laser, and another containing the spectroscopy setup and additional electronics. This was chosen, instead of one module containing all components, for operational flexibility. Limitations of the experimental setup are discussed and an outlook for future applications is given.

Declaration of Authorship

I hereby assure, that I wrote this thesis myself. I did not use any other sources than the ones indicated and that quotes are referred to as such.

Mainz, August 2, 2021[Signature]

Janka Söhn
AG QOQI
Institute of physics
Staudingerweg 7
Johannes Gutenberg-Universität D-55128 Mainz
jsoehn@students.uni-mainz.de

Acknowledgements

As I would not have been able to accomplish this work all by myself, I would like to thank everybody involved for their contribution:

I would especially like to thank Prof. Dr. Patrick Windpassinger for giving me the opportunity to write this thesis in the QOQI research group, for answering upcoming questions and for his great flexibility and understanding regarding the unusual current circumstances.

I also want to thank Prof. Dr. Klaus Wendt for kindly agreeing to be second examiner.

Furthermore, I would like to thank Sören Boles and André Wenzlawski for the great mentoring. I really appreciate that I was always able to ask even to dumbest questions and that any problem was immediately tried to be solved. Thank you for the help in the lab, the proofreading and all the helpful comments and advice.

Thanks also to Sören Boles, Ishan Varma, and Parvez Islam for the nice company in the office in the lately very empty university and the shared lunch times.

I would like to thank Marina Gil Sendra and Román Frutos Picazo for their constant help in improving this work, for all the general physics advice throughout the years and simply for being part of my life.

Thanks to Joseph A. Smiga and James Eills for a last-minute proof-reading.

I want to thank my friends and fellow students, without whom I would not have been able to get through the last four years. Thank you for all the professional and emotional support, for making long afternoons spent in the faculty more fun and for every survived exam period.

Last but not least, I want to thank my family who always supported me, and my friends for having my back, standing my moods in stressful times and for always being there for me.

Contents

1. Introduction

In many scientific fields it becomes more and more important that experimental setups are not only conducted in controlled experimental conditions but also, that the equipment can be used in field applications. To accomplish this, the experimental setups need to be optimised in a way such that they meet different requirements, such as portability, high mechanical stability, and manageable size. For example, the federal institute for physics and technology, the PTB (Physikalisch-Technische Bundesanstalt), was able to build the most accurate and stable portable optical clock in the world [1]. The scientists managed to design and construct the experimental setup of an optical clock in the size of a car trailer. With this, time measurements with a systematic uncertainty of 7.4×10^{-17} can be performed in different locations. This has profound implications for the field of geodesy, and for Global Positioning Systems (GPS).

The QOQI (Experimental Quantum Optics And Quantum Information) research group at the Johannes Gutenberg Universität Mainz is part of the QUANTUS (Quantengase Unter Schwerelosigkeit) project together with six other German universities [2]. This project is focused on studying physical phenomena in micro-gravity environments, such as the generation of ultra-cold atoms and Bose-Einstein condensates. The hardware for these experiments first needs to go through rigorous testing in ground-based laboratories. As the collaboration between the different universities is based on cooperation and collective research, scientists frequently need to visit research groups of the other collaborating institutes. For that, the necessary equipment has to be packed and transported between the cooperation faculties. The aim of this work is to provide a convenient alternative version of a frequency-stabilised fibre-coupled diode laser which can be easily taken to different locations. It was designed to simplify packing and transport issues and to ensure high mechanical stability and simple readjustment of the diode laser with high stability in terms of frequency.

We design the portable diode laser to stabilise onto an atomic transition, i.e. onto a hyperfine transition in Rubidium (Rb), at a wavelength around 780 nm. We choose this wavelength because the QUANTUS collaboration uses Rubidium for many of their projects, such as the MAIUS-1 (Materiewellen Und Interferrometrie Unter Schwerelosigkeit) project which created a Bose-Einstein condensate and performed atom interferometry aboard a sounding rocket (launched January 2017) with Rubidium-87 atoms [3]. An introduction into the atomic structure of ^{85}Rb and ^{87}Rb is given in section 2.2.

We use a distributed feedback laser in a saturated absorption spectroscopy setup to achieve the frequency-stabilisation in the miniaturised design. The choice of this laser type is motivated in section 2.1. The necessity, the working principle and the experimental setup for saturated absorption spectroscopy are demonstrated in section 2.3. We discuss how we can use the technique of frequency modulation to stabilise our laser system onto a certain frequency in section 2.4.

Various methods can be used to obtain a frequency-stabilised laser source using saturated absorption spectroscopy. The most elaborate approaches are modulation transfer spectroscopy, frequency modulation spectroscopy, and an alternative operation mode for the latter that employs retroreflection. We evaluate the performance of these three spectroscopic techniques experimentally for the determination of the spectroscopy method which will optimise the frequency stabilisation in the miniaturised version in terms of functionality and spacial requirements. First, the tested spectroscopy methods are introduced in section 2.5, followed by a description of the experimental setups in section 3.1. In section 3.2 we present the results from the different measurements and justify why we decided to implement a retroreflective frequency modulation spectroscopy setup into the design for the miniaturised laser module. We ensure that the chosen method for the frequency stabilisation works in the laboratory frame in section 3.3 and discuss why this should work for the miniaturised design accordingly.

In the last part of this work, the miniaturised design is presented. It consists of two modules, one containing the diode laser output coupled into two optical fibres: one for the spectroscopy module and one to be used for the main experiment. The second module contains the spectroscopy instrumentation and additional electronics. These modules can be connected by an optical single-mode fibre to transmit the laser light from the fibre-coupled laser module into the fibre-coupled spectroscopy module. The spectroscopy module generates an error signal which is used to stabilise the laser frequency by feeding it back to the laser module. The laser box can be tuned to feed all the light into one optical fibre and, therefore, provide a portable fibre-coupled laser source where high frequency stability is not required. In this case, the spectroscopy module can simply be omitted. The size of the modules was chosen to accomodate commercial products, to keep the costs to a minimum while ensuring minimum dimensions of the modules for convenience. This is discussed in section 4.

The thesis will be concluded by discussing the limitations of the design, ideas of further improvements and possible alternatives, in section 5.

The final design provides a stable fibre-coupled frequency-stabilised laser source which does not exceed the size of a shoebox and could therefore be used for the named purposes.

2. Theoretical background and methods

In order to understand the working principle of the laser frequency stabilisation using spectroscopy, the most important physical phenomena behind it will be described here. First, we will give an introduction on diode lasers, followed by an explanation on the importance of the hyperfine structure of atoms for this thesis. Then, saturated absorption spectroscopy and the process of the laser frequency stabilisation will be discussed. The theory part will be concluded with the different kinds of spectroscopy methods that will be tested in section 3.

2.1. Basic working principle of diode lasers

In the experiments and in the final design we will be using light coming from a diode laser. While in the experimental setup an external cavity diode laser will be used, in the miniaturised version a distributed feed-back laser will be implemented. In this section we will give a short overview of the working principle behind both diode laser types and the reasons behind choosing a distributed feedback laser over an external cavity diode laser for the miniaturised setup.

2.1.1. Laser diode

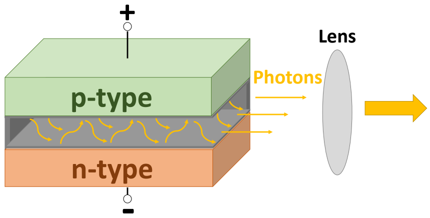

Figure 2.1.: Basic working principle of a diode laser. Photons are generated by the p-n-junction when applying voltage to the semiconductor plates. They multiply by stimulated emission until leaving the diode through the lens for collimation.

The basic working principle of a diode laser is shown in Figure 2.1. It consists of a laser diode and some collimating optics. A laser diode is a semiconductor device which produces laser light by accumulating photons with the same frequency, phase, and direction [4]. This is achieved by putting a block of a p-doped material on top of a block of a n-doped material seperated by an additional intrinsic layer, the so-called active region. A n-doped material is a semiconductor with additional weakly-bound <u>n</u>egative charged electrons, while a p-doped material shows additional holes, representing weakly-bound <u>p</u>ositive charges. When applying a voltage across the two blocks, a p-n-junction is generated inside the active region, releasing photons of similar frequency. The wavelength of the photons depends on the particular material of the two terminals and the layer in between, and can be regulated by changing the temperature and the input current. In order to produce laser light, mirrors are placed at the edges of the p-n-junction so that the photons are reflected inside and stimulate more photons. They accumulate inside the active region and can only exit the laser diode in one direction. In order to collimate the light into one narrow beam, a converging lens is needed before the exit. Typically, several longitudinal modes are observed simultaneously, resulting in low coherence and broad linewidths.

2.1.2. External cavity diode lasers (ECDL)

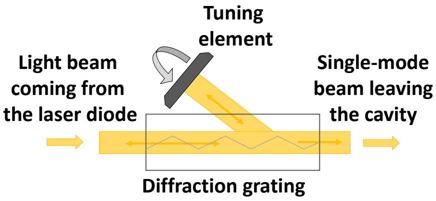

Figure 2.2.: Possible configuration of a cavity in an external cavity diode laser [5].

An external cavity diode laser (ECDL) consists of a laser diode and an external cavity which contains wavelength-selective optics. Figure 2.2 shows one possible cavity configuration, i.e. a modified Littman-Metcalf configuration [6]. The laser beam, consisting of several modes, hits a diffraction grating. By rotating the tuning element, the wavelength is adjusted and by that a single mode is extracted [5]. This is realised by adding an input to the ECDL which changes the position of the piezoelectric tuning element by using the effect of piezoelectricity. This setup relies on the piezoelectric effect wherein certain materials deform when applying voltage to them.
The advantages of an ECDL lie in its high resolution and long term operations [7], which makes it the favoured choice for our experiments performed in section 3.

2.1.3. Distributed feedback laser (DFB)

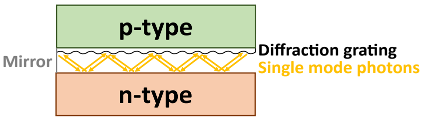

Figure 2.3.: Schematic of a distributed feedback laser. The diffraction grating it tuned in a way that single-mode photons are reflected. Through stimulated emission these photons are multiplied in the active region [8].

In a distributed feedback laser (DFB) part of the active region of the photodiode consists of a diffraction grating consisting of a periodically structured material. The period of these structures is chosen to only reflect a narrow band of wavelengths. By this they generate a single laser mode and, therefore, create the optical feedback of the laser [9]. As a result, DFB lasers have a small spectral bandwidth with deviations in the order of 10^{-7} [10].
We decided to implement a distributed feedback laser into our design of the miniaturised, portable setup. This decision is based on the high robustness of the DFB laser, due to the absence of alignment-sensitive optical components [11].

2.2. Atomic properties and processes

This section is based on Ref. [4].

2.2.1. Energy levels

A bound quantum mechanical system, such as electrons bound to a nucleus by an attractive potential, has a discrete energy spectrum. The quantized energy states fulfill the Schrödinger equation:

$$i\hbar\frac{\partial}{\partial t}\left|\psi(t)\right\rangle = \hat{\mathcal{H}}\left|\psi(t)\right\rangle \quad \text{with} \quad \hat{\mathcal{H}} = -\frac{\hbar^2}{2m}\Delta + V(x), \tag{2.1}$$

where $|\psi(t)\rangle$ denotes the wavefunction at time t in the state ψ and $\hat{\mathcal{H}}$ the Hamilton operator in a potential V(x). For an atom which can be approximated by the hydrogen atom, the energy eigenvalues are given by

$$E_n = -\frac{e^2}{4\pi\epsilon_0}\cdot\frac{Z^2}{2a_0n^2}, \tag{2.2}$$

where e is the elementary charge, ϵ_0 denotes the permittivity in vacuum, Z is the atomic number of the nucleus, a_0 the Bohr's radius and n denotes the principal quantum number. As shown in Figure 2.4, the principal energy levels of electrons are described through orbits around the nucleus and can be labelled alphabetically starting with K closest to the nucleus. These shells correspond to the principal quantum number n = 1, 2, 3,... with $2n^2$ electrons per shell. The lowest possible energy level of an atom or molecule is called ground state. States with higher energies are called excited states. Every quantum mechanical state can be described by additional quantum numbers, like the angular momentum quantum number ℓ, the magnetic quantum number m$_\ell$ and the spin quantum number m$_s$. An overview of these quantum numbers is given in table 2.1. Due to different interactions of nucleus and electrons, the principal energy states can have different values if we take the interactions between them into account. The energy levels then can be split into several sublevels by considering different energy corrections, i.e. the fine structure and the hyperfine structure will be explained in a bit more detail now.

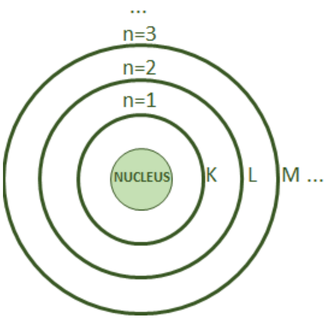

Figure 2.4.: Principal energy levels of an atom with n being the principle quantum number.

Number	Symbol	Possible values	Notation
Principal quantum number	n	1, 2,...	K, L, M,...
Angular momentum quantum number	ℓ	0, 1, 2, ...,(n-1)	S, P, D, F, G, H,...
Magnetic quantum number	m$_\ell$	-ℓ,...,ℓ	-
Spin quantum number	m$_s$	-s,-s+1,...,s-1,s	-

Table 2.1.: Overview of the principal quantum numbers.

2.2.2. Fine structure

The fine structure of the energy levels is due to spin-orbit coupling which is a relativistic kinetic energy correction:

$$\Delta E_{FS} = E_n \frac{Z^2 \alpha^2}{n} \left(\frac{1}{j+s} - \frac{3}{4n} \right), \tag{2.3}$$

with E_n being the energy of the energy level without considering spin-orbit coupling and α denoting the fine structure constant. There the orbital angular momentum ℓ and the spin angular momentum s couple and the spectral lines split into several levels. The energy levels will be a bit higher or lower depending on the kind of coupling. Here we introduce a new quantum number, the so-called total angular momentum quantum number $j = \ell \pm s$ defined within the interval $|\ell - s| \leq j \leq \ell + s$. As ℓ is usually represented by letters starting with s, p, d, f and then continues alphabetically, as described in table 2.1 we can use the spectroscopic notation and by that unambiguously assign a name to each level created by the spin-orbit-interaction: $n^{2s+1}L_j$.

2.2.3. Hyperfine structure

Selection rules

1. Δs = 0
2. Δl = 0,$\pm$1 but l = 0 $\not\rightarrow$ l´= 0
3. Δj = 0,$\pm$1 but j = 0 $\not\rightarrow$ j´= 0
4. $\sum_i$ l_i must change its parity

Table 2.2.: Overview of the quantum mechanical selection rules where s denotes the spin quantum number, l the angular momentum quantum number, j the total electron angular momentum quantum number [12].

The hyperfine structure of an atom is then further splitting of the energy levels due to interactions between the spin of the nucleus and the total angular momentum of the electrons. The quantum number of the nuclear spin I is defined by the total spin of its nucleons. The hyperfine structure is thus represented by introducing a new quantum number F which consists of the nuclear spin quantum number I and the total electron angular momentum j, so that $F = I + j$ with $|\ j\text{-}I\ | \leq\ F \leq\ j\text{+}I$. The additional energy correction is given by:

$$\Delta E_{HFS} = \frac{\hat{A}}{2} [F(F+1) - j(j+1) - I(I+1)], \tag{2.4}$$

with $\hat{A}$ being the hyperfine structure constant.
Only certain transitions are allowed and will actually take place. In order to find out which ones those are, we need to take into account the so-called selection rules. They can be briefly described by the rules presented in table 2.2. Discussing the derivation of these rules in detail would go beyond the frame of this work. See Ref. [13] for additional information.

2.2.4. Atomic structure of Rubidium

For the experiments and the final setup we will be using natural Rubidium gas inside a vapour cell. The natural abundance of Rubidium consists of 72.2% ^{85}Rb and

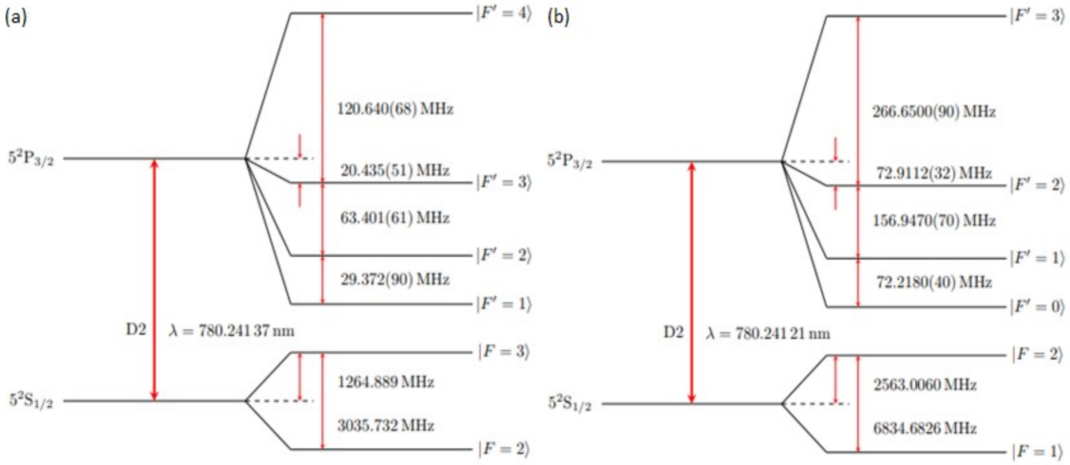

Figure 2.5.: Hyperfine structure of the Rubidium D2 line for (a) ^{85}Rb and (b) ^{87}Rb, taken from Refs.[14] and [15].

27.8% ^{87}Rb, where ^{85}Rb and ^{87}Rb denote Rubidium isotopes with the mass numbers 85 and 87. The ground state for both isotopes is the $5^2\text{S}_{1/2}$ level. Due to the fine structure (see section 2.2.2), the first excited state splits up into the levels $5^2\text{P}_{1/2}$ and $5^2\text{P}_{3/2}$, called the two D-lines: D1 and D2. We will only be looking at the wavelength of the D2 line which lies at a wavelength of around 780.241 nm. The hyperfine structure is determined as described in the previous section and is shown in Figure 2.5. Taking the selection rules into account, we expect the following transitions for the Rubidium D2 line:
$5^2S_{1/2}$ $(F = 2) \rightarrow 5^2P_{3/2}$ $(F' = 1, 2, 3)$ and $5^2S_{1/2}$ $(F = 3) \rightarrow 5^2P_{3/2}$ $(F' = 2, 3, 4)$ in ^{85}Rb and
$5^2S_{1/2}$ $(F = 1) \rightarrow 5^2P_{3/2}$ $(F' = 0, 1, 2)$ and $5^2S_{1/2}$ $(F = 2) \rightarrow 5^2P_{3/2}$ $(F' = 1, 2, 3)$ in ^{87}Rb [14, 15].

2.3. Atomic spectroscopy

Atomic spectroscopy is widely used to analyse atomic properties. In general, in absorption spectroscopy, photons from a light source, e.g. laser light, illuminates the sample. The light intensity for given frequencies is measured before and after passing through the gas and the two values are compared. Light absorption is commonly analysed using Beer's law:

$$dI = -\alpha I dL, \tag{2.5}$$

where dI is the intensity decrease of the intensity I caused by the propagation through a medium of length L and α denotes the absorption coefficient [16]. α is defined as the ratio of the intensity that was absorbed in the path of 1 cm ($\alpha = dI/I[\text{cm}^{-1}]$) and can therefore be used for the analysis of absorption spectra. This way, the energy that was absorbed by the gas atoms is analysed and, by tuning through a frequency range, possible energy transitions of the corresponding material can be determined [16]. We will also use the absorption coefficient in section 2.4.2 to obtain a quantitative description of the error signal. For regular absorption spectroscopy, we only have one laser beam passing through the probe, revealing part of its hyperfine structure, while in saturated absorption spectroscopy, the beam is split into a beam with high intensity ("pump beam") and a beam with lower intensity "probe beam") which enter the sample from opposite directions. This can result in a resolution high enough to resolve the further hyperfine structure of the gas as Doppler broadening is suppressed. This will be discussed in more detail in the following section.

2.3.1. Broadening phenomena

We will discuss the reasons why we chose to perform saturated absorption spectroscopy, also called Doppler-free absorption spectroscopy. For this we need to understand some broadening mechanisms of the spectrum.

2.3.1.1. Natural broadening

Natural broadening is a physical effect due to the Heisenberg uncertainty principle [4]. Here, it relates the uncertainty of the energy to the lifetime of an excited state due to spontaneous radiative decay and results in the broadening of an unshifted Lorentzian intensity profile

$$I(\omega) = I_0 \frac{\Gamma_N^2}{(\omega_0 - \omega)^2 + \Gamma_N^2}, \tag{2.6}$$

where ω denotes the frequency, I_0 the intensity amplitude at the transition frequency ω_0 and Γ_N the full width at half maximum (FWHM) of the distribution [16]. For instance, for Rubidium we find a natural linewidth of $\Gamma_N \approx 6$ MHz [17].
This effect is found in absorption spectroscopy as well as in saturated absorption spectroscopy.

2.3.1.2. Doppler broadening

The effect of natural line broadening can be intensified by the so-called Doppler broadening. As the name suggests this kind of broadening is caused by the Doppler effect which describes the frequency shift of a photon due to the relative velocity of an atom to the light field of the laser [4]. These Doppler shifts result in an inhomogeneously broadened Doppler spectral profile within the absorption spectrum and can be described by a Gaussian profile

$$I(\omega) = I_0 \, exp \left[-(\frac{c(\omega - \omega_0)}{\omega_0 v_p})^2 \right] \tag{2.7}$$

with c being the speed of light and v_p the most probably velocity group with $v_p = \sqrt{\frac{2k_BT}{A}}$, where k_B is the Boltzmann constant, T the absolute temperature and A the atomic mass of the absorbing atoms. It shows a FWHM of

$$\Gamma_D = \frac{2\omega_0}{c}\sqrt{2RTln(2)\frac{T}{A}}, \tag{2.8}$$

also referred to as the Doppler width [17], where R denotes the gas constant. At a transition frequency of $\omega_0 = 3.8 \cdot 10^{14}$ Hz (which corresponds to the wavelength $\lambda = 780$ nm) at room temperature ($T = 297$ K), for Rubidium, which will later be used in the experiments, the Doppler width will accordingly be 502 MHz.

This order of magnitude allows us to neglect the effect of natural line broadening (compare section 2.3.1.1) and is problematic when trying to use atomic properties for laser stabilisation. As the distances between the atomic transitions of the hyperfine structure levels in the D2 line of Rubidium show frequency values between 30 MHz and 270 MHz (see Figure 2.5), we are not able to distinguish them. Therefore, we need to use saturated absorption spectroscopy where this effect is suppressed which is why saturated absorption spectroscopy is also referred to as Doppler-free absorption spectroscopy [18, 19].

2.3.2. Saturated absorption spectroscopy (SAS)

This section in based on Refs. [18] and [20].

2.3.2.1. Working principle behind SAS

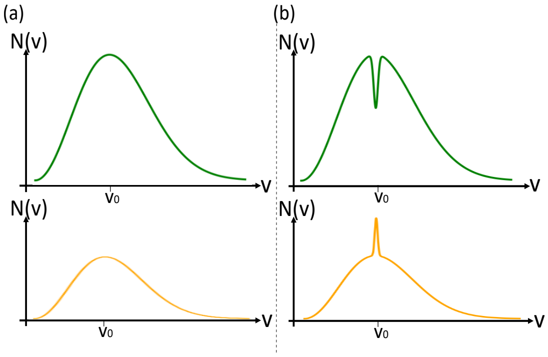

Figure 2.6.: (a) Maxwellian velocity distribution for a ground state (top) and an excited state (bottom), in (b) a laser beam passes through a gaseous sample at $\omega = \omega_0$ for a ground state (top) and an excited state (bottom).

Considering one laser beam passing through a gaseous sample, the number of atoms N(v)dv within the velocity range dv, also referred to as a velocity group, shows a Maxwell distribution with its maximum at v = 0. A Maxwell distribution, giving the probability density function, is defined as follows:

$$f(v) = \sqrt{\frac{2}{\pi}}\frac{v^2 \cdot exp(\frac{-v^2}{2a^2})}{a^3} \tag{2.9}$$

where v denotes the velocity and $a = \sqrt{m/k_BT} = \text{const}$. The corresponding populations, the number of atoms occupying a specific atomic state $|n\rangle$, are usually larger in the ground state $|0\rangle$ than in excited states $|1\rangle$. Figure 2.6a shows the Maxwell distribution for populations in a ground and an excited state. In

Figure 2.6b that distribution is modified by sending an additional laser beam with frequency $\omega = \omega_0$ through the sample. Only the velocity group at $v = 0$ interacts with the photons and therefore depopulates the ground-state distribution. This phenomenon is called “hole-burning”. If $\omega \neq \omega_0$, the atoms of the velocity group at $v = 0$ can not be excited into a higher state, but atoms moving relatively to the light can. Now SAS comes into play: at $\omega = \omega_0$ the pump beam interacts with the same velocity group ($v = 0$) as the probe beam. As the intensity of the pump beam is much higher, it depopulates this group, which results in less atoms in the ground state within that velocity group for the probe beam to excite. As a result, a sharp dip can be found in the absorption spectrum of the probe beam. Those dips are called Lamb dips and have a finite width, mainly due to natural line broadening. As described in section 2.3.1.1, for Rubidium this results in a linewidth of $\Gamma \approx 6$ MHz. As each level in the hyperfine structure corresponds to a certain transition frequency ω_0, Lamb dips occur at those levels. This allows us to measure the corresponding frequencies of the hyperfine structure. Later on we will use these frequencies for the laser stabilisation.
In Figure 2.7 we see the difference between the spectrum of the D2 line of Rubidium (a) using absorption spectroscopy and (b) using saturated absorption spectroscopy. In Figure 2.7a we are only able to see four (Doppler-broadened) peaks of the hyperfine structure while in Figure 2.7b we can see that lamb dips occur within each peak.

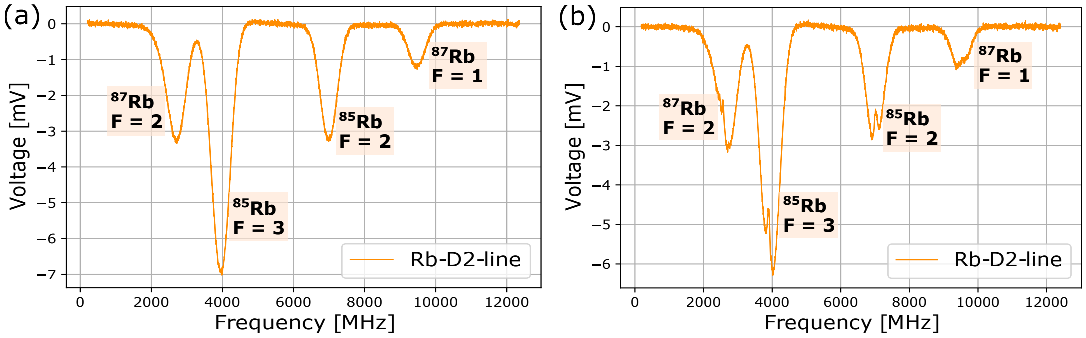

Figure 2.7.: (a) Absorption spectrum of the Rubidium D2 line obtained with a single beam passing through the probe, (b) Same absorption spectrum using saturated absorption spectroscopy.

2.3.2.2. Cross-over resonances

When looking at the saturated absorption spectrum of Rubidium we would expect to see one Lamb dip at each transition of the showing hyperfine levels as discussed in section 2.2.3. Accordingly, in each Doppler peak we would expect three Lamp dips to appear when switching to SAS, due to the selection rules which limit the possible transitions, specified in section 2.2.4. But we will see, when measuring the absorption spectra for Rubidium in section 3, that each absorption spectrum shows additional dips at frequencies that do not correspond to any transition frequency. They are explained by the so called cross-over resonances. When having two excited energy levels $|1\rangle$ and $|2\rangle$ with the resonance frequencies ω_1 and ω_2 less than a Doppler width apart, two Lamb dips will occur at those frequencies, as previously discussed. The crossover frequency appears exactly in the middle between those transition, at $\omega_{co} = (\omega_2 - \omega_1)/2$. At this frequency, the Doppler shift of pump and probe beam are of the same magnitude but in opposite direction. The depopulation of the pump beam and the absorption of the probe beam occur within the same velocity group, reducing the absorption, analogously to the formation of the lamb dips [21]. This behaviour is illustrated in Figure 2.8. As the cross-over dips originate from the same transition frequencies as the two corresponding Lamb dips, they are as stable and precisely determined. As a result, the laser can also be stabilised on a cross-over peak [16].

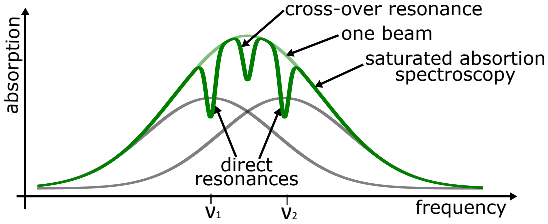

Figure 2.8.: Formation of cross over resonances, two Doppler distributions close to each other result in an additional peak. Performing saturated absorption spectroscopy results in an additional dip at that sum.

2.3.2.3. Experimental setup of SAS

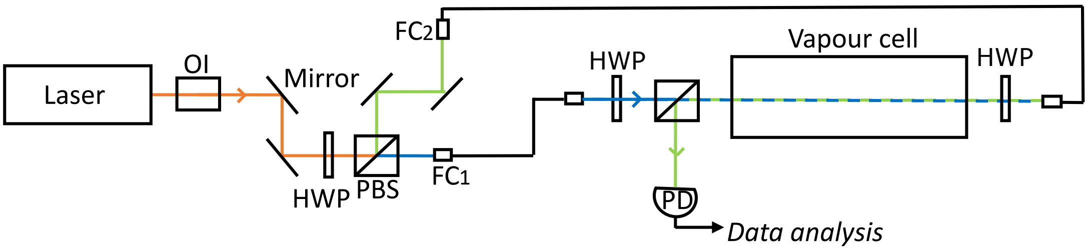

Figure 2.9.: Experimental setup for saturated absorption spectroscopy. OI: optical isolator, HWP: $\lambda/2$-wave-plate, PBS: polarising beam splitter, FC: fibre coupler, PD: photodiode, pump beam, probe beam.

Figure 2.9 shows the sketch of the setup for saturated absorption spectroscopy (SAS). The light is emitted from a laser (represented by the orange line) and passes through and optical isolator. An optical isolator is a device which allows light with certain polarisation to pass from only one direction and blocks it from the opposite direction. It is included in the setup to protect the laser from unwanted feedback. Its working principle is based on the Faraday effect. This effect describes a rotation of the polarisation plane of a linearly polarised electromagnetic wave in a magnetic field parallel to the direction of propagation [22]. The laser beam then hits two mirrors before passing through a $\lambda/2$-wave plate (HWP) onto a polarising beam splitter (PBS). The mirrors are used in order to precisely adjust the direction of the laser beam. The $\lambda/2$-wave plate allows us to change the polarisation of the electromagnetic wave and therefore set the ratio of how much light will be reflected/transmitted by the PBS. We choose the transmitted beam (indicated by the blue lines) to have 90% of the intensity and will therefore act as the pump beam. It is directly coupled into a fibre port (FC_1). The pump beam leaves the fibre passing through another $\lambda/2$-wave plate in order to fully transmit through the following PBS. After this, it enters a vapour cell where the gas atom will be excited by the photons. The pump beam will then leave the vapour cell and after this will not be of further interest. The part of the laser beam which is reflected at the first PBS (indicated by the green lines) hits two mirrors again in order to couple it into a fibre port (FC_2). It has around 10% of the intensity and therefore acts as our probe beam. It leaves the fibre passing through a $\lambda/2$-wave plate, followed by the vapour cell and a PBS. The polarisation is chosen in a way that the beam is fully reflected and hits a photo diode. A photo diode consists of a p-n-junction run in reverse bias. Thus, the n-doped material is connected to the positive voltage terminal while the p-doped material receives a negative voltage. With no radiation hitting the p-n-junction only a negligible current can be measured. When photons hit the depletion zone, a reverse saturation current, also called the photo current, starts to flow. The photo current is proportional to the intensity of the light and can be measured [4]. The information contained in the recorded beam can be used for further analysis.

2.4. Realisation of the laser stabilisation

This section is based on Refs. [23] and [24].

2.4.1. Qualitative explanation

We now show the working principle behind the laser frequency stabilisation for a frequency modulation spectroscopy setup. For clarity purposes, we describe the generation of the stabilised laser frequency using Doppler-broadened spectroscopy, as illustrated in Figure 2.10. It works equivalently for saturated absorption spectroscopy, which will be used in the sections 3 and 4, where the absorption spectrum of the probe beam will be analysed in the same way.

The idea of this frequency stabilisation method is to measure a signal, i.e. the absorption spectrum of a gaseous probe, and modify it to get a signal which we can feed into an electronics system to lock onto a specific value. This new signal, the so-called error signal, can be fed into a proportional-integral-derivative controller (PID) which creates a feedback loop with the laser. This setup allows us to suppress frequency fluctuations.

We discuss in more detail, how the error signal has to look like, for this mechanism to work. The photons of a laser beam passing through a vapour cell are partially absorbed by the gas atoms, as discussed in section 2.3.2. The photodiode in Figure 2.10 receives a Doppler-broadened absorption spectrum, like the one shown in Figure 2.7a

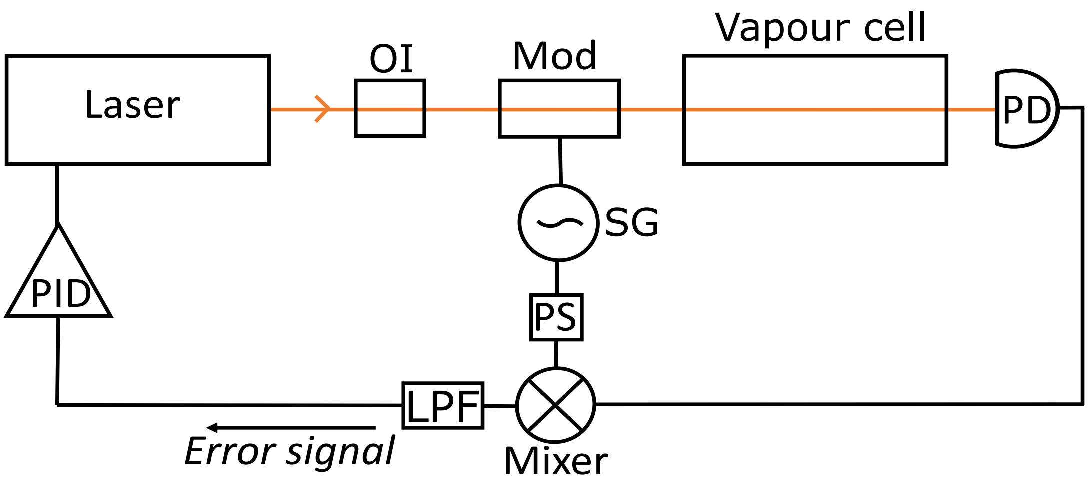

Figure 2.10.: Experimental setup for frequency-stabilisation using Doppler-broadened frequency modulation spectroscopy. OI: optical isolator, Mod: modulator, PD: photodiode, SG: signal generator, PS: phase shifter, LPF: low-pass filter, PID: proportional-integral-derivative controller.

for Rubidium. We want to stabilise the laser onto a frequency that corresponds to a transition frequency of the atomic gas and, therefore, hold the laser on the value of a local minimum of the absorption signal. This can not be realised experimentally, because deviations from the extreme value in the absorption spectrum result in an increase in both directions which makes it impossible to correct them. Mathematically, this problem can be solved by considering the derivative of the absorption spectrum with respect to the frequency. As the derivative will show a zero-crossing at the location of the transition frequency, which lies at the exact minimum of the showing dip in the absorption spectrum, the sign of the function will unambiguously determine the direction of any deviation.

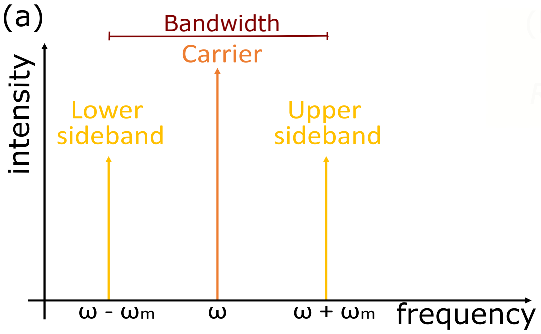

Figure 2.11.: Illustration of sidebands appearing next to the carrier frequency ω.

Experimentally, a function proportional to the derivative of the absorption spectrum can be realised as illustrated in Figure 2.10. We modulate the frequency of the signal emitted by the laser, for example, by modulating the laser output current or by using an electro-optic modulator. Then we feed that signal into a mixer, where it is multiplied with another oscillating signal which carrys the same frequency as the modulation signal. The modified signal is then passed through a low-pass filter to create the error signal. The modulation generates sidebands which are bands of frequencies higher or lower than the carrier frequency (see Figure 2.12a). In our case the carrier frequency is the atomic transition frequency ω in the absorption spectrum and the frequency of the sidebands Ω is determined by $\Omega = \omega \pm \omega_m$. They define the bandwidth of the modulated signal and can therefore be used for the generation of a stable error signal.

2.4.2. Quantitative approach

The aim of this section is, to obtain a function that relates the absorption signal recorded by the photodiode with its derivative. For this we will make use of the absorption coefficient α, as discussed in section 2.3.

A frequency ω, modulated with the constant frequency ω_m, can be expressed as $\omega' = \omega + \Delta\omega \cdot cos(\omega_m t)$ with $d\omega/\mathrm{dt} = 0$ and $\Delta\omega = \mathrm{const.}$ indicates the frequency deviation of the carrier. The real part of the corresponding electric field is

$$\begin{aligned} E(t) &= E_0 \cos(\Phi) \\ &= E_0 \cos[\omega t + M \sin(\omega_m t) + \varphi] \end{aligned} \tag{2.10}$$

considering $\partial\Phi/\partial t = \omega'$, E_0 is a constant and $M = \Delta\omega/\omega_m$ is the modulation index which, therefore, indicates the ratio between the frequency deviation of the carrier and the modulation frequency. We consider the field for $\varphi = 0$ (without loss of generality), resulting in

$$E(t) = \frac{E_0}{2} \exp\{i[\omega t + M \sin(\omega_m t)]\} + \frac{E_0}{2} \exp\{-i[\omega t + M \sin(\omega_m t)]\}. \tag{2.11}$$

Because M $\ll$ 1 for narrow bandwidths, this can be rewritten in terms of Bessel functions $J_n(M)$ of n-th order:

$$E(t) = \frac{E_0}{2} \sum_{n=-\infty}^{\infty} J_n(M) \exp\{i[(\omega + n\omega_m)t]\} + \frac{E_0}{2} \sum_{n=-\infty}^{\infty} J_n(M) \exp\{-i[(\omega + n\omega_m)t]\}, \tag{2.12}$$

which can be approximated to

$$\begin{aligned} E(t) = &\frac{E_0}{2}\exp(i\omega t) + \frac{M}{2} \exp[i(\omega t + \omega_m t)] - \frac{M}{2} \exp[i(\omega t - \omega_m t)] \\ &+ \frac{E_0}{2}\exp(-i\omega t) + \frac{M}{2} \exp[-i(\omega t + \omega_m t)] - \frac{M}{2} \exp[-i(\omega t - \omega_m t)], \end{aligned} \tag{2.13}$$

using $J_n(M) \approx \frac{M^n}{2^n n!}$ for M $\ll$ 1, so the Bessel functions can be neglected for n $>$ 1. Now the signal passes through the vapour cell of length L. The transmission can be defined as $T_n = exp(-\delta_n - i\phi_n)$ where $\delta_n = \alpha_n \frac{L}{2}$ represents the decrease of the field amplitude and ϕ the optical phase shift at $\omega + n\omega_m$. With this, the electric field behind the vapour cell can be described as

$$\begin{aligned}E_C(t) &= \frac{E_0}{2}\{T_0 \exp(i\omega t) + T_1\frac{M}{2}\exp[i(\omega t + \omega_m t)] - T_{-1}\frac{M}{2}\exp[i(\omega t - \omega_m t)]\} \\ &+ \frac{E_0}{2}T_0 \exp(-i\omega t) + T_1\frac{M}{2}\exp[-i(\omega t + \omega_m t)] - T_{-1}\frac{M}{2}\exp[-i(\omega t - \omega_m t)] \\ &= E_0\{\exp(-\delta_0)\cos(\omega t - \phi_0) + \frac{M}{2}\exp(\delta_1)\cos[(\omega + \omega_m)t - \phi_1] \\ &- \frac{M}{2}\exp(-\delta_{-1})\cos[(\omega - \omega_m)t - \phi_{-1}]\}.\end{aligned} \tag{2.14}$$

The intensity I_{PD}, measured by the photo-detector, is proportional to E_C^2 and can, therefore, be calculated to

$$I_{PD} = c\epsilon E_0^2 \exp(-2\delta_0)[1+M\ \cos(\omega_m t)(\delta_{-1}-\delta_1)+M\ \sin(\omega_m t)(\phi_1+\phi_{-1}-2\phi_0)], \tag{2.15}$$

where c denotes the speed of light and ϵ the permittivity. The detailed derivation of this formula can be found in the appendix, in section A.3. The amplitude of the oscillating parts, containing the desired information, can be extracted by feeding the signal into a mixer. The mixer receives an additional signal of the same frequency ω_m as the modulation. To ensure this, we use the same function generator as for the modulator. The phase can be adjusted by adding a phase shifter into the setup (see Figure 2.10). The mixer multiplies the two signals, which results in:

$$\begin{aligned}V(t) &= I_{PD} \cdot \cos(\omega_m t) \\ &= c\epsilon E_0^2 \exp(-2\delta_0)\{\cos(\omega_m t) + \frac{M}{2}[1 + \cos(2\omega_m t)](\delta_{-1} - \delta_1) \\ &+ \frac{M}{2}[\cos(\pi/2) + \cos(2\omega_m t - \pi/2)](\phi_1 + \phi_{-1} - 2\phi_0]\}.\end{aligned} \tag{2.16}$$

The calculation including all intermediate steps, can be found in section A.3. Feeding this signal into a low-pass filter, and thereby cancelling out low frequency terms ($\omega < \omega_m$), and approximating $\frac{\delta_1 - \delta_{-1}}{2\omega_m} \approx \frac{d\delta}{d\omega} = \frac{L}{2}\frac{d\alpha}{d\omega}$ due to choosing low modulation frequencies, we obtain the error signal:

$$V_{err} = -c\epsilon E_0^2 \frac{M}{2} \exp(-2\delta_0) L\omega_m \frac{d\alpha}{d\omega}. \tag{2.17}$$

This signal contains the derivative of α in terms of the frequency. Therefore, it shows a zero-crossing at the frequency ω_0.

As we will be using SAS in section 3, this is exemplarily shown in Figure 2.11 for a Lorentzian distribution for the field amplitude of the form

$$\delta_n(\omega) = \frac{A}{1 + (\frac{\omega + n\omega_m}{\Gamma/2})^2}, \tag{2.18}$$

where A is a constant and Γ the natural linewidth of the investigated gas.

We can conclude: the power in the transmitted beam passing through the vapour cell is recorded by a photo-detector which forwards the signal to a mixer. The mixer also obtains a second oscillating signal from the function generator. Multiplying these signals creates a demodulated signal by producing direct current terms which can be extracted through a low-pass filter. What is left of the modified signal is the error signal which can now be fed to a PID controller.

The PID controller uses functions of proportionality, integration and derivation to control a feedback signal, as illustrated in Figure 2.12b. The device receives an error signal and subtracts it from a given reference signal, here, a constant zero-value, in order to get a signal driving the P-, I-, and D-elements. The individual contributions are summed up and fed back to the process, in our case to the laser. The transfer function in its ideal form is

$$u(t) = K_P \cdot y(t) + K_I \int_0^{\infty} e(\tau) d\tau + K_D \frac{d}{dt} y(t), \tag{2.19}$$

where K_j denote the corresponding gains, $y(t)$ the process variable and $e(t)$ the difference function between the reference signal $r(t)$ and the process variable $(e(t) = r(t) - y(t))$ [25, 26].

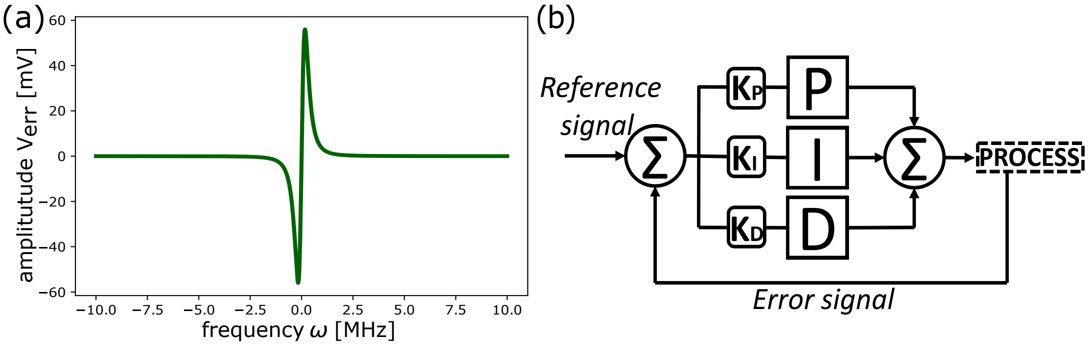

Figure 2.12.: (a) Example of the error signal using the function of the field amplitude shown in Eq. 2.18. We set the parameters to $c\epsilon E_0^2$=1, L = 0.1 m, M = 0.1, ω_m = 10 MHz, A = 0.1 and Γ = 6 MHz. (b) Basic working principle of a PID controller. The obtained error signal is compared to a reference signal through proportionality (P), integration (I) and derivation (D) tuned by the corresponding gains K$_j$ and integrated into a feedback-loop with the process.

2.5. Modulated saturated absorption spectroscopy

As the aim of this thesis is miniaturising a frequency stabilised laser, which is achieved by using absorption spectroscopy, we need to determine which kind of spectroscopy is suited best for this application. It was already discussed that SAS is necessary in order to get a frequency precision high enough to stabilise the laser on. In order to conduct frequency stabilisation, some kind of oscillating modulation needs to be added to the frequency of the laser signal which is meant to be analysed. For this modulation an electro-optic modulator will be used. In section 3 we will compare frequency modulation spectroscopy in an ordinary and a retroreflective version to modulation transfer spectroscopy in order to find out which method should be implemented into the miniaturised design. These three different methods will be introduced now. The advantages and disadvantages of the different spectroscopy methods will be discussed after performing the respective experiments.

2.5.1. Frequency modulation spectroscopy (FMS)

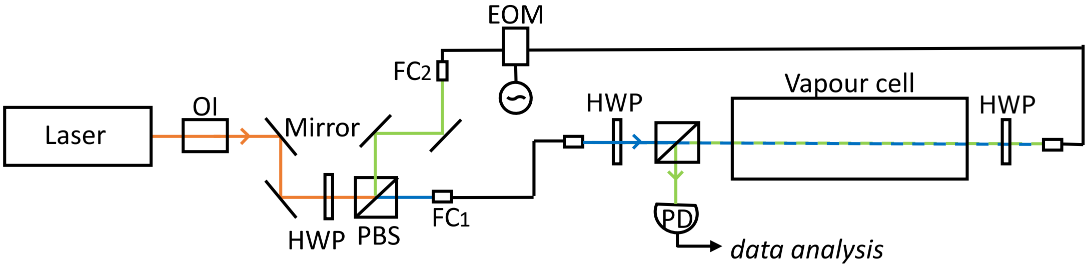

Figure 2.13.: Experimental setup for frequency modulation spectroscopy. OI: optical isolator, HWP: $\lambda/2$-wave-plate, PBS: polarising beam splitter, FC: fibre coupler, EOM: electro optical modulator, PD: photodiode, pump beam, probe beam.

Figure 2.13 shows the scheme of a frequency modulation spectroscopy setup. As FMS is a kind of SAS, the setup is almost identical with the one discussed in section 2.3.2 in Figure 2.9, just that now, an eletro-optic modulator (EOM) is added in the path of the probe beam for the modulation of the signal as discussed in section 2.4. The basic working principle of an EOM is the following: it is a device that can modify the optical features of light, such as the phase or polarisation, using an electronic control signal which is implemented by a function generator. It consists of a birefringent crystal and uses the electro-optic effect, which is the phenomenon of the refraction index of a material being modified due to an applied external electrical field [27, 28]. Here, the EOM is used to modulate the frequency of the probe beam. This is possible when modulating its phase, because phase modulation and frequency modulation are both proportional to the modulating voltage, therefore a change in phase results in a change of frequency and vice versa. The modulation of the probe beam is performed in order to generate sidebands, as described in section 2.4. In the experiments, a fibre EOM with a Lithium Niobate X-Cut Y-Prop, MgO doped crystal is used [29]. By connecting the EOM to a function generator which is producing a sinusoidal signal, the EOM is used as a voltage-controlled waveplate for the probe beam, by which the phase, and therefore the frequency, can be regulated [30]. The modulated probe beam then coincides with the pump beam inside the vapour cell and is measured by a photodiode. This signal can then be used for laser stabilisation as discussed in section 2.4 [23].

2.5.2. Retroreflective saturated absorption spectroscopy (RRS)

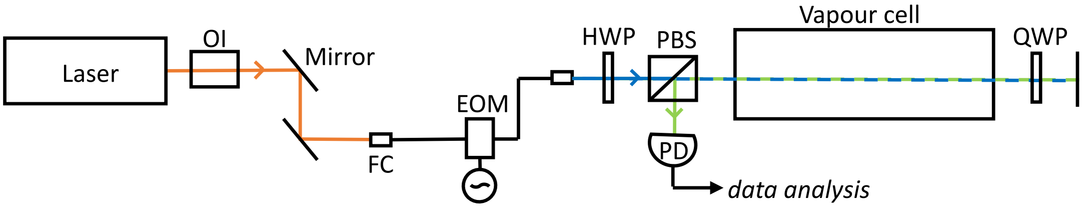

Figure 2.14.: Experimental setup for retroreflective saturated absorption spectroscopy. OI: optical isolator, HWP: $\lambda/2$-wave-plate, PBS: polarising beam splitter, FC: fibre coupler, EOM: electro optical modulator, QWP: $\lambda/4$-wave-plate PD: photodiode, pump beam, probe beam.

As shown in Figure 2.14, in RRS, the emitted light from the laser is directed onto a mirror system consisting of two mirrors, which allow us to perform a beam walk, and is then directly coupled into a fibre. The light is modulated by an EOM and the modulated wave passes through a $\lambda/2$-wave plate and a PBS. It goes through the vapour cell and a $\lambda/4$-wave plate and hits a mirror which sends it back onto the PBS where the laser beam is reflected onto a photodiode which again records the spectrum of the gas inside the vapour cell. Here it is important to remember, even though here RRS is treated seperately, that retroreflective saturated absorption spectroscopy is just a modified version of FMS, i.e. as the same beam passes through the cell twice, the light emitted from the laser acts as the probe beam as well as the pump beam. The intensity ratio is not tunable in this case and will always be 50/50 [23].

2.5.3. Modulation transfer spectroscopy (MTS)

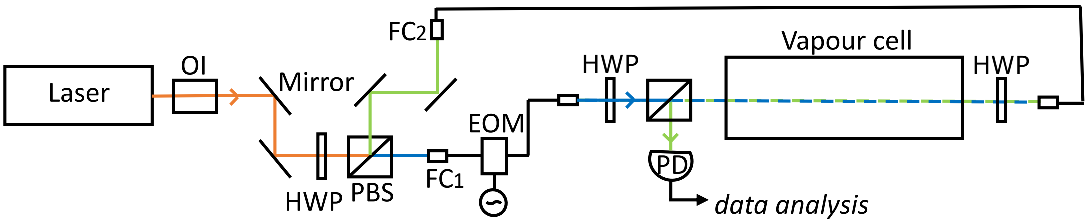

Figure 2.15.: Experimental setup for modulation transfer spectroscopy. OI: optical isolator, HWP: $\lambda/2$-wave-plate, PBS: polarising beam splitter, FC: fibre coupler, EOM: electro optical modulator, PD: photodiode, pump beam, probe beam.

In Figure 2.15 the experimental setup for modulation transfer spectroscopy is shown. As in FMS, the light emitted by the laser is split into two beams. While in FMS the probe beam is modulated by the EOM, in MTS the pump beam is the one being modulated. Because the measured beam is not modulated here, the error signal will differ from the one described in section 2.4. The generation of the MTS error signal is based on non-linear interactions between pump and probe beam and the derivation of it would beyond the frame of this work. For further information see Refs. [31] and [32].

3. Comparison of different spectroscopy methods for the laser frequency stabilisation

After discussing the possible approaches to realise Doppler-free spectroscopy, measurements with the three different methods are taken in the laboratory and the resulting error signals are compared. This will allow us to optimise the features of the miniaturised version of the frequency-stabilised setup, i.e. which spectroscopy method delivers the desired results, needs little input power and keeps the dimensions to a minimum.

3.1. Experimental setup

Figure 3.2 shows the experimental setup for a laser frequency stabilisation onto an atomic reference frequency. The names of the models and the manufacturers of each component used in this setup are listed in Table A.3.

The light is emitted from an external cavity diode laser (ECDL) at a wavelength of 767 - 780 nm, as this includes the wavelength range of the Rubidium transitions which lie around 780 nm. The basic working principle of such a diode laser is described in section 2.1.1.

The vapour cell, through which the probe and the pump beam pass, contains Rubidium gas in natural abundance with 72.2% ^{85} Rb and 27.8% ^{87}Rb (see section 2.2.4).

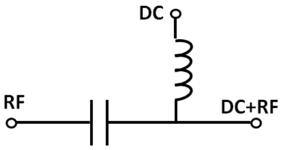

Figure 3.1.: Electrical schematic of a bias tee.

Until the probe beam hits the photodiode, the procedure is the same as in the sections 2.5.1 for FMS (Figure 3.2a), 2.5.3 for MTS (Figure 3.2b) and 2.5.2 for RRS (Figure 3.2c). From the photodiode the signal is first fed into a bias tee. A bias tee is an electronic device which splits the incoming signal into its alternating current (AC) part and its direct current (DC) part. This can be understood by looking at its electrical schematic, shown in Figure 3.1. A capacitor builds up a strong electric field when put into a direct current circuit but works as a resistor with frequency-dependant impedance in an alternating current circuit. This will allow the signal in the radiofrequency (RF) range to pass but block the DC. In this sense, it acts like a high-pass filter. An inductor, on the other hand, needs a certain amount of time to build up a magnetic field and to let current flow through which is why it blocks high frequencies and transmits direct current and therefore acts like a low-pass filter [33]. Since we are only interested in the MHz part of the signal,

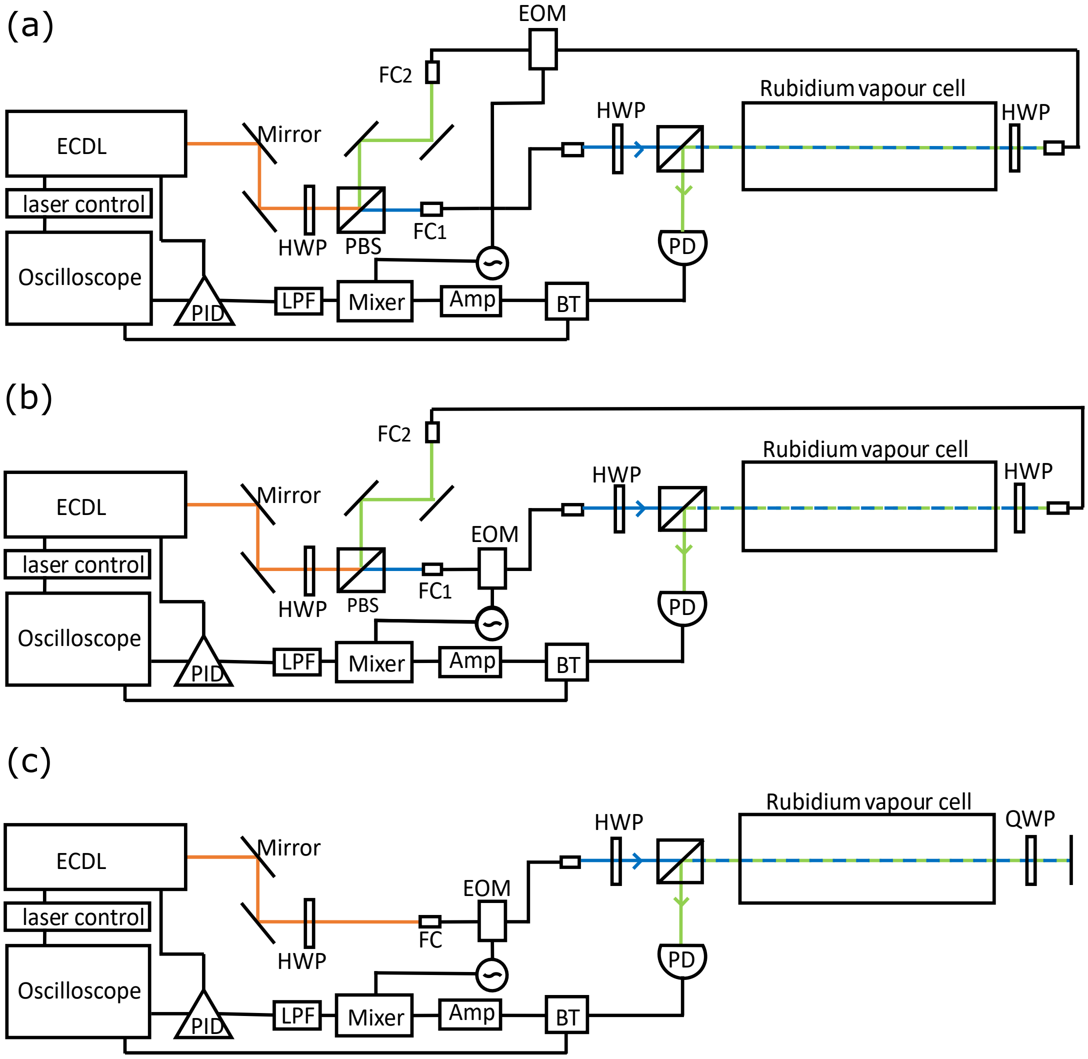

Figure 3.2.: Schematic of the experimental setups for (a) frequency modulation spectroscopy, (b) modulation transfer spectroscopy, and (c) retroreflective saturated absorption spectroscopy. The laser is emitted from an ECDL, passes through the corresponding spectroscopy setup and the signal is recorded using a photodiode (see section 2.5). The signal is now modified by passing through a bias-tee, an amplifier, a mixer and a low-pass filter before entering the PID controller. The stabilising signal is fed back to the laser. ECDL: external cavity diode laser, HWP: $\lambda/2$-wave plate, PBS: polarising beam splitter, FC: fibre coupler, EOM: electro-optic modulator, QWP: $\lambda/4$-wave plate, PD: photodiode, BT: bias tee, Amp: amplifier, LPF: low-pass filter, PID: proportional-integral-derivative controller, pump beam, probe beam.

i.e. in the range of the modulation frequency of the EOM, we take the signal from the RF-output and send it through an amplifier before it is fed into the mixer. After this we perform the frequency stabilisation as described in section 2.4.

Photos of the experimental setup can be found in section A.4.1 (Figures A.2, A.3 and A.4).

The aim of the following section is to optimise the error signal regarding its amplitude, slope and required input power by varying different parameters. The aim is to lock onto a narrow frequency range and choose the method that is best-suited for the implementation into the miniaturised design. For that, we compare the three different spectroscopy setups mentioned above. We will also consider the spacial requirements of each discussed setup.

3.2. Optimisation of the error signals and choice of method

In order to determine the spectroscopy method that is suited best for the miniaturised frequency-stabilised laser setup, an error signal is created and maximised for each introduced method. For this, different parameters are taken into account, such as the amplitude, the needed input power and the gradient of the corresponding slope of the ^{87}Rb F=2→F=3 transition of the error signal. This transition was chosen because the error signal in all methods showed a sufficient slope at the corresponding frequency. The amplitude ΔV, defined as the distance between the maximum and the minimum value of the slope inside a transition of the error signal, is maximised by varying different input parameters. The locking mechanism detects deviations from zero, as discussed in section 2.4. The higher the amplitude of the slope, the easier it is for the locking mechanism to find the correct value to stabilise on. The same argument hold for the gradient of the slope: the faster the signal changes from zero, the better the mechanism is able to sensor the deviation. We evaluate the gradient of the slope by fitting a linear function to it and discuss its sufficiency. The reason for the minimisation of the necessary input power lies in the final application of the system. We want to use the frequency-stabilised diode laser for further experiments. Therefore, we want most of the total laser power to be available for those experiments. As a result, it is necessary to minimise the power going into the stabilisation. As the experimental setup will eventually be miniaturised, we also consider the complexity and spacial requirements of each setup.

3.2.1. Frequency modulation spectroscopy

For FMS, we use the setup shown in Figure 3.2a.
The laser beam emerging from the ECDL measures around 3 mm × 1 mm, [7], and is set to the temperature T = 22.2 °C and the current of I = 144 ± 5 mA. The EOM is run at frequency ω = 10 MHz and an amplitude of 2.5 V$_{pp}$, the mixer receives a signal of ω = 10 MHz and an amplitude of 450 mV$_{pp}$. The phase difference between the signals of the EOM and the mixer is $\Delta\phi$ = -110°. To the amplifier, a voltage of 15 V is applied.

The corresponding errors for each value are stated in Table A.4 and are omitted here, for better readability.

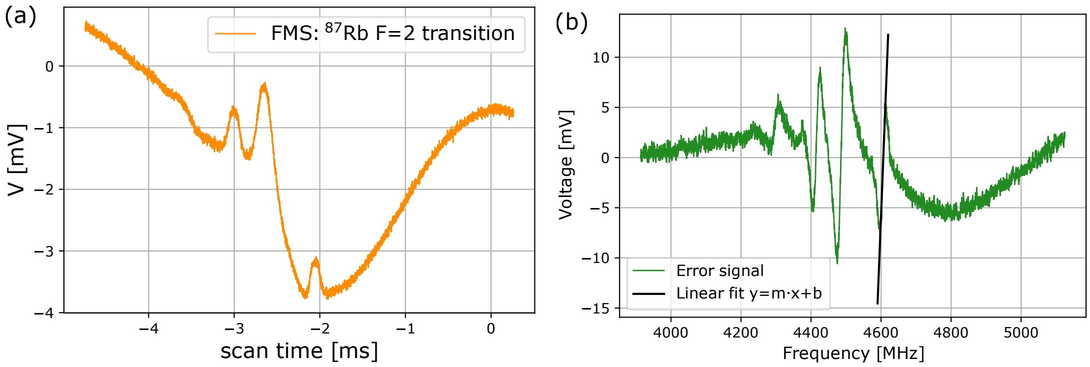

Figure 3.3.: (a) Absorption spectrum obtained using frequency modulation spectroscopy at the Rubidium D2 line of the ^{87}Rb F=2 level. (b) Corresponding error signal with a linear function fit to the F=2→F'=3 transition.

We observe an absorption spectrum and the corresponding error signal, as shown in Figure 3.3. The error signal appears as derived in section 2.4, showing a zero-crossing for each hyperfine transition and the cross-over resonances, as described in section 2.3.2, which are visible in the absorption spectrum. This will be further discussed in section 3.2.4.

First we try to maximise the amplitude ΔV of the slope at the ^{87}Rb F=2→F=3 transition:

In Figure 3.4, the results for the different measurements are shown. Before varying different parameters, we maximise the amplitude of the error signal by eye. This is accomplished by adjusting the output power of the laser at the fibre coupler and, therefore, modifying the power transmitted into each of the spectroscopy beams. When exiting the corresponding fibre, we ensure the maximum overlapping of probe and pump beam inside the Rubidium cell by slightly adjusting the fibre ports which emit the beams into the spectroscopy setup, until the amplitude of the error signal seems to be maximised.

First we want to see how the amplitude of the error signal changes when varying the pump beam intensity relative to the probe beam intensity and vice versa. For this, we take measurements around the values where the error signal is visibly large. As shown in Figure 3.4a, when keeping the power of the probe beam at a constant value of 0.1 mW, we observe an increase of the error signal amplitude for an increase of the pump beam power. It reaches a maximum amplitude of 11.6 mV at $P_{pump} = 0.3$ mW before slowly decreasing again.

The same observation is made when keeping the power of the pump beam at a constant value ($P_{pump} = 0.3$ mW), as shown in Figure 3.4b. The values of P_{probe} first

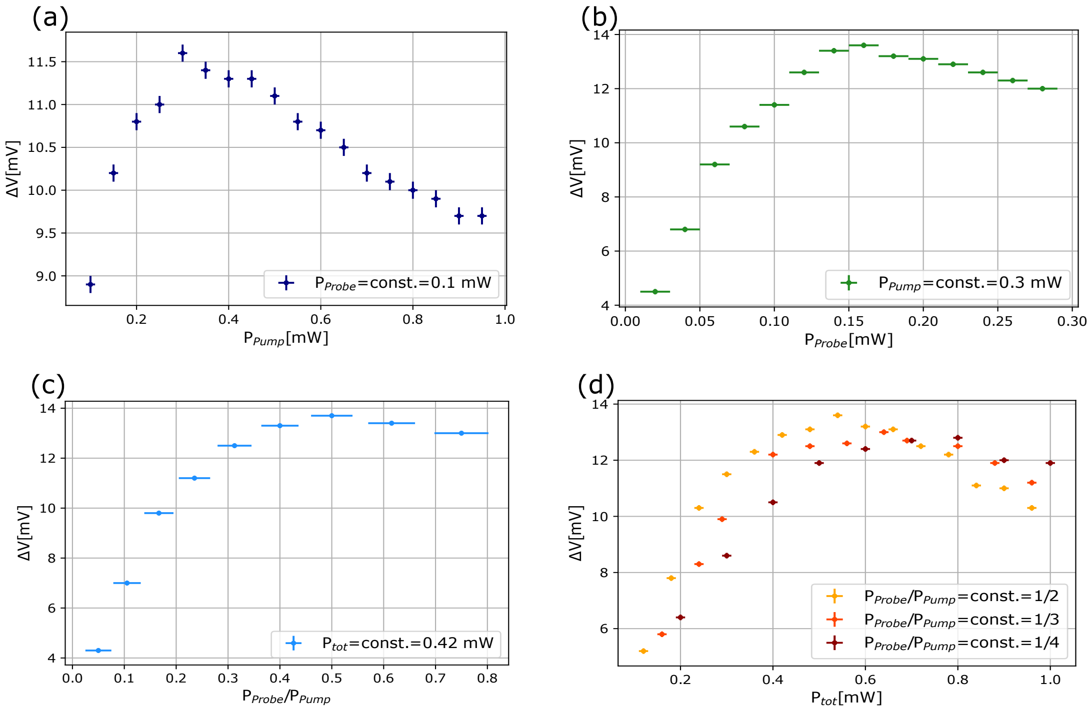

Figure 3.4.: Graphs obtained from frequency modulation spectroscopy for different values held constant: (a) P_{probe} = const. for varying P_{pump}, (b) P_{pump} = const. for varying P_{probe}, (c) P_{tot} = const. for varying P_{probe}/P_{pump}, (d) P_{probe}/P_{pump} = const. for varying $P_{tot} = P_{probe} + P_{pump}$. The values for the error bars are stated in Table A.4.

increase, reach a maximum of $\Delta V = 13.5$ mV at $P_{probe} = 0.16$ mW and decrease after that.

There seems to be a correlation between P_{pump} and P_{probe}. To find out how they are related to each other and to get a maximised error signal, we define the total power given to the spectroscopy as $P_{tot} = P_{probe} + P_{pump}$. We will look how the amplitude can be maximised while keeping the total power at a constant value ($P_{tot} = 0.42$ mW). This results in a graph as shown in Figure 3.4c, where a maximum of $\Delta V = 13.6$ mV is reached at a ratio $P_{probe}/P_{pump} = 1/2$. Ultimately, we want to verify that this ratio is also showing the biggest possible error signal amplitude even when changing the total optical power given to the spectroscopy. Three different ratios ($P_{probe}/P_{pump} = 1/2$, 1/3, and 1/4) were measured at different total optical power values (see Figure 3.4d). All curves show a peak between 12 mV and 14 mV, for the $P_{probe}/P_{pump} = 1/2$ ratio, the error signal amplitude seems to be slightly higher than for the other values. The more valuable result here is the fact, that the $P_{probe}/P_{pump} = 1/2$ ratio needs less total optical power to reach its maximum value.

This directly brings us to the second point we would like to optimise for the maximised error signal: the minimisation of the total power needed from the laser.

We are trying to frequency-stabilise a diode laser, which can then be used for further experiments. We want most of the total laser power to be used for those experiments. As a result, it is necessary to minimise the power going into the frequency stabilisation. In Figure 3.4d we obtain the maximum amplitude at the total power of P_{tot} = 0.55 mW which will be evaluated in section 3.2.4.

The last feature to be considered is the gradient of the slope of the corresponding transition in the error signal. The gradient is obtained by plotting a linear fit into the error signal at the transition the laser is meant to be locked on, as illustrated in Figure 3.3. The linear fit here gives us a gradient of m = 0.90 V/GHz at maximised amplitude. This value will later be compared to the gradients obtained by the other spectroscopy methods.

We will perform the same analysis of the error signals for the MTS and RRS setups before discussing results, correlations and possible consequences.

3.2.2. Modulation transfer spectroscopy

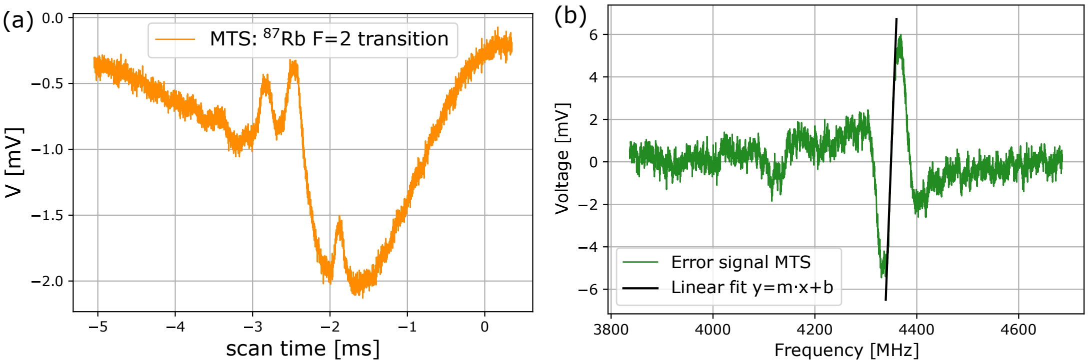

Figure 3.5.: (a) Absorption spectrum obtained using modulation transfer spectroscopy at the Rubidium D2 line of the ^{87}Rb F=2 level. (b) Corresponding error signal with a linear function fit to the F=2→F'=3 transition.

For the MTS measurements, we use the experimental setup in Figure 3.2b.

We are able to observe an absorption spectrum and an error signal, as shown in Figure 3.5. The phase difference between the signals of the EOM and the mixer is changed to $\Delta\phi = +110°$.

Taking the same measurements as for the FMS, we obtain the graphs as shown in Figure 3.6. We first look at the power of the pump beam while keeping P_{probe} constant at 0.14 mW and see that a peak of around 11 mV occurs but at higher powers than before (see Figure 3.6a). Also, we notice that the curve is quite flat, showing a maximum value in the range of P_{pump} = 0.80-1.75 mW.

As shown in Figure 3.6b, also when keeping the power of the pump beam at a constant value of P_{pump} = 1.7 mW, maximum values of 11-12 mV appear in a range of P_{probe} = 0.17-0.50 mW. In both graphs we recognise that P_{pump} needs to be of

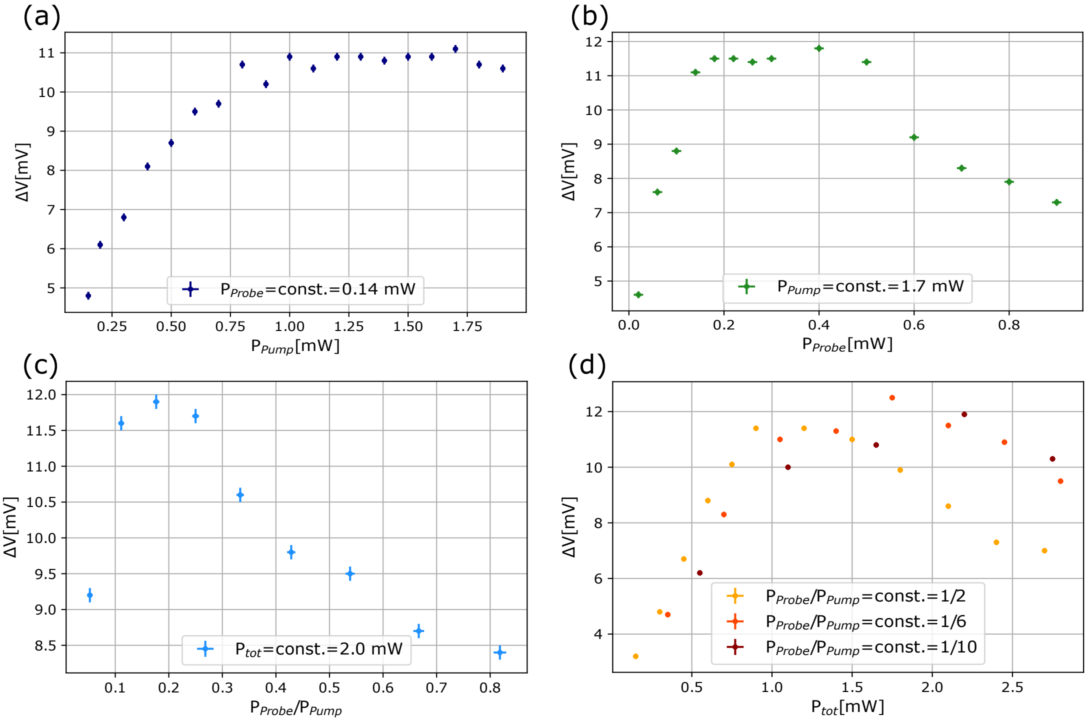

Figure 3.6.: Graphs obtained from modulation transfer spectroscopy with different values held constant: (a) P_{probe} = const. for varying P_{pump}, (b) P_{pump} = const. for varying P_{probe}, (c) $P_{tot} = P_{probe} + P_{pump}$ = const. for varying P_{probe}/P_{pump} and (d) P_{probe}/P_{pump} = const. for three different values for varying P_{tot}. The values for the error bars are stated in Table A.4.

much higher value than P_{probe}. This is why, in the next step the total power is again kept at a constant value (P_{tot} = 2.0 mW) while the ratio P_{probe}/P_{pump} is modified, as shown in Figure 3.6c. This results in a steep maximum around the ratio of 0.18 (so between P_{probe}/P_{pump} = 1/6 and 1/5).

Figure 3.6d shows the curves for different ratios (P_{probe}/P_{pump} = 1/2, 1/6 and 1/10) at varying P_{tot}. It confirms that the maximum amplitude of 12.5 mV can be reached using a ratio of P_{probe}/P_{pump} = 1/6 at P_{tot} = 1.75 mV. We choose the maximum value of ΔV = 11.9 mV at a total power of P_{tot} = 1.0 mW for our signal in order to have a high amplitude without having to use too much total power.

Having maximised the amplitude of the error signal, we obtain a gradient of m = 0.63 V/GHz, taken from the linear fit in Figure 3.5.

In the error signal for MTS we notice that, compared to the error signal for FMS, only one slope is visible in the whole ^{87}Rb F=2 transition. This is due to the lineshape baseline stability becoming almost independant of linear absorption effects, as modulation appears in the unmodulated probe beam caused by sufficient non-linear interactions of the pump and the probe beam with the Rubidium vapour [31]. The detailed discussion about this phenomenon would go beyond the frame of this work.

See Refs. [31] and [32] for additional information.

3.2.3. Retroreflective saturated absorption spectroscopy

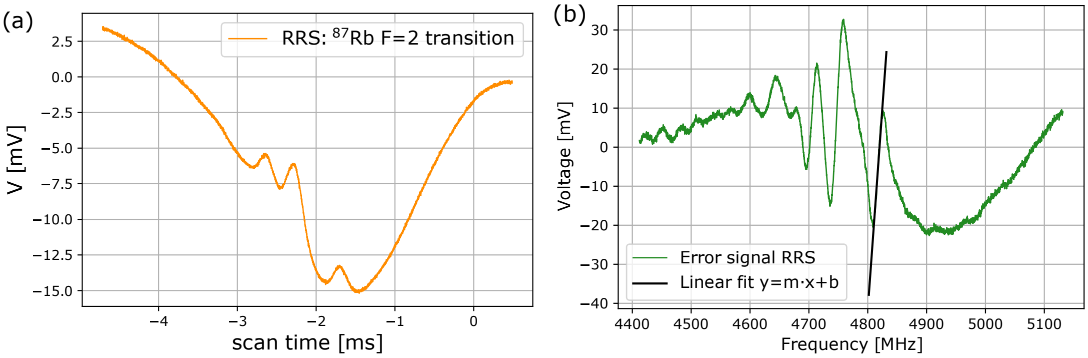

Figure 3.7.: (a) Absorption spectrum obtained using retroreflective saturated absorption spectroscopy at the Rubidium D2 line of the ^{87}Rb F=2 level. (b) Corresponding error signal with a linear function fit to the F=2→F'=3 transition.

The RRS setup is shown in Figure 3.2c.
The phase difference between the signal of the EOM and the mixer is set to $\Delta\phi$ = -180°.

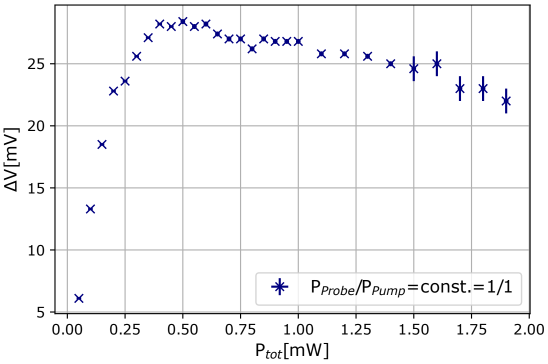

Figure 3.8.: Graph obtained from retroreflective saturated absorption spectroscopy with P_{probe}/P_{pump} = 1 for varying P_{tot} = P_{probe} + P_{pump}. The values for the error bars are stated in Table A.4.

We are again able to observe an absorption spectrum and the corresponding error signal which appears as derived in section 2.4. They are shown in Figure 3.7.
Since the RRS setup is a kind of FMS where we are not able to vary probe and pump beam power individually, less measurements can be taken. In Figure 3.8a the variation of P_{tot} at the constant probe to pump beam ratio P_{probe}/P_{pump} = 1 is shown. It displays a maximum amplitude of ΔV = 28 mV at P_{tot} = 0.5 mV. Using this value for the maximised error signal, a gradient of m = 2.08 V/GHz is obtained at the ^{87}Rb F=2→F=3 transition, as shown in Figure 3.7b.

3.2.4. Discussion and interpretation of the results

	ΔV_{max} [mV]	$P_{tot_{max}}$ [mW]	m [V/GHz]	S/N
FMS	13.5 ± 0.1	0.5 ± 0.01	$0.90 \pm 4.49 \cdot 10^{-4}$	7.5 ± 0.4
MTS	12.0 ± 0.1	1.0 ± 0.01	$0.63 \pm 2.46 \cdot 10^{-4}$	4.8 ± 0.2
RRS	28.0 ± 0.2	0.4 ± 0.01	$2.08 \pm 1.04 \cdot 10^{-3}$	10.0 ± 0.4

Table 3.1.: Overview of the values for optimised error signals for frequency modulation, modulation transfer, and retroreflective saturation absorption spectroscopy. S/N denotes the signal-to-noise ratio.

In this section, first, the observations regarding the error signals, obtained by the different methods, are discussed. Then the spectroscopy setup is going to be chosen for the miniaturised design in order to obtain a frequency stabilisation module with high efficiency and miniaturised dimensions. To give an overview, the best values chosen for the error signal of each spectroscopy method are given in Table 3.1.

Contrary to expectation, for the FMS and the RRS approaches, we obtain absorption signals for Rubidium showing four peaks inside the Doppler profiles. We would expect three peaks from the hyperfine transitions and three additional cross-over resonances, as discussed in section 2.3.2.2. Based on their position we are able to tell which transitions we observe. They correspond to the ^{87}Rb F=2→F=3 transition, the cross-over resonances of the ^{87}Rb F=2→F=1 to the ^{87}Rb F=2→F=2, 3 transitions respectively, and the cross-over resonance of the ^{87}Rb F=2→F=2 to the ^{87}Rb F=2→F=3 transition. The same argumentation holds for the corresponding error signals. Why the remaining transitions do not show in the spectra could be due to insufficient adjustment of the beams inside the vapour cell. As the energy needed for the excitation of the remaining transitions is considerably higher (compare Figure 2.5) they are less likely to take place, and are therefore not visible within the achieved resolution.

When looking at the three error signals and corresponding values in Table 3.1, we immediately notice that the maximum amplitude in the RRS setup shows a value twice as high as for the FMS and the MTS approaches. This is also a result contrary to expectations, as RRS is a modified FMS procedure, wherefore we expect the same order of magnitude in the signals. The unexpected increase in amplitude could be explained by insufficient adjustment of the experimental setup. It is possible that the probe and the pump beam exiting the fibres in the FMS and MTS setups are not perfectly aligned inside the vapour cell while the reflected beam in the RRS version overlaps inside the vapour cell more accurately. Better beam alignment results in more atoms within a velocity group, which the photons of both laser beams can excite. This leads to deeper lamp dips and, therefore, to an improved error signal. Unfortunately we did not take a measurement with the FMS setup for a ratio $P_{probe}/P_{pump} = 1$. Observing a value within the same order of magnitude as for the residual FMS measurements, could confirm this assumption.

Regarding the amount of zero-crossings and their relative intensities, all error signals appear as expected with respect to the derivation in section 2.4 or, for the MTS setup, with respect to Refs. [31] and [32]. As previously discussed, the observation that the amplitude of the error signal obtained by RRS is twice as high as the one obtained by FMS does not agree with our expectations. Unfortunately, we did not measure the modulation indices M in the experiments which is why a direct comparison of the amplitude values does not make sense, since higher modulation indices than the one chosen in Figure 2.11 result in higher amplitudes and steeper slopes.

We also notice that all graphs shown in Figures 3.4, 3.6, and 3.8a show a maximum in the amplitude of the error signal. One possible explanation for this observation is the saturation intensity of the Rubidium transition. It results from the limited amount of atoms which can be excited at the corresponding light frequency and is proportional to the natural decay rate of the excited atomic state and the on-resonance scattering cross section and depends on the polarisation the incoming light [15]. As we are not looking at the absorption spectrum directly but at the amplitude of the resulting error signal, additional factors will contribute to the reasons for the saturation value in the graphs.
The higher value of $\mathrm{P}_{tot_{max}}$ in the MTS approach is a result of the method itself [31]. The measured (probe) beam is not modulated itself, but it receives the modulation information from the pump beam when colliding inside the vapour cell. The effect also arises from the non-linear processes generating the sidebands in the probe beam, but again, MTS had to be studied in more detail in order to understand the exact impact.

In the FMS and the MTS approach, the obtained $\Delta\mathrm{V}_{max}$-values have the same order of magnitude. Also both show a sufficient amplitude and gradient of the corresponding slope for the laser-locking. Looking at the values of the error signal for the RRS, the amplitude and the gradient are even higher than for FMS and MTS methods, as previously discussed. Therefore, the values are also sufficient for the laser-locking and can be equally used for the stabilisation. All discussed methods show a satisfactory signal-to-noise ratio S/N.

As the main aim of this work is to miniaturise the laser stabilising setup, we are also going to take a look at the components needed to set up the different spectroscopy setups. As for FMS and MTS the light beam coming from the laser first needs to be split up into two beams, resulting in additional mirrors, a PBS, a $\lambda/2$-wave plate and a fibre coupler being needed for the setup. For the RRS we need less optical components, as we can see in Figure 2.14. Therefore, it reduces the size of the miniaturised setup. This is why we decided to implement the retroreflectice saturated absorption spectroscopy setup into the design of the miniaturised laser frequency stabilisation.

3.3. Verification of the laser locking

Before we implement the setup into the design software to create a miniaturised version of it, we first want to verify that the frequency stabilisation works in the laboratory. Later, the same procedure should work for the new design.

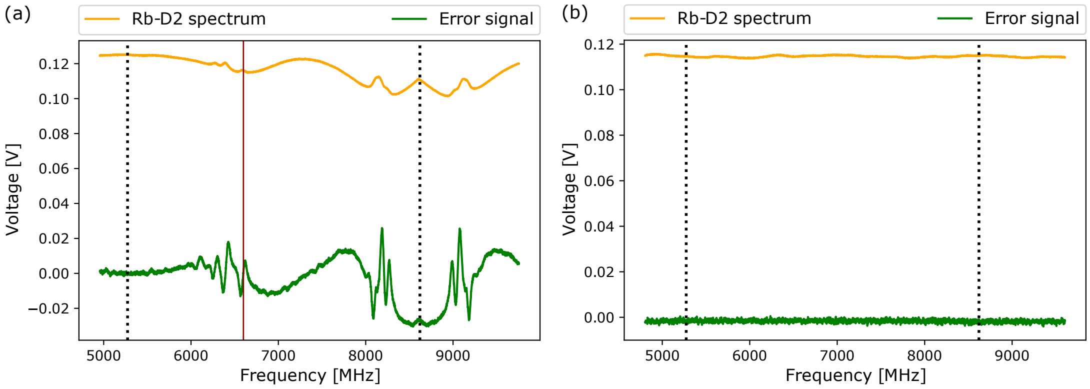

Figure 3.9.: Spectrum (orange line) and error signal (green line) of the Rubidium D2 line in the range of the ^{87}Rb F=2 and the ^{85}Rb F=3 transitions performing retroreflective saturated absorption spectroscopy. The dotted lines indicate the turning points of an additional triangle signal fed to the laser. (a) Signal before locking onto the frequency indicated by the red line, (b) Stabilised signal.

We want to show, once activating the lock in the RRS setup, that the characteristic spectrum of the Rubidium D2 line will vanish while still feeding an oscillating signal into the current input of the laser. The Rubidium spectrum and the corresponding error signal shown in Figure 3.9 are obtained by scanning the frequencies of the absorption spectrum around the ^{87}Rb F=2 and the ^{85}Rb F=3 transitions. This can be done by feeding a triangle function into the laser control using a function generator. The input signal has an amplitude of $A = 350$ mV$_{pp}$ and a frequency of $\omega = 300$ mHz. In Figure 3.9 it is indicated by the dotted lines which show the position of the turning points of that signal. We see that the spectra in Figure 3.9a are mirrored at those lines. The red line indicates the frequency we want to lock the laser onto. The locking mechanism is activated and therefore, as described in the functionality of a PID controller in section 2.4, the error signal is stabilised onto a constant zero-value by feeding the processed information back to the laser through the piezo input. The piezo input adjusts the tuning element inside the ECDL (see Figure 2.2). In the miniaturised version, where a DFB laser is integrated, the information is fed to the laser through the current input, where it adjusts the diffraction grating as described in section 2.1.3. We are able to optimise the output signal by adjusting the contribution of the corresponding proportional, integral and derivative control gains K$_P$, K$_I$ and K$_D$ (see Figure 2.12b). The oscilloscope now shows the signal presented in Figure 3.9b. Although we are still feeding the same oscillating signal to the laser through the current input, the spectrum as well as the error signal do not show noteworthy fluctuations anymore and are, therefore, stabilised on the value of the set frequency.

Now that we verified that the stabilisation of the laser works for the preferred spectroscopy method in a laboratory setup, we will design the miniaturised version of the frequency-stabilised laser using RRS.

4. Miniaturisation of the setup

In this section we discuss the design of the miniaturised frequency-stabilised diode laser. As a reminder: we want to design a setup of Doppler-free spectroscopy for the laser frequency stabilisation using retroreflective saturated absorption spectroscopy, which satisfies spacial requirements for good portability. It is meant to allow quick packing and easy transportation while ensuring high mechanical stability, simple readjustment and satisfactory laser frequency stabilisation. The dimensions result from the choice of components, which was based on keeping the production costs and efforts as small as possible. First, the chosen design is described. As the next step, the choices made around it will be explained in more detail and the used components, sizes and materials will be looked at.

4.1. Description of the chosen design

Figure 4.1 shows the design of the miniaturised frequency-stabilised diode laser. The implemented models are listed in Table A.5. The dimensions of every customised part can be found in the corresponding technical drawing in section A.4.4. The implemented screws, nuts and adaptors can be found in Table A.6.

The design consists of two modules, one containing the diode laser, coupling into fibres, here referred to as the “laser box”, and one containing the spectroscopy setup and the electronics. The second module will be referred to as the “spectroscopy box”. Putting the entire setup into one single module would bring certain advantages. For instance, we would have only one module to design, setup, store, and carry when needed. Nevertheless, we decided to design two modules. This design has one major advantage: despite the fact that we wanted to achieve a miniaturised frequency-stabilised laser setup, we are keeping it optional if the frequency stabilisation is needed for each individual experiment. When it is not needed, the second module can simply be omitted and the laser box serves as a portable fibre-coupled diode laser. Considering that the idea behind the design of a miniaturised laser was mainly to make operations at university easier, a portable laser which can be chosen to be frequency stabilised, serves this purpose better.

The idea behind the design is having a base plate with equally-spaced holes aligned in a grid structure, where the commercial components can be secured, by clamping them with the corresponding posts to the base plate. This ensures the desired flexibility in terms of usage, as the individual parts can be safely secured to the module or, alternatively, be taken out for a different purposes.

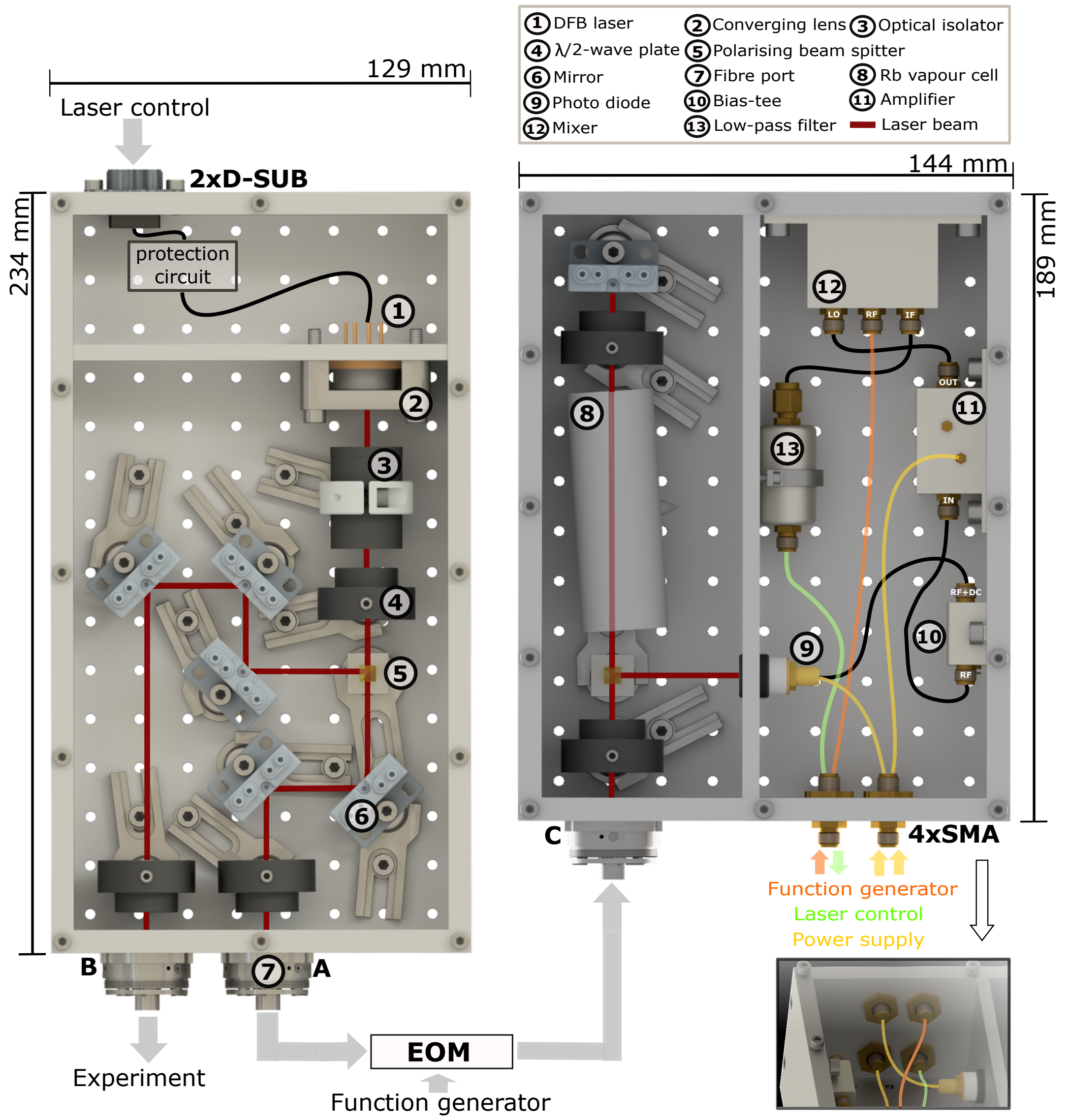

Figure 4.1.: Design of the miniaturised setup. (1) The laser beam (red line) coming from the DFB laser is (2) collimated by a converging lens, passes through (3) an optical isolator and (4) a $\lambda/2$-wave plate, and (5) hits a polarising beam splitter. The beam is split into two paths. Both hit (6) some mirrors and pass through another $\lambda/2$-wave plate before coupling into (7) fibre ports. Fibre port B can be connected to an experiment. Fibre port A is connected to fibre port C through an electro-optical modulator. The laser beam is polarised so that it transmits through the polarising beam splitter. It passes the (8) Rubidium vapour cell, a $\lambda/4$-wave plate and is reflected at a mirror. Back at the polarising beam splitter the beam is reflected onto the (9) photodiode. The recorded signal passes through (10) the bias-tee, (11) the amplifier, (12) the mixer and the (13) low-pass filter. The modified signal leaves the module via SMA connectors and is fed to the laser control which gives the information back to the laser through D-SUB connectors. All implemented components are listed in Table A.5.

The laser box consists of two chambers. The small chamber contains the wires needed in order to connect the DFB laser (1) to the D-Sub connectors. In order to protect the laser, the wires should be soldered to a TO-3 socket [34], and the D-Sub connectors, which receive the temperature and current regulations from the laser control, should pass through a protection circuit before entering the laser.

The laser beam emerging from the DFB laser is first collimated, by adding the converging lens (2). After passing through an optical isolator (3) the beam is split into two beams. By adding a $\lambda/2$-wave plate (4), the relative intensities of the beams can be set. The beam, transmitting through the PBS (5) and coupling into fibre port (7) A, is chosen to receive around 1% of the total power and is used for the frequency stabilisation of the laser. The mirrors (6) in the optical path ensure the precise coupling into the fibre ports. By including at least two mirrors in each path, we obtain two degrees of freedom to adjust the beam propagation onto the entrance of the optical fibre. The wave plate in front of the fibre port is added to align the polarisation of the laser beam with the optical axis of the fibre. For the frequency stabilisation, fibreport A can be connected to fibre port C of the spectroscopy box via a fibre-EOM. From here the laser beam passes through the RRS setup, containing the Rubidium vapour cell (8), and is recorded by the photodiode (9). As discussed in section 3.1, the signal is now modified by the bias-tee (10), an amplifier (11), the mixer (12), and the low-pass filter (13) in order to create the error signal. The error signal can then be taken from one of the four SMA-outputs and fed into the external PID and laser control. By feeding that information back to the laser, it can be stabilised on the set frequency and can be used for further experiments that need a frequency-stabilised laser in order to work. For this, the main part of the laser power is set to be reflected at the PBS inside the laser box and coupled into fibre port B for further use.

4.2. Choice of components, dimensions and materials

All dimensions are given in millimetres and sizes for screws and nuts are given with respect to the metric unit system.

The laser box measures 129×234×61 mm, 129×251.7×61 mm considering the additional 17.7 mm from the fibre port. The spectroscopy box measures 144×189×61 mm (144×206.7×61 mm including the fibre port). These dimension are a result of the choice of components which, for instance, all measure less than 50mm in height. The aim was to include as many conventional components as possible. Thus, fewer parts need to be customised, keeping the costs and effort of the production to a minimum. The centres of the diode laser, the fibre ports and the photodiode are placed 26 mm above the base plate. This determines the height of the laser beam and, therefore, the height of the optical axis of the remaining optical components.

There is a gap after each optical components, in order to fit a measurement device. This is especially important when setting up and adjusting the modules and for simplifying repairs.

In the laser box, fibre port B was placed on the same wall as the fibre port A. However, putting another mirror which reflects the laser beam onto that wall increases the outline dimensions (at least 1/4 of the width could be removed). This was chosen so that only two walls have inputs and outputs, and that those two walls are on opposite sides. This makes the box easier to store and, especially, makes it easier to secure it to a place by clamping it from two sides. The same argument applies to the spectroscopy box, where the SMA outputs are put onto the same wall as fibre port C.

The companies and exact models of the implemented commercial optical and electrical components are listed in Table A.5. They were chosen, so that they can easily be mounted and satisfy the dimensional requirements. For instance, the mirror mounts were chosen so that the mirrors can be adjusted and secured by an Allen key from the top. Like this, less space is required in between the individual components.

The used photodiode has an externally threaded housing with a SM05-thread. With this it can directly be screwed into the septum and secured there. Unfortunately, in the technical drawing of the corresponding wall in section A.4.4 this could not be implemented with the used software in time, as this specific thread type is not supported and will have to be induced manually.

The customised parts that optimise the design will be discussed in more detail.

4.2.1. Fastening assemblies

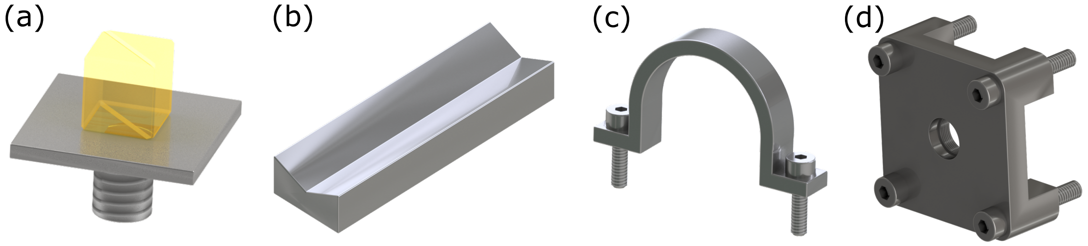

Figure 4.2.: (a) Polarising beam splitter on its mounting plate. (b) Mounting rail for the Rubidium vapour cell. (c) Mount for the low-pass filter onto the wall. (d) Mount for the converging lens onto the wall.

In order to ensure the modifiability of the setup, we choose a modular design for every part. With this, each component can be disassembled into several parts. This has the advantage of being able to replace individual parts if they are broken without having to replace the whole assembly. Also, if the modules are not in use, parts of them can be adapted to other setups.

For instance, as shown in Figure 4.2a, the PBS is to be glued to a little plate made of stainless steel (12.7×12.7×1 mm) using epoxy resin, which can then be screwed into any 1/2"-post using a M4-screw.

The same procedure is performed for the Rubidium vapour cell. As it is a cylindrical component, a rail of stainless steel with a slight extrusion was designed where the component can be glued into, as illustrated in Figure 4.2b. Again, the rail can be connected to any 1/2”-post by a M4-screw. The technical drawings with the corresponding dimensions can be found in the section A.4.4.

As the low-pass filter needs to be secured as well but does not have positional constraints, a mount was designed which fastens it to the septum. This mount can be seen in Figure 4.2c. It consists of an arch of stainless steel (inner radius: 2 mm, thickness: 2 mm, width: 5 mm) and can be screwed onto the wall with M2-screws.

The converging lens, with an effective focal length of f = 3.1 mm, needs to be mounted in front of the DFB laser. For that, we design a mounting system as shown in Figure 4.2d (outline: 40×40 mm, plate: 6mm, posts: 9.2 mm). The lens is screwed into the mount by its outer M9-thread and secured there. The M4-screws used for attaching the mount to the septum allow us to adjust the distance to the laser exit in the optical axis.

All fastening assemblies are made of stainless steel to ensure maximum stability.

4.2.2. Mounts for the optical components

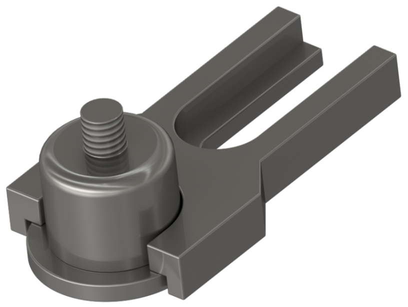

Figure 4.3.: Mount for optical components, consisting of the post and the clamping fork.

The mounts for the optical components, shown in Figure 4.3, were designed to give maximum stability while ensuring freedom in orientation and minimum dimension. For stability, the posts, as well as the clamping forks are made of stainless steel. Each post consists of two parts. The base part with a height of 2 mm and a 16.7 mm diameter can be connected to any commercial 1/2”-post by a M6-threaded extrusion. The added 1/2”-post varies in height, depending on the component it is used for. For the PBS a conventional 20 mm post can be used, while the post for the optical isolator, the mirrors, the wave plates and the vapour cell were especially designed and need to be fabricated, as shown in Table 4.1. The detailed dimensions of the mounts can be found in section A.4.4.

1/2”-posts

Part	Height
Isolator	7 mm
Mirrors	8 mm
Wave plates	9 mm
Vapour cell	10 mm
PBS	20 mm

Table 4.1.: Heights for all used 1/2”-posts. PBS: polarising beam splitter.

The design of the clamping forks is based on conventional ones but adapted to the dimensions of our setup. To be exact, they fix the 1/2”-posts with the 16.7 mm base-post of 2 mm height to the base plate with M4-threaded holes with 15mm-spacing. The height of 5 mm ensures stability. The rail, measuring 17 mm in length, secures the corresponding optical component independent of its position on the base plate. This is achieved by fixing the clamping fork to a hole in the base plate using a M4-screw with a round nut for protection. In order to keep the space needed to secure the optical components to a minimum, we decided not to use commercial clamping forks, as no model was found which would ensure the same module dimension.

4.2.3. Base plate, walls and lid

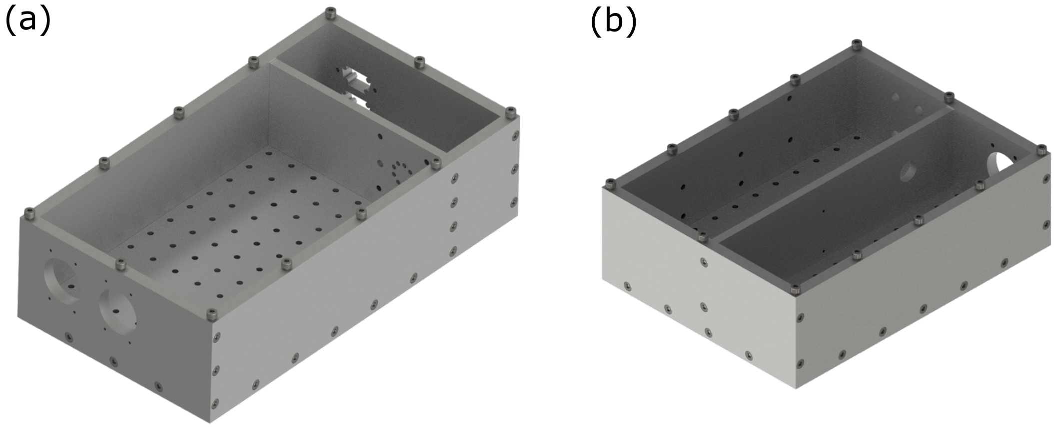

Figure 4.4.: Assembly of (a) the laser-box and (b) the spectroscopy-box. The lid is removed for visibility purposes.

The base plate and the walls are shown in Figure 4.4. The base plate measures 205×155 mm for the laser box, 175×130 mm for the spectroscopy-box, with a thickness of 10 mm. Starting at 5 mm from two perpendicular edges, a M4-threaded hole can be found every 15 mm into both directions, creating a grid over the whole plate.

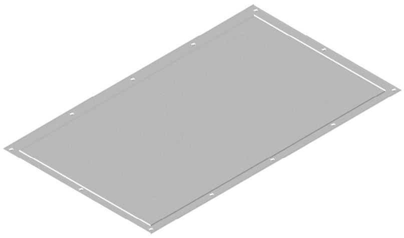

Figure 4.5.: Lid of the spectroscopy box.

The side walls measure 219×60×7 mm and 115×60×7 mm for the laser-box and 189×60×7 mm and 130×60×7 mm for the spectroscopy-box. They are secured to the sides of the base plate and to each other by M3-screw. M3-threaded holes are drilled into base plate and match holes into the walls for this purpose. As the short walls will be holding the fibre ports, as well as the in- and outputs, additional holes need to be implemented.

The walls separating the optical setup from the electronics are 5 mm thick and are also secured by M3-screws to the side walls. They measure 115×49 mm for the laser-box and 175×49 mm for the spectroscopy-box. The exact positioning dimensions can be found in section A.4.4. As the septa will hold the diode laser or, respectively, the photodiode and low-pass filter, additional holes are implemented and threaded where necessary.

The lid of the spectroscopy box is examplarily shown in Figure 4.5. It has the same outline dimensions as the corresponding box and measures 2 mm in thickness. Where it touches the outside walls, it is only 1 mm thick and can be fixed to them by M3-screws. For that, holes with a 3.4 mm diameter are implemented. It is designed to be made of Plexiglas which ensures enough stability but still allows us to look inside the box during operation. This can be useful in case errors occur.

The material for the base plate and and the walls was chosen to be black anodised aluminium. Aluminium is an inelastic and stable metal which comes with the benefit of being light at the same time. Due to laser safety, the metal is chosen to be anodised. In case of the laser beam unexpectedly hitting the surfaces of the box, just a fraction of the light will be reflected.

5. Conclusion and outlook

In the frame of this work, we were able to design a miniaturised frequency-stabilised diode laser. We introduced the concepts of saturated absorption spectroscopy and the corresponding laser frequency stabilisation method. We discussed the advantages and disadvantages of using frequency stabilisation spectroscopy and modulation transfer spectroscopy for the laser stabilisation. All tested versions proofed to be sufficient for the laser stabilisation, so we considered the setup size to be a crucial parameter. As a result we implemented a retroreflective version of the frequency modulation spectroscopy setup, introduced as the retroreflective saturated absorption spectroscopy, into the final version of the miniaturised design. The final design consists of two individual modules, one containing the fibre-coupled distributed feedback laser and one holding the spectroscopy setup and the electronics needed for the frequency stabilisation. They can be connected through an electro-optic modulator for the performance of the laser frequency stabilisation. This design was chosen for the flexibility in also using the portable laser without frequency stabilisation.

The dimensions of each module are approximately the size of a book. This is both manageable and leaves room for optimisation. For instance, the electronics could be implemented using a circuit board instead of individual devices. This could reduce the size of the spectroscopy module by half and therefore increase the flexibility in storage and transportation. This was not yet implemented due to time issues, as the designed module still serves our purpose.

The size of both modules could, in principle, be further reduced by carefully determining the exact position and produce customised components. Instead of using a base plate with equally spaced holes and clamping fork which can be attached to them, the base plate could be designed with holes in the calculated positions. Like this, the mounted optical components could be directly fixed to the base plate and the space needed for the clamping forks could be saved. This would require maximum precision and neglects aspects in mounting flexibility. As we set our preferences on using as many commercial components as possible and ensure flexibility of the setup, we decided not to design this version.

If the frequency-stabilised laser module is to be used in environments with extreme conditions, the embedding of the vapour cell needs to be adjusted. In case of operation near a strong magnetic field, a layer of magnetic field shielding material, such as a μ-metal, should be wrapped around the cell. Wrapping additional coils around the vapour cell can also amplify this effect. For operations in environments with low temperature, heating wires should be placed around the vapour cell. For this, additional connectors need to be implemented into the design.

We stated the reasons for designing two separate modules. Nevertheless, one module containing the entire setup could also be realised. This would bring the advantage of reduced storage space and the electro-optic modulator already being included inside the module. Like this, the module would only need to be connected to the laser control.

The design is the first step of the realisation of the frequency-stabilised diode laser. Now, the parts need to be fabricated, the modules need to be mounted and the optics need to be adjusted. Then, the frequency-stabilised laser modules can be used for the desired purposes.

A. Appendix

A.1. Scan time to frequency units conversion in Rubidium spectra

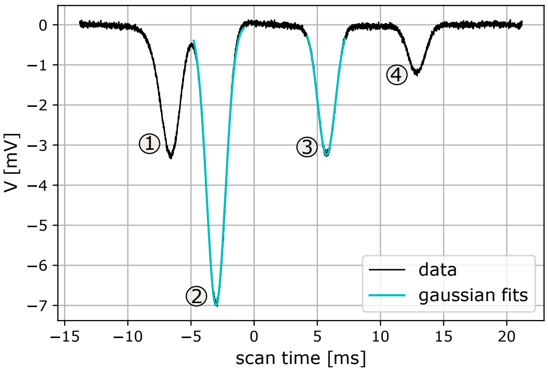

Figure A.1.: Absorption spectrum of the Rubidium D2 line with Gaussian functions fitted to the ^{85} transitions.

The spectra of the Rubidium probe, as shown in Figure 2.7, are recorded with an oscilloscope which measures the voltage received by the photodiode in units of scan time. As we are interested in the atomic transitions depending on their relative frequencies, we need to convert the time scale in milliseconds into a frequency scale in megahertz.

Looking at Figure A.1, we find four dips in our spectrum, which can be approximated by a Gaussian profile:

$$f(t) = A \cdot exp(-\frac{(t-t_0)^2}{2\sigma^2}, \qquad (A.1)$$

where A denotes the amplitude, x_0 the position on the x-axis and σ the standard deviation. We know that our Rubidium probe consists of the natural isotopic mixture of 72.2% ^{85}Rb and 27.8% ^{87}Rb. Due to the isotopic abundance, we can assume that more light will be absorbed by the ^{85}Rb atoms. We also know that the frequency splittings between the hyperfine ground energy level $5^2\mathrm{S}_{1/2}$ is 3.035 GHz for ^{85}Rb and 6.8 GHz for ^{87}Rb [14][15]. Using this assumption, we can assign peak 2 and 3 in Figure A.1 to ^{85}Rb. In the same way peak 1 and 4 can be assigned to ^{87}Rb. Fitting a Gaussian function to the peaks of ^{85}Rb as indicated in Figure A.1, gives us a distance between their minima of 8.780 ms (see Table A.1 for all fit parameters). We calculate the conversion factor ξ as

$$\xi = \frac{3035.732\mathrm{MHz}}{0.00878\mathrm{s}} = 346.941\frac{\mathrm{MHz}}{\mathrm{s}}. \qquad (A.2)$$

Multiplying the scan time by ξ we can convert the time units into frequency units. Alternatively this could be done using the ^{87}Rb-peaks and the value of the difference between the $5^2\mathrm{S}_{1/2}$ levels of ^{87}Rb.

Accordingly, the x-axis in all spectral graphs have been converted by this method using Figure 2.5 as a reference. The peaks and values are listed for all graphs in Table A.2.

	Left peak (^{85}Rb F = 3)	Right peak (^{85}Rb F = 2)
A [mV]	-7.001±0.009	-3.251±0.004
t_0 [ms]	-3.019±0.001	5.731±0.001
σ [ms]	0.739±0.001	0.692±0.001

Table A.1.: Table containing all values from the Gaussian fits in Figure A.1, obtained with Python. All values are rounded to 3 decimal digits.

Figure	**scan time peak 1** [ms]	**scan time peak 2** [ms]	ξ [$\frac{MHz}{s}$]
2.7a	-3.019	5.731	346.941
2.7b	-2.980	5.715	349.135
3.3	-2.658	-1.667	201.911
3.5	-2.450	-1.885	353.982
3.8b	-2.658	-1.667	119.942
3.9	0.685	0.785	2000

Table A.2.: Conversion factors for all graphs where scan time needs to be changed into units of frequency with the method explained in section A.1. All values are rounded to 3 decimal digits. For the error signals, the zero-crossings of two transitions were used as reference. The the MTS error signal, transitions in the corresponding absorption spectrum were used, as they were measured with the same time scale.

A.2. Plotting methods and error determination

The plotting of graphs and analysis are conducted using the programming language python with the libraries NumPy, Matplotlib, and SciPy.

The data is read into NumPy arrays. Fitting errors are obtained using the library SciPy, specifically scipy.optimize.curve_fit that uses least squares to fit a user-defined function to data with specified errors.

The error propagation of a variable $f(\vec{x})$ with known errors $\Delta x_1, \Delta x_2, ..., \Delta x_n$ is calculated via

$$\Delta f(\vec{x}) = \sqrt{\left(\frac{\partial f}{\partial x_1}\Delta x_1\right)^2 + \left(\frac{\partial f}{\partial x_2}\Delta x_2\right)^2 + ... + \left(\frac{\partial f}{\partial x_n}\Delta x_n\right)^2}. \qquad (A.3)$$

A.3. Derivation of important formulas

A.3.1. Derivation of Equation 2.15 in section 2.4.2

Starting with

$$\begin{aligned} E_C(t) = E_0\{&exp(-\delta_0)cos(\omega t-\phi_0)+\frac{M}{2}exp(\delta_1)cos[(\omega+\omega_m)t-\phi_1] \\ &-\frac{M}{2}exp(-\delta_{-1})cos[(\omega-\omega_m)t-\phi_{-1}]\} \end{aligned} \tag{A.4}$$

can be converted into intensity by using

$$I = c\epsilon E_C^2. \tag{A.5}$$

This results in

$$\begin{aligned} I(t) = c\epsilon E_0^2\{&exp(-2\delta_0)cos^2(\omega t-\phi_0)+M\,exp(-\delta_0-\delta_1)cos[(\omega+\omega_m)t-\phi_1]cos(\omega t-\phi_0) \\ &-M\,exp(-\delta_0-\delta_{-1})cos[(\omega-\omega_m)t-\phi_{-1}]cos(\omega t-\phi_0)\}+\mathcal{O}(M^2), \end{aligned} \tag{A.6}$$

when omitting terms of second order in M. Using the trigonometric property

$$cos\alpha cos\beta = \frac{1}{2}[cos(\alpha-\beta)+cos(\alpha+\beta)] \tag{A.7}$$

$I(t)$ can be rewritten into

$$\begin{aligned} I(t) = \frac{c\epsilon E_0^2}{2}\{&exp(-2\delta_0)[1+cos(2\omega t-2\phi_0)] \\ &+M\,exp(-\delta_0-\delta_1)[cos(2\omega t+\omega_m t-\phi_1-\phi_0)+cos(\omega_m t-\phi_1+\phi_0)] \\ &-M\,exp(-\delta_0-\delta_{-1})[cos(2\omega t-\omega_m t-\phi_{-1}-\phi_0)+cos(\omega_m t-\phi_{-1}+\phi_0)]\}. \end{aligned} \tag{A.8}$$

The photodetector is not able to resolve terms containing 2ω. This results in

$$\begin{aligned} I_{PD} = \frac{c\epsilon E_0^2}{2}&exp(-2\delta_0)[1+M\,exp(-\delta_0-\delta_1)cos(\omega_m t-\phi_1+\phi_0) \\ &-M\,exp(-\delta_0-\delta_{-1})cos(\omega_m t-\phi_{-1}+\phi_0)]. \end{aligned} \tag{A.9}$$

With the trigonometric property

$$cos(\alpha-\beta) = cos\alpha cos\beta + sin\alpha sin\beta, \tag{A.10}$$

we get the follwing equation:

$$\begin{aligned} I_{PD} = c\epsilon E_0^2&exp(-2\delta_0)\{1 \\ &+Mcos(\omega_m t)[exp(\delta_0-\delta_1)cos(\phi_1-\phi_0)-exp(\delta_0-\delta_{-1})cos(\phi_{-1}-\phi_0) \\ &+Msin(\omega_m t)[exp(\delta_0-\delta_1)sin(\phi_1-\phi_0)+exp(\delta_0-\delta_{-1})sin(\phi_{-1}-\phi_0)\}. \end{aligned} \tag{A.11}$$

Now taking into account that $|\delta_n-\delta_{n+1}| \gg 1$ and $|\phi_n-\phi_{n+1}| \gg 1$ gives us the final result of the Intensity I_{PD}, measured by the photo detector

$$I_{PD} = c\epsilon E_0^2 exp(-2\delta_0)[1+Mcos(\omega_m t)(\delta_{-1}-\delta_1)+Msin(\omega_m t)(\phi_1+\phi_{-1}-2\phi_0)]. \tag{A.12}$$

A.3.2. Derivation of Equation 2.16 in section 2.4.2

Starting from

$$V(t) = I_{PD} \cdot cos(\omega_m t), \tag{A.13}$$

we can implement Eq. 2.15 to obtain

$$\begin{aligned} V(t) = c\epsilon E_0^2 exp(-2\delta_0)[cos(\omega_m t) + M\, cos^2(\omega_m t)(\delta_{-1} - \delta_1) \\ + M\, cos(\omega_m t - \frac{\pi}{2})cos(\omega_m t)(\phi_1 + \phi_{-1} - 2\phi_0)]. \end{aligned} \tag{A.14}$$

Using the trigonometric property from Eq. A.7, which is

$$cos\alpha cos\beta = \frac{1}{2}[cos(\alpha - \beta) + cos(\alpha + \beta)], \tag{A.15}$$

this results in the desired formula for $V(t)$:

$$\begin{aligned} V(t) = c\epsilon E_0^2 exp(-2\delta_0)\{cos(\omega_m t) + \frac{M}{2}[1 + cos(2\omega_m t)](\delta_{-1} - \delta_1) \\ + \frac{M}{2}[cos(\pi/2) + cos(2\omega_m t - \pi/2)](\phi_1 + \phi_{-1} - 2\phi_0]\}. \end{aligned} \tag{A.16}$$

A.4. Tables and figures

A.4.1. Photos of the experimental setup

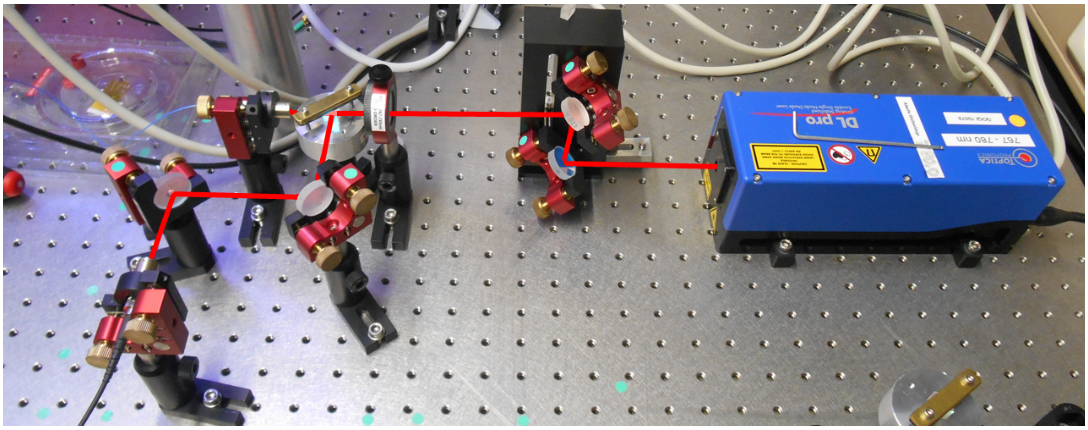

Figure A.2.: Light is coming from an external cavity diode laser (ECDL) is coupled into two fibres, with different light intensities.

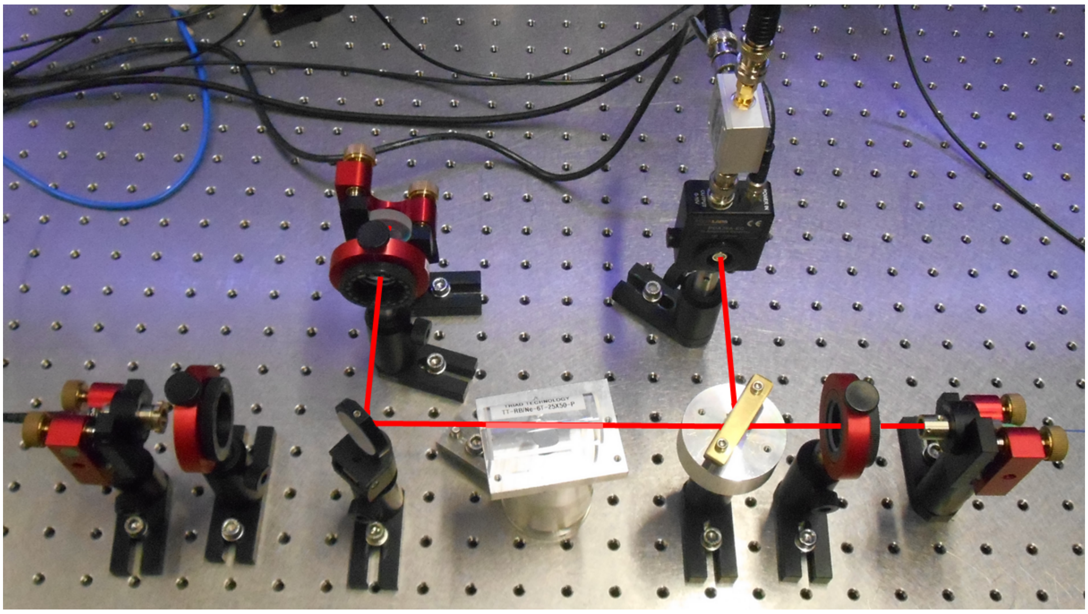

Figure A.3.: Photo of the setup in the laboratory showing the adjustable spectroscopy setup. Here we see the RRS version. By rotating the foldable mirror out of the laser beam, we are able to also perform FMS and MTS, as shown in Figure A.4.

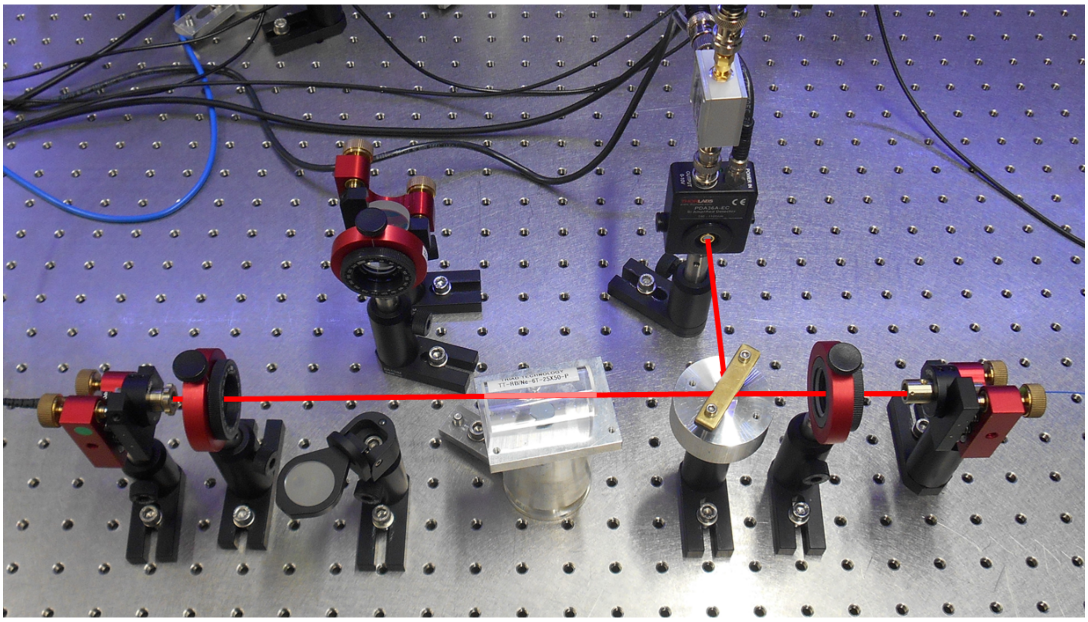

Figure A.4.: Photo of the setup in the laboratory showing the adjustable spectroscopy setup. Here we see the FMS and MTS version. By rotating the foldable mirror into the laser beam, we can perform RRS, as shown in Figure A.4.

A.4.2. Tables

Component	Company	Model
External cavity diode laser	Toptica	DL pro (780 nm)
Electro-optic modulator	iXblue	NIR-MPX800-LN-0.1
Photodiode	Thorlabs	PDA36A-EC
Bias-tee	Mini-circuits	ZFBT-6GW+
Amplifier	Mini-circuits	ZFL-500+
Mixer	Mini-circuits	ZFM-3-S+
Low pass filter	Mini-circuits	SLP-1.9+
Oscilloscope	Rohde & Schwarz	HMO724
Function generator	Rigol	DG1022
Laser control system	Toptica	DTC 110 (Temperature) DCC 110 (Current)
PID controller	Toptica	PID 110
Scan control	Toptica	SC 110

Table A.3.: Electrical components used in the experimental setup.

Section	Variable	Corresponding error value
3.2	P_{probe}/P_{probe}	$\sqrt{(\frac{\Delta P_{Pump}}{P_{Pump}})^2 + (\frac{P_{Probe} \cdot \Delta P_{Probe}}{P_{Pump}^2})^2}$
3.2.1 (FMS)	P_{probe}	0.005 mW
	P_{pump}	0.01 mW
	P_{tot}	0.01 mW
	ΔV	0.1 mV
3.2.2 (MTS)	P_{probe}	0.01 mW
	P_{pump}	0.01 mW
	P_{tot}	0.01 mW
	ΔV	0.1 mV
3.2.3 (RRS)	P_{tot}	0.01 mW
	ΔV	0.1 mV (for $P_{tot} < 0.5$ mW)
		0.2 mV (for $0.5 \neq P_{tot} < 1.5$ mW)
		1.0 mV (for $P_{tot} \leq 1.5$ mW)

Table A.4.: Error values used in the graphs in section 3.2. The formula for the error values of P_{probe}/P_{probe} is obtained as described in section A.2. The constant values were chosen, adapting to the scale of measure.

Component	Company	Model
Distributed feedback laser	Toptica	EYP-DFB-0780-00080-1500-TOC03-0005
Collimating lens	Thorlabs	C330TMD-B
Optical isolator	Thorlabs	IO-3D-780-VLP
Mirrors	Newport	05Q20BB.HR2
Mirror mount	Newport	HVM-05R
$\lambda/2$-wave plate	Newport	05RP32-780
$\lambda/4$-wave plate	Newport	05RP34-780
Wave plate mount	Radiant-dyes	RD-RM-S
Rubidium vapour cell	Thorlabs	GC25075-RB
Polarising beam splitter	Thorlabs	PBS052
PBS mounting post	Thorlabs	TR20V/M
Fibreport	Thorlabs	PAF2-A4B
Photodiode	Thorlabs	SM05PD1A
Bias-tee	Mini-circuits	ZX85-12G-S+
Amplifier	Mini-circuits	ZFL-500+
Mixer	Mini-circuits	ZLW-3+
Low pass filter	Mini-circuits	SLP-1.9+

Table A.5.: Commercial electrical, optical and mounting components used in the design of the miniaturised setup.

Place	**Type and Thread**	**Length**	**Amount**
Laser box			
Walls to base plate	Hexagon socket head cap screw M3	12 mm	18
Walls to walls	Hexagon socket head cap screw M3	12 mm	18
Lid to walls	Hexagon socket head cap screw M3	8 mm	12
Laser diode to wall	Hexagon socket head cap screw M3	8 mm	2
Lens with mount to wall	Hexagon socket head cap screw M4	25 mm	4
Fibreports to wall	Hexagon socket head cap screw M2	8 mm	8
Wave plate mount	Hexagon socket set screw M4	6 mm	3
Mirror mount to post	Hexagon socket head cap screw M4	8 mm	5
Clamps to base plate	Round nut, inner ∅ = 4.2 mm	-	10
Clamps to base plate	Hexagon socket head cap screw M4	12 mm	10
D-SUB to wall	Screws adaptive to D-SUB connector (M4)	8 mm	4
	D-SUB(f) 9CKT	-	1
	D-SUB(m) 9CKT	-	1
Spectroscopy box			
Walls to base plate	Hexagon socket head cap screw M3	12 mm	18
Walls to walls	Hexagon socket head cap screw M3	12 mm	12
Lid to walls	Hexagon socket head cap screw M3	8 mm	12
Fibreport to wall	Hexagon socket head cap screw M2	8 mm	4
Mixer to wall	Hexagon socket head cap screw M4	8 mm	4
Amplifier to wall	Hexagon socket head cap screw M4	8 mm	4
Bias-tee to wall	Hexagon socket head cap screw M4	8 mm	2
Low pass filter to wall	Hexagon socket head cap screw M2	8 mm	2
Wave plate mount	Hexagon socket set screw M4	6 mm	2
Mirror mount to post	Hexagon socket head cap screw M4	8 mm	1
Clamps to base plate	Round nut, inner ∅ = 4.2 mm	8	5
Clamps to base plate	Hexagon socket head cap screw M4	12 mm	5
	SMA(f) to SMA(f)	-	4

Table A.6.: Types and location of screws, nuts and adaptors used in the design of the miniaturised setup where (f) denotes female and (m) denotes male.

A.4.3. Pictures of the miniaturised design

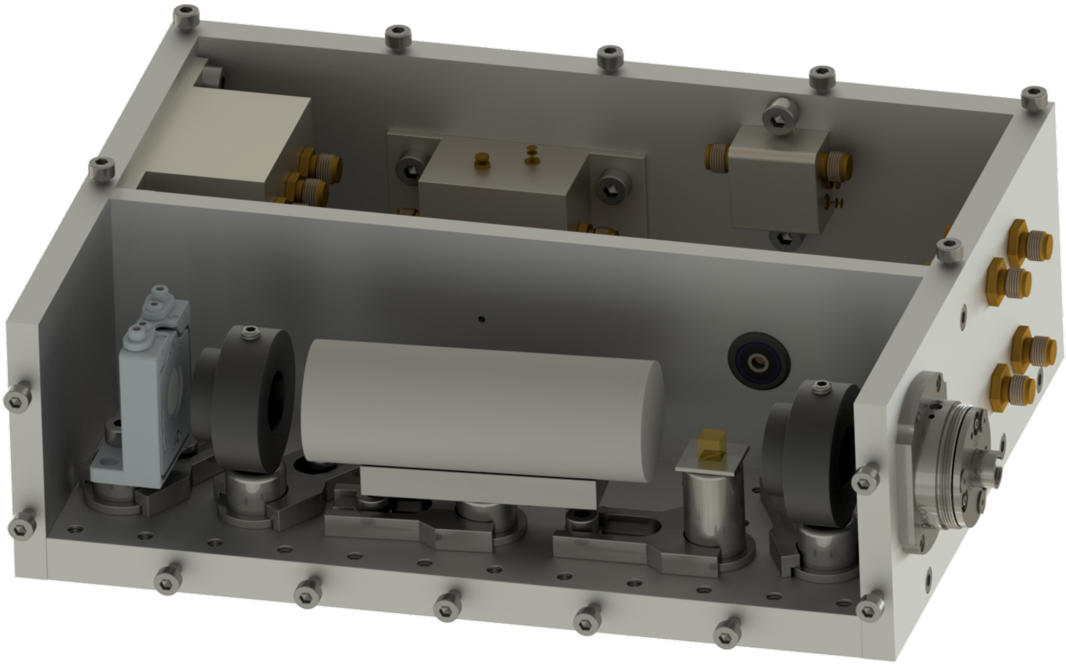

Figure A.5.: Rendered picture of the designed spectroscopy box. Here shown from an angle that shows the spectroscopy setup.

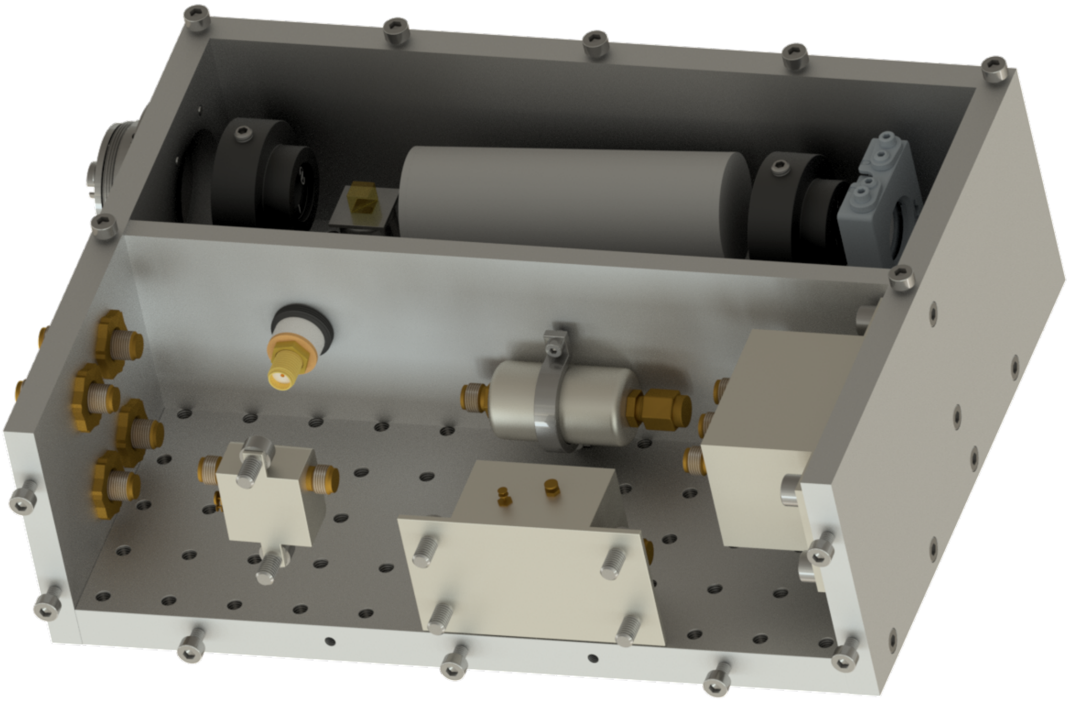

Figure A.6.: Rendered picture of the designed spectroscopy box. Here shown from an angle that shows the electronics.

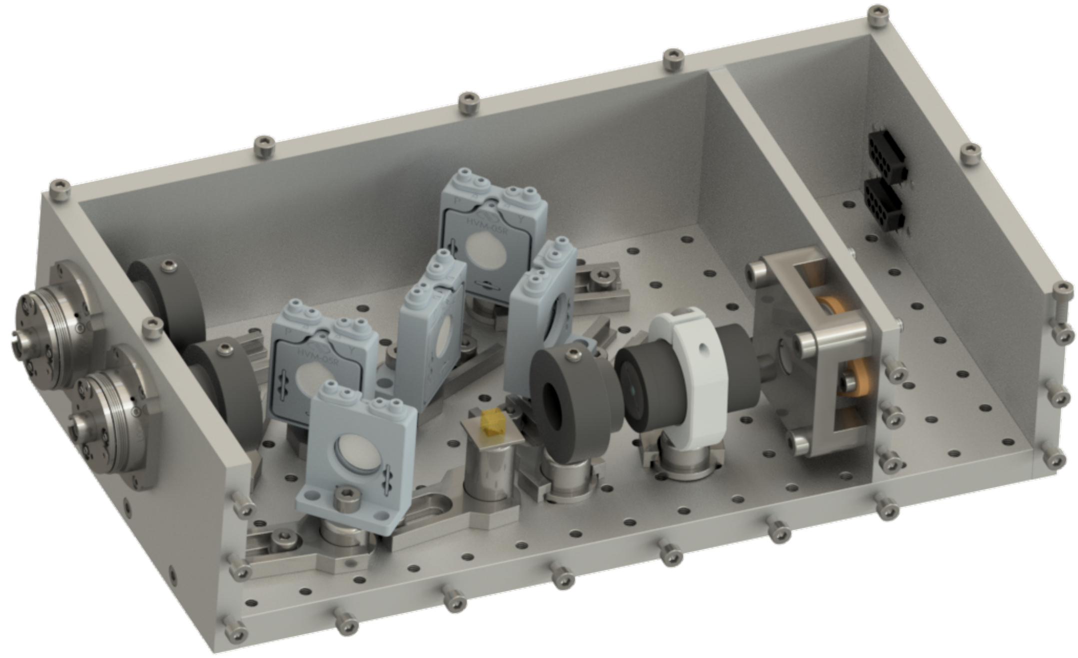

Figure A.7.: Rendered picture of the designed laser box. Here shown from an angle that shows the laser diode.

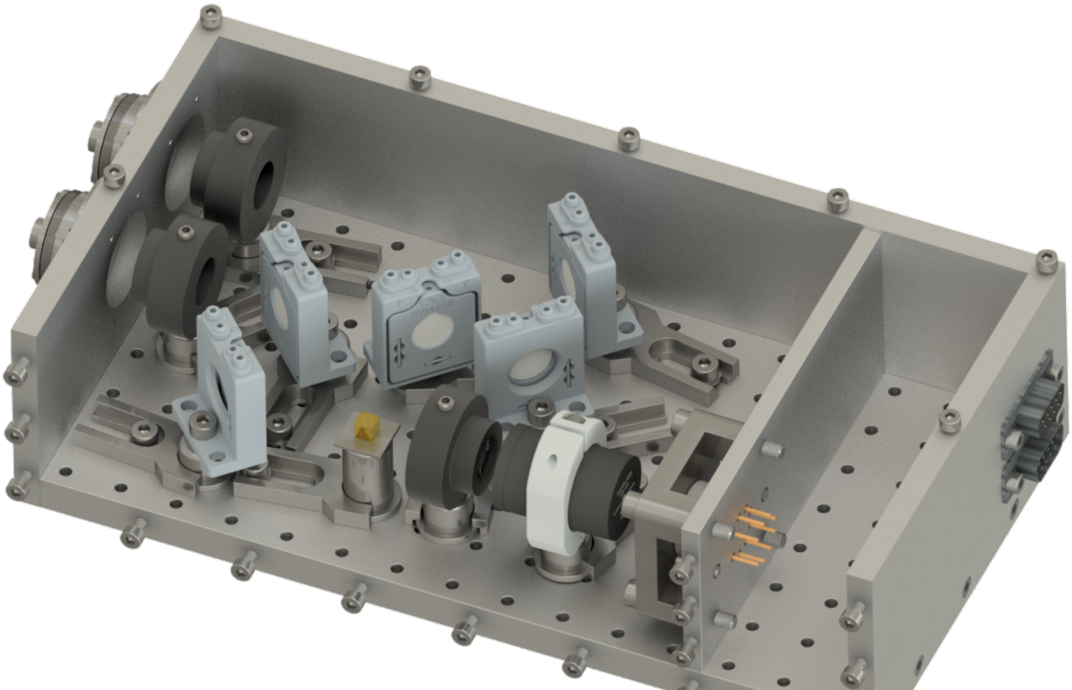

Figure A.8.: Rendered picture of the designed laser box. Here shown from an angle that shows the entrances of the fibre couplers.

A.4.4. Technical drawings of designed parts

See pages 52-75.

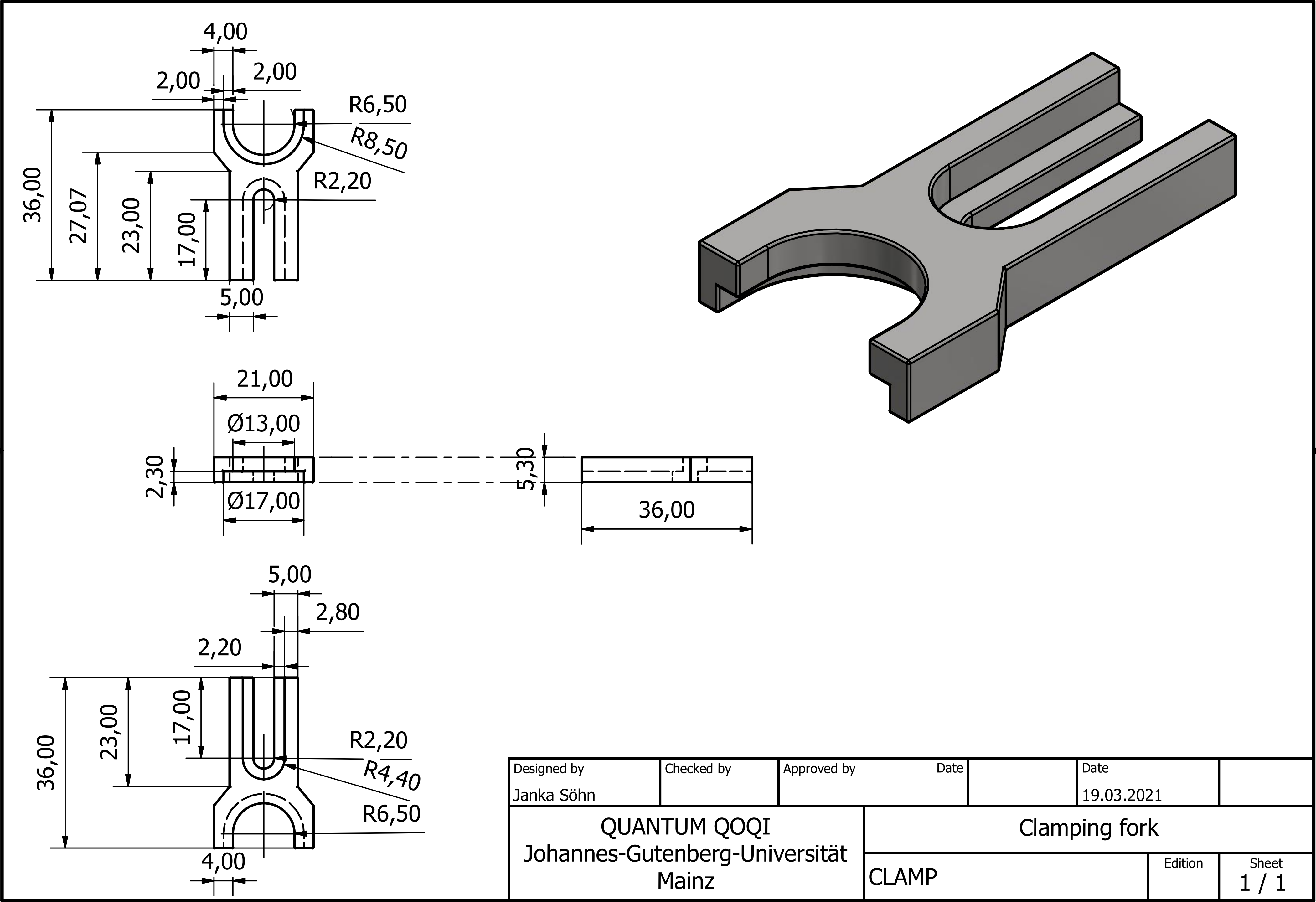

Designed by Janka Söhn	Checked by	Approved by	Date	Date 19.03.2021	
QUANTUM QOOQI Johannes-Gutenberg-Universität Mainz			Clamping fork		
			CLAMP	Edition	Sheet 1 / 1

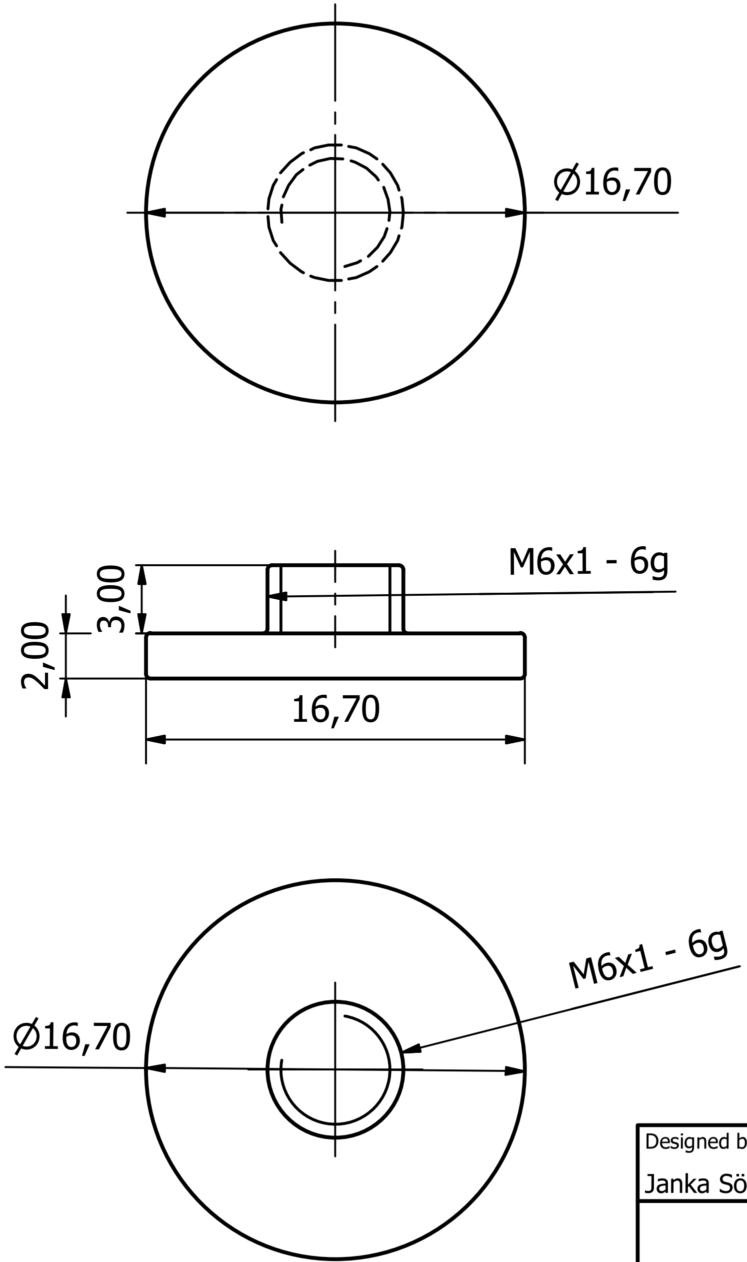

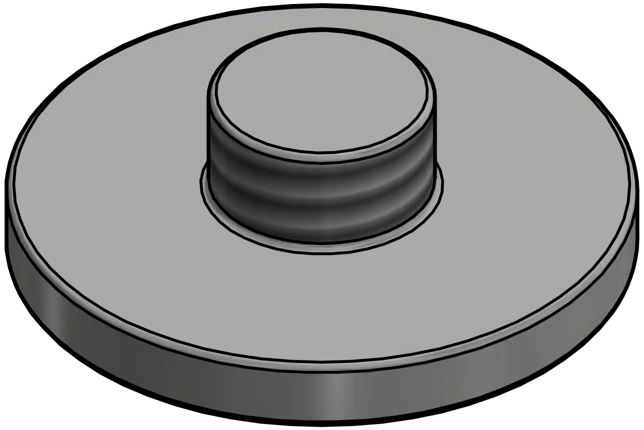

Designed by Janka Söhn	Checked by	Approved by	Date	Date 19.03.2021	
QUANTUM QOQI Johannes-Gutenberg-Universität Mainz		Base-post			
		Basepost		Edition	Sheet 1 / 1

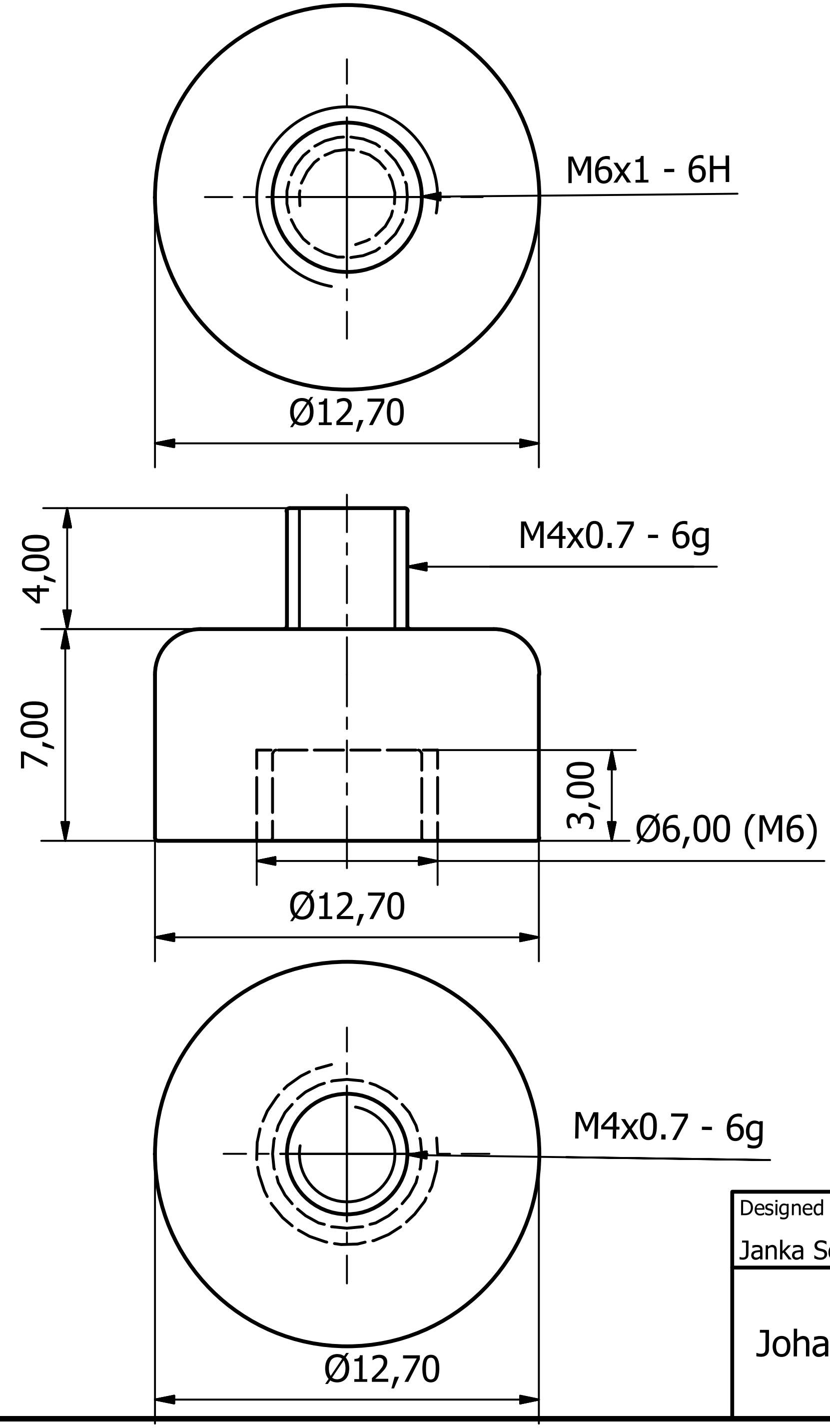

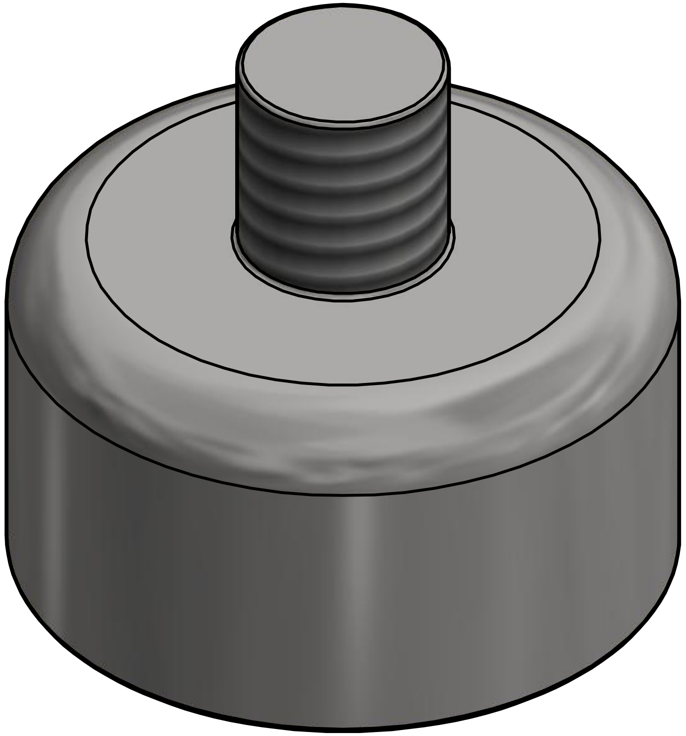

Designed by Janka Söhn	Checked by	Approved by	Date	Date 19.03.2021
QUANTUM QOQI Johannes-Gutenberg-Universität Mainz	1/2"-post for optical isolator			
	IsolatorPost		Edition	Sheet 1 / 1

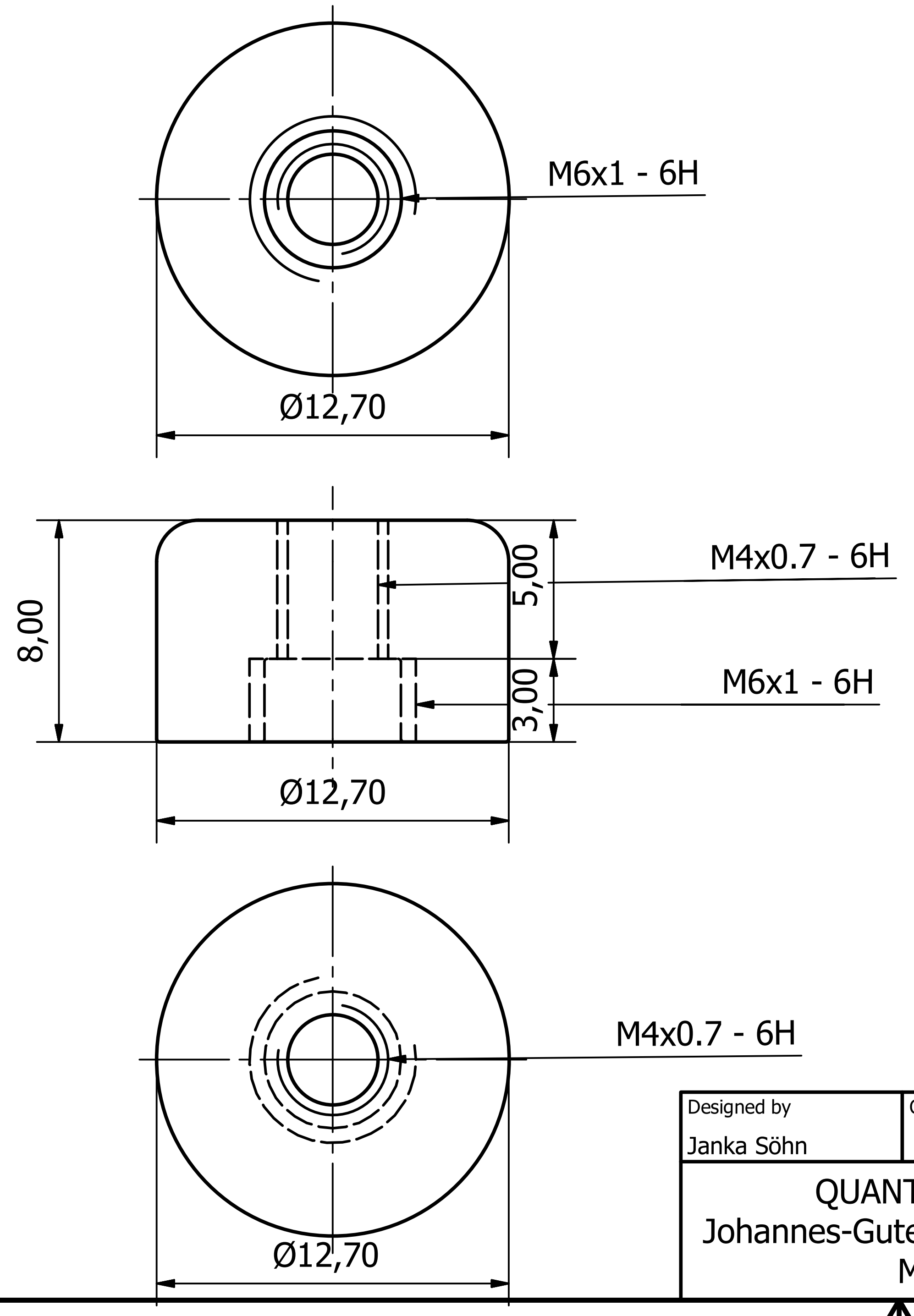

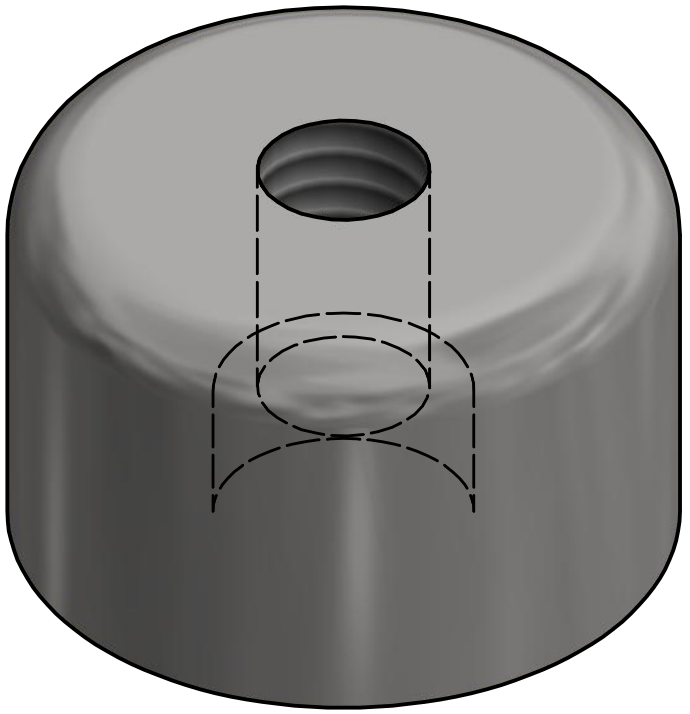

Designed by	Checked by	Approved by	Date	Date	
Janka Söhn				19.03.2021	

QUANTUM QOQI Johannes-Gutenberg-Universität Mainz	1/2''-post for mirrors		
	MirrorPost	Edition	Sheet 1 / 1

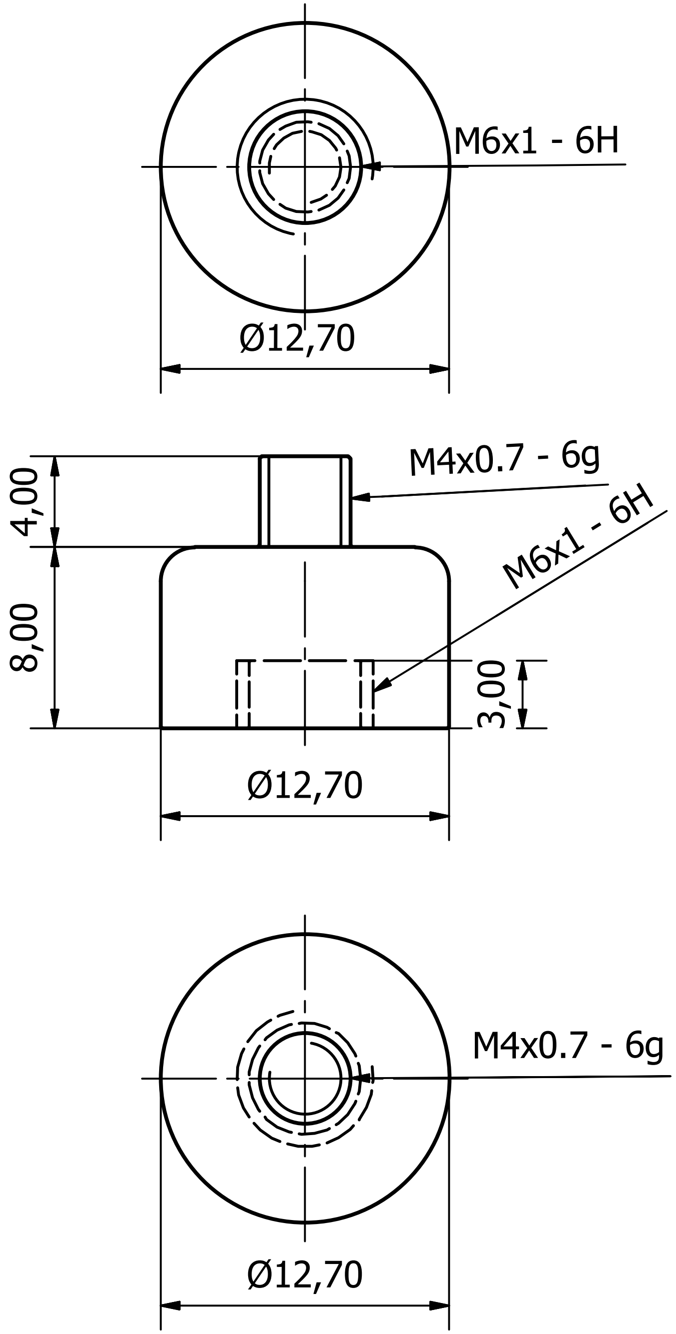

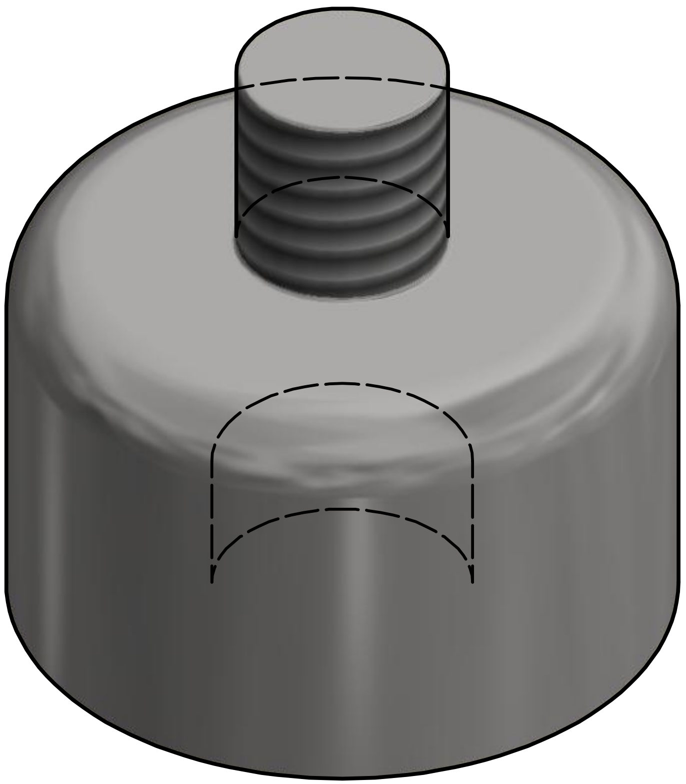

Designed by Janka Söhn	Checked by	Approved by	Date	Date 19.03.2021	
QUANTUM QOQI Johannes-Gutenberg-Universität Mainz			1/2''-post for rubidium vapour cell		
			RbcellPost	Edition	Sheet 1 / 1

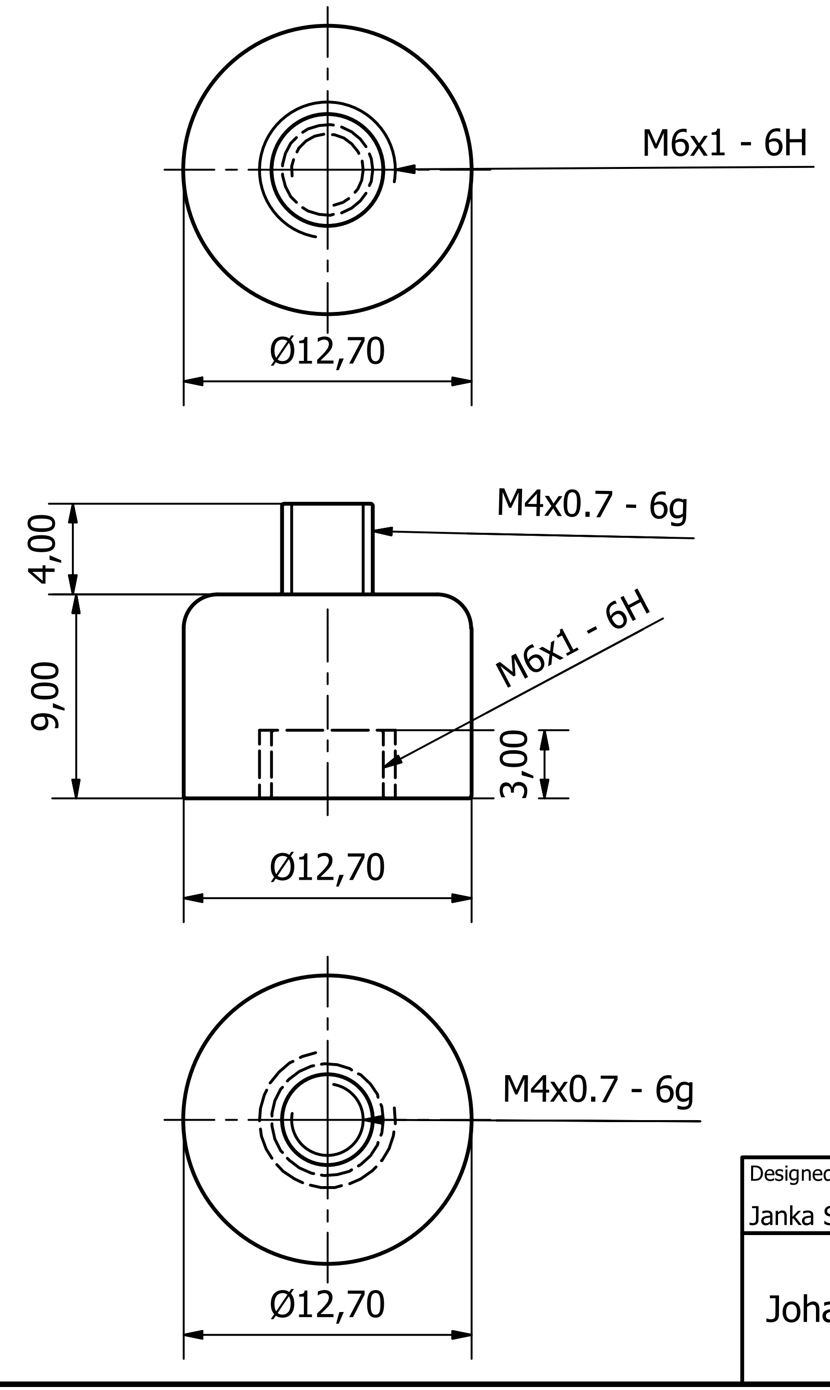

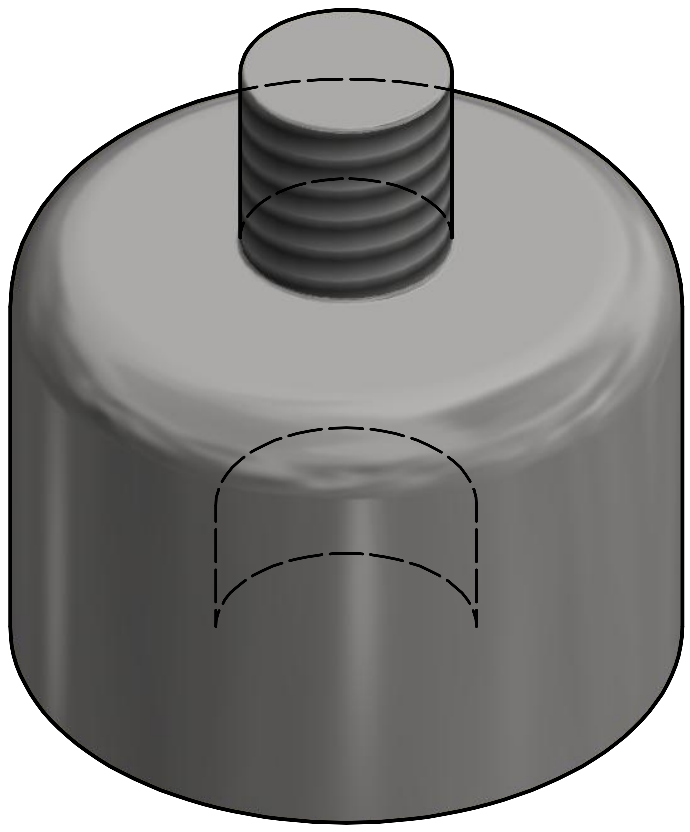

Designed by	Checked by	Approved by	Date	Date	
Janka Söhn				19.03.2021	

QUANTUM QOOQI
Johannes-Gutenberg-Universität
Mainz

1/2"-post for wave plates

	Edition	Sheet
WaveplatePost		1 / 1

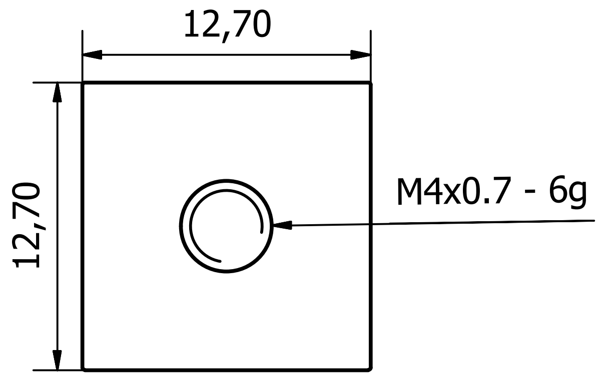

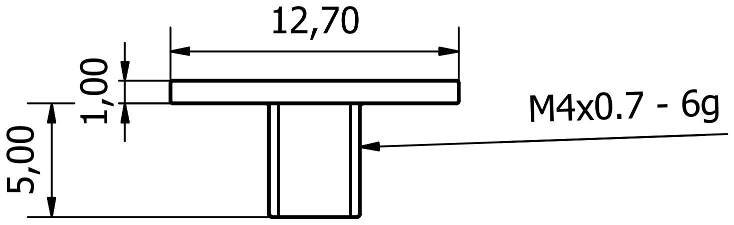

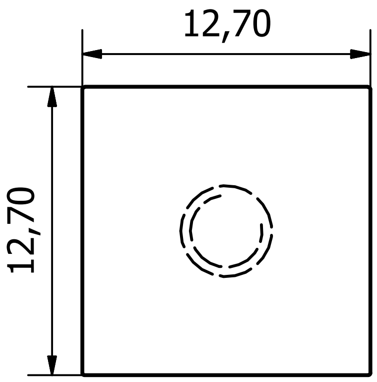

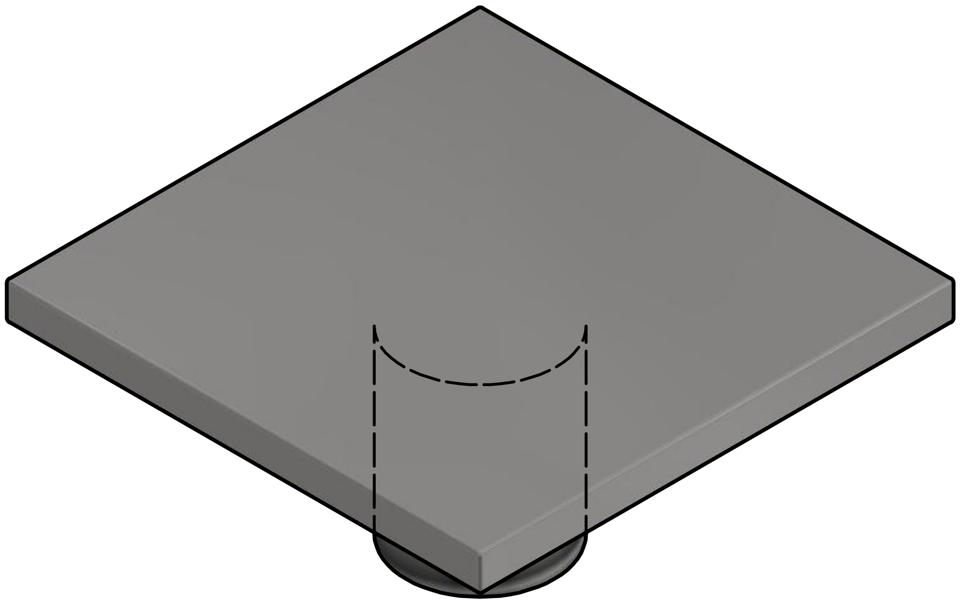

Designed by	Checked by	Approved by	Date	Date	
Janka Söhn				19.03.2021	

QUANTUM QOQI
Johannes-Gutenberg-Universität
Mainz

Mount for polarising beam splitter

	Edition	Sheet
PBSMount		1 / 1

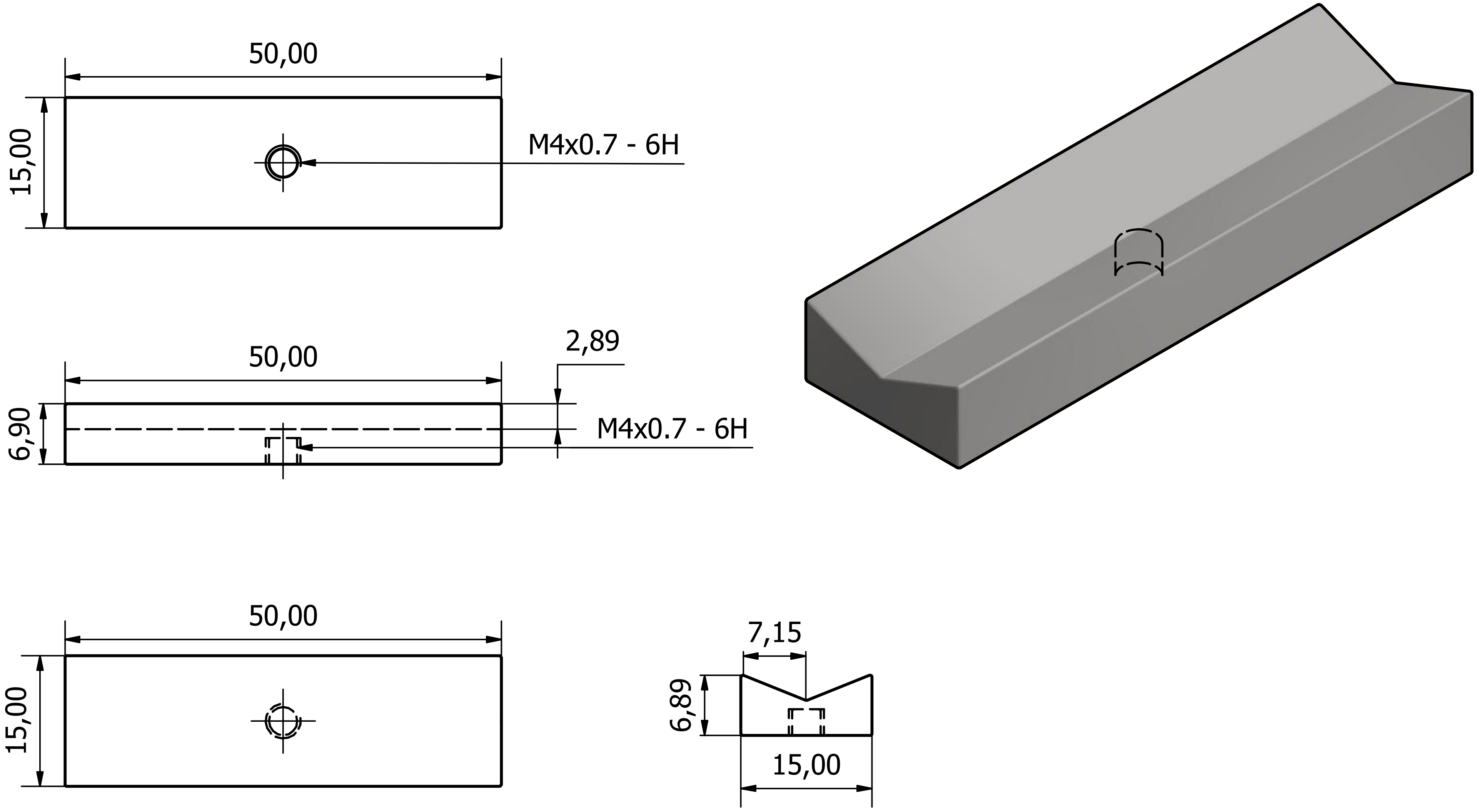

Designed by	Checked by	Approved by	Date	Date
Janka Söhn				19.03.2021

QUANTUM QOQI
Johannes-Gutenberg-Universität
Mainz

Mount for rubidium vapour cell

RbcellMount

Edition	Sheet
	1 / 1

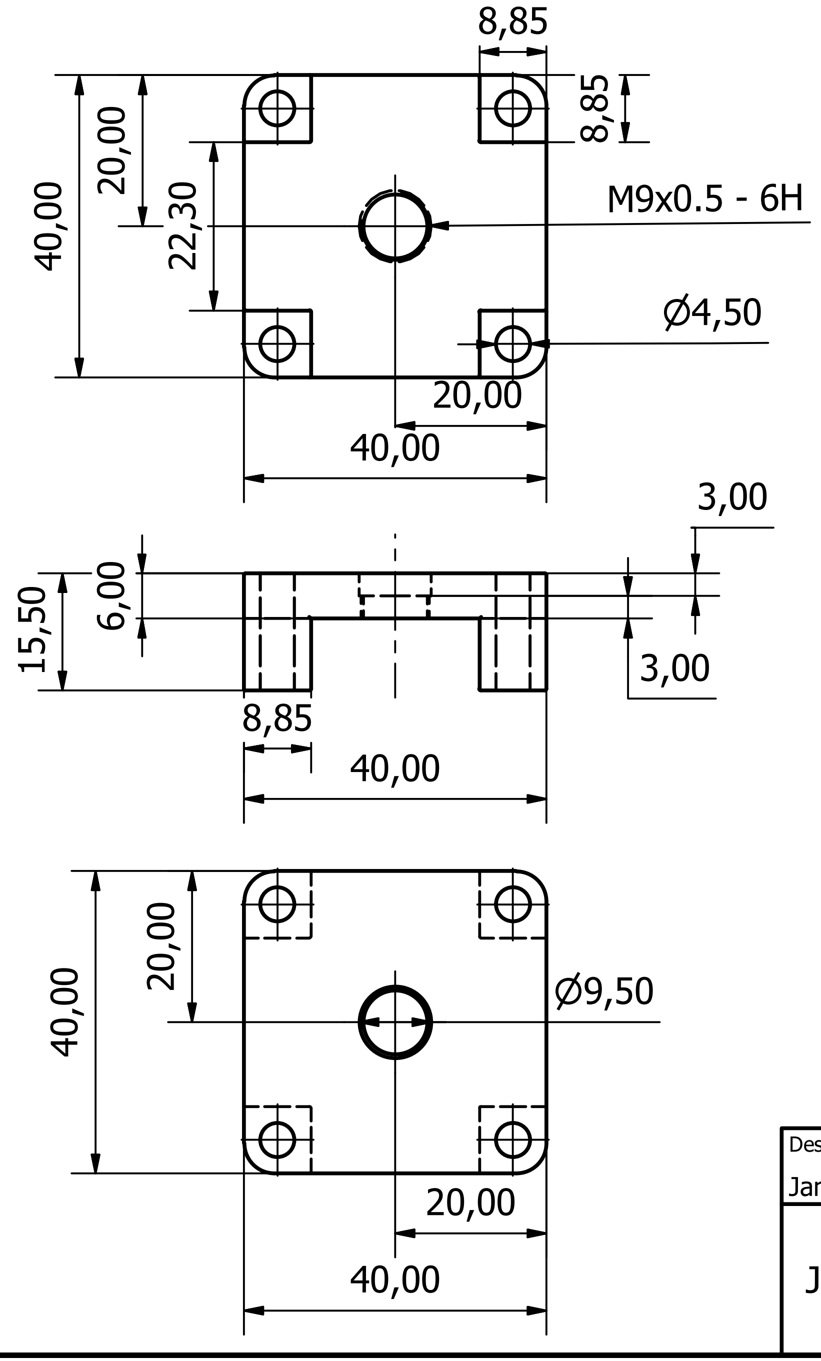

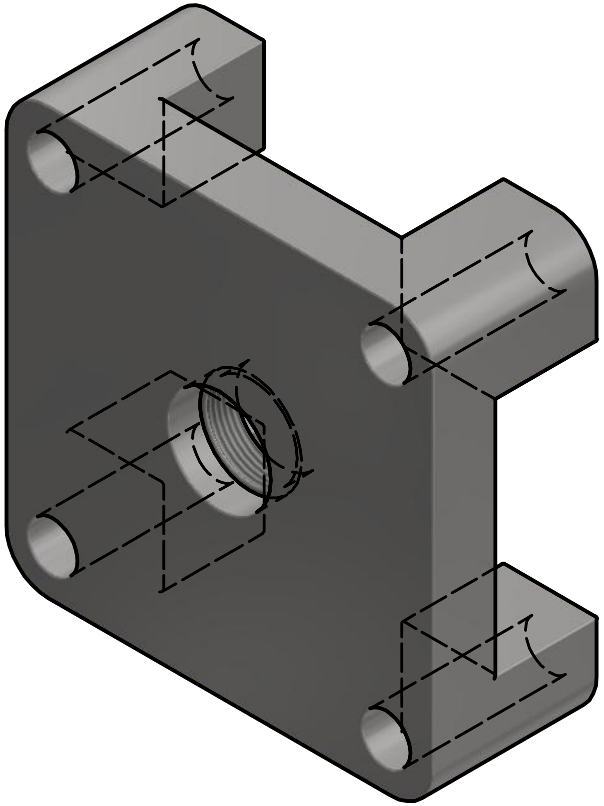

Designed by Janka Söhn	Checked by	Approved by	Date	Date 19.03.2021	
QUANTUM QOQI Johannes-Gutenberg-Universität Mainz			Mount for converging lens		
			LensMount	Edition	Sheet 1 / 1

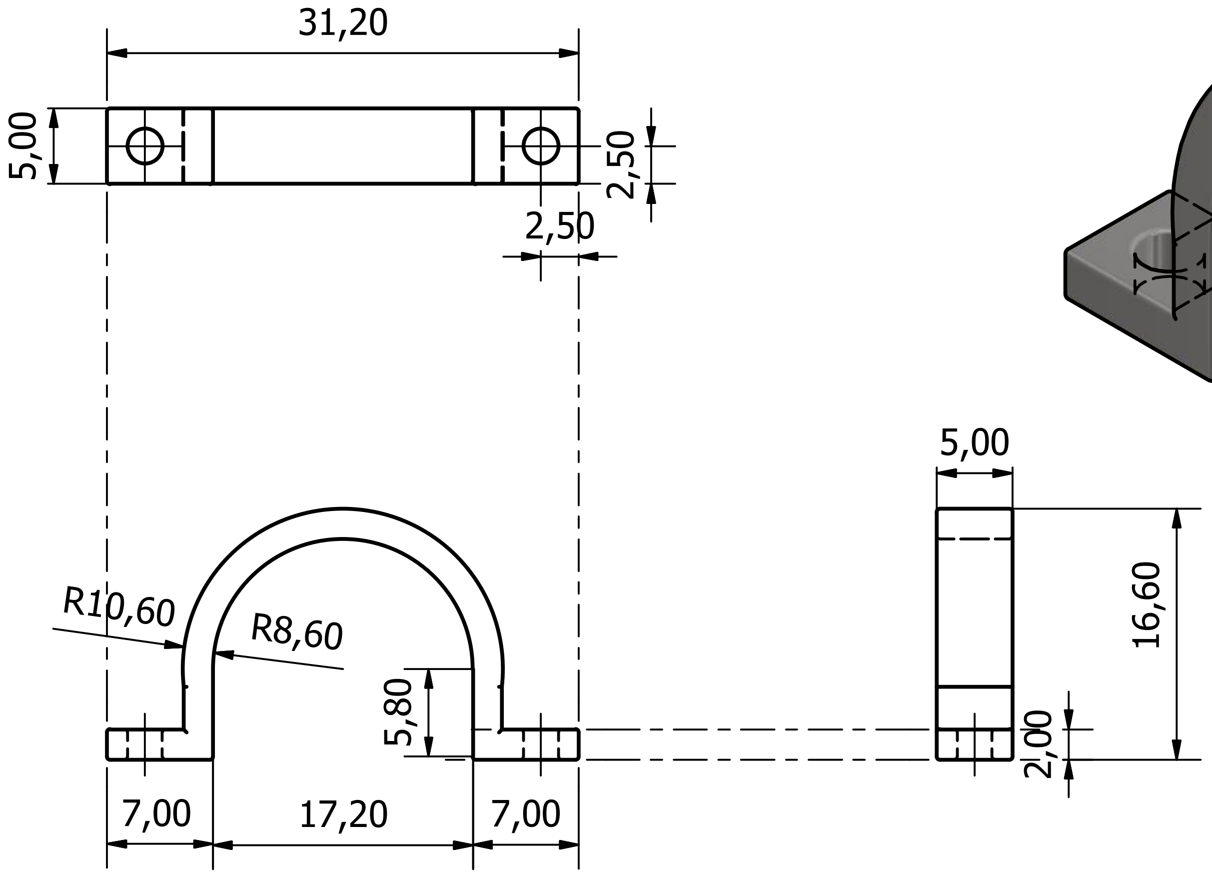

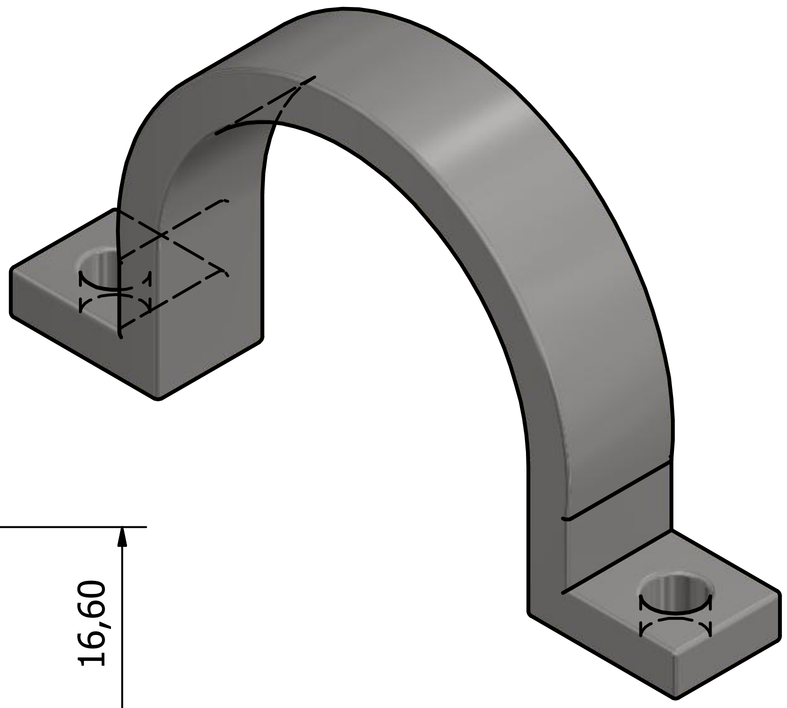

Designed by	Checked by	Approved by	Date	Date	
Janka Söhn				29.03.2021	

QUANTUM QOQI
Johannes-Gutenberg-Universität
Mainz

Mount for low-pass filter

	Edition	Sheet
LPFholder		1 / 1

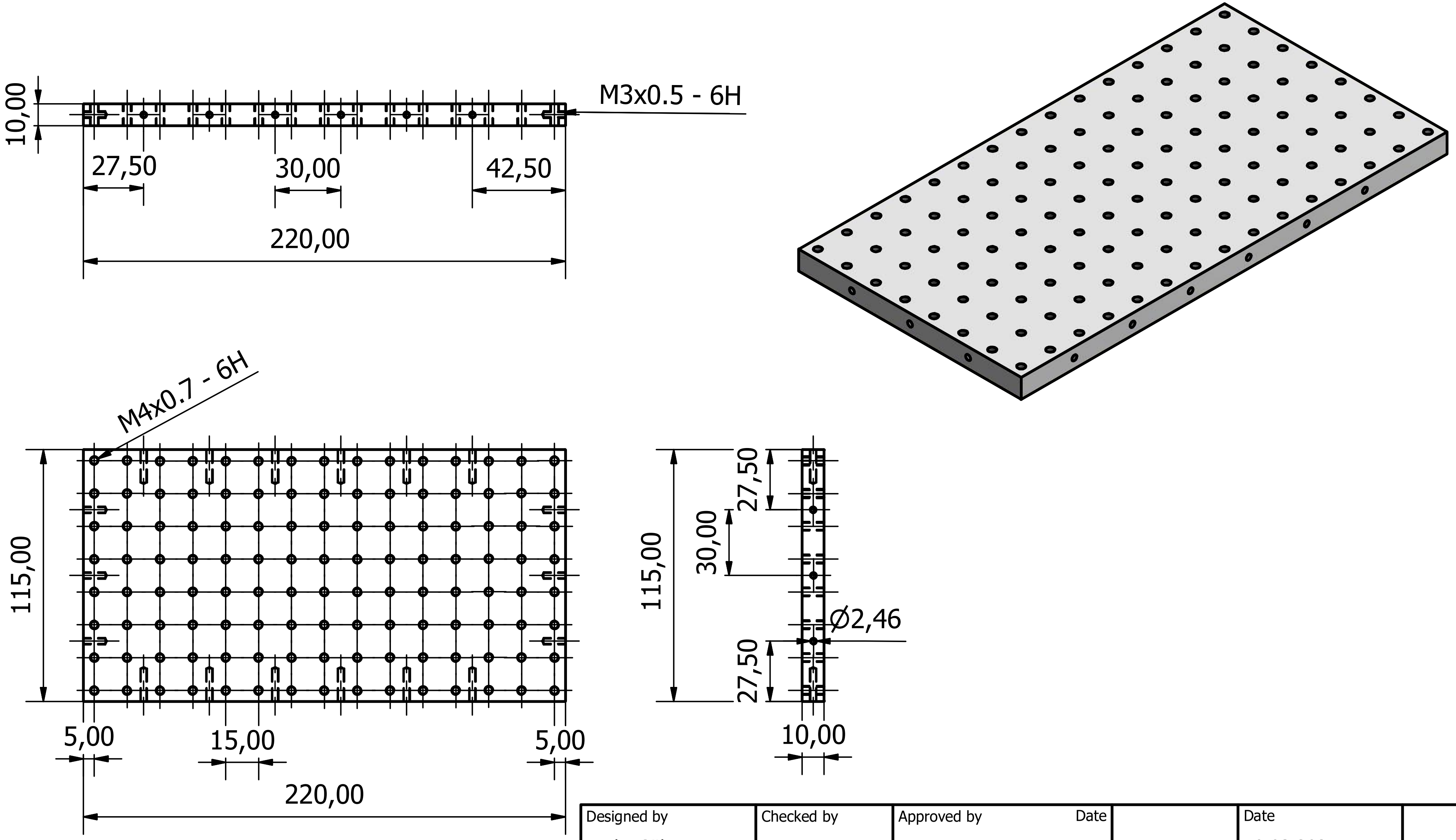

Designed by	Checked by	Approved by	Date		Date	
Janka Söhn					19.03.2021	

QUANTUM QOOQI Johannes-Gutenberg-Universität Mainz	Base plate of laser box		
	BaseplateLaserbox	Edition	Sheet 1 / 1

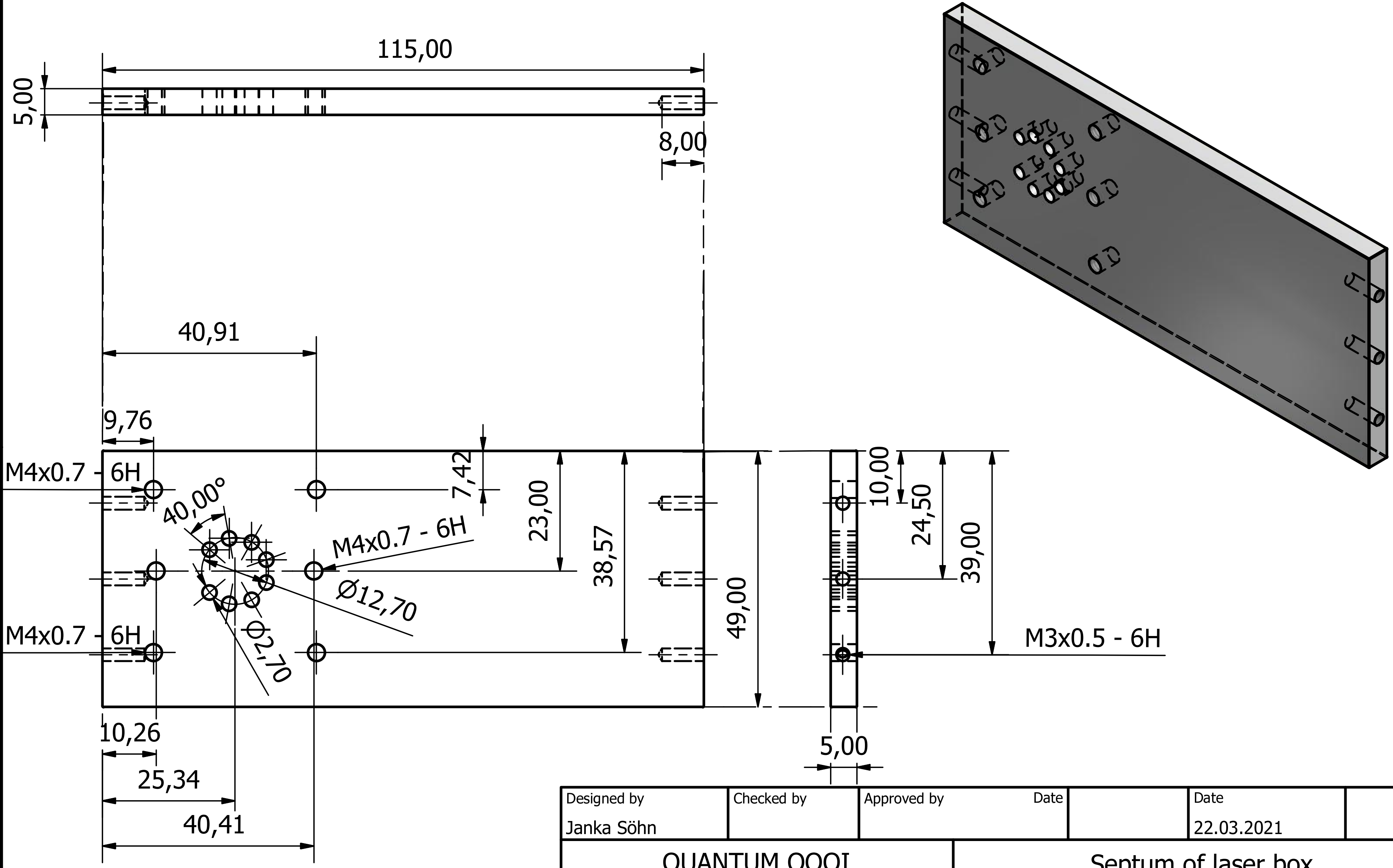

Designed by	Checked by	Approved by	Date	Date
Janka Söhn				22.03.2021

QUANTUM QOQI
Johannes-Gutenberg-Universität
Mainz

Septum of laser box

LaserboxSeptum

Edition

Sheet
1 / 1

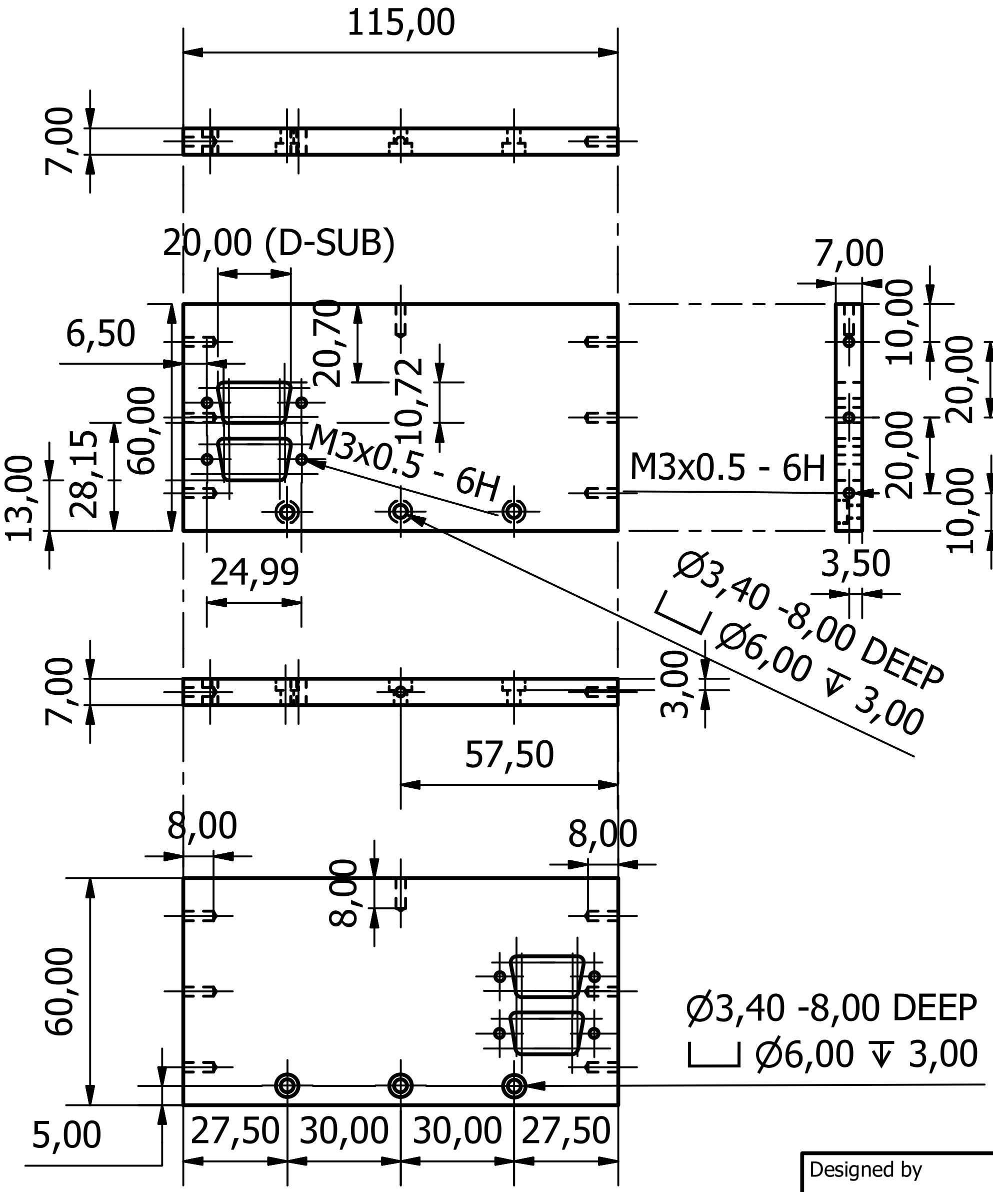

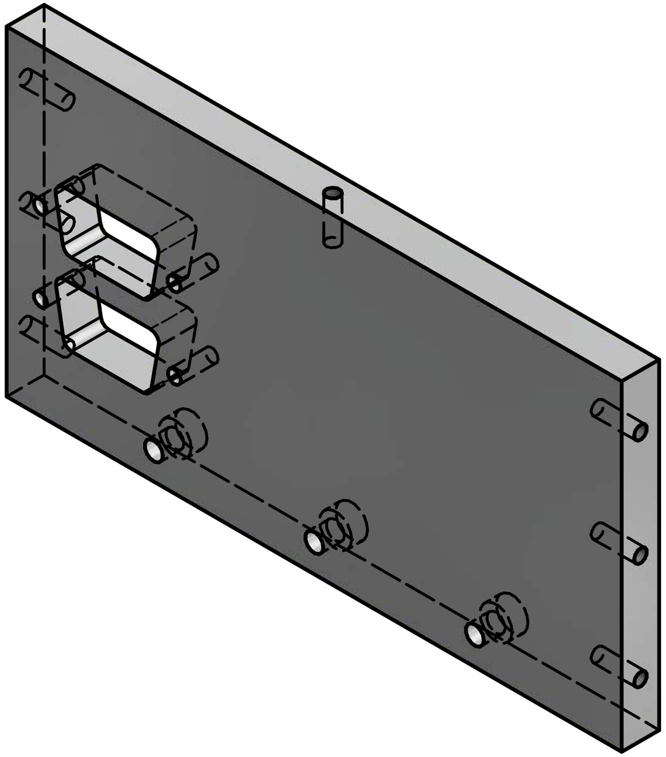

Designed by	Checked by	Approved by	Date	Date	
Janka Söhn				19.03.2021	

QUANTUM QOQI Johannes-Gutenberg-Universität Mainz	Wall 1 of laser box		
	LaserboxWall1	Edition	Sheet 1 / 1

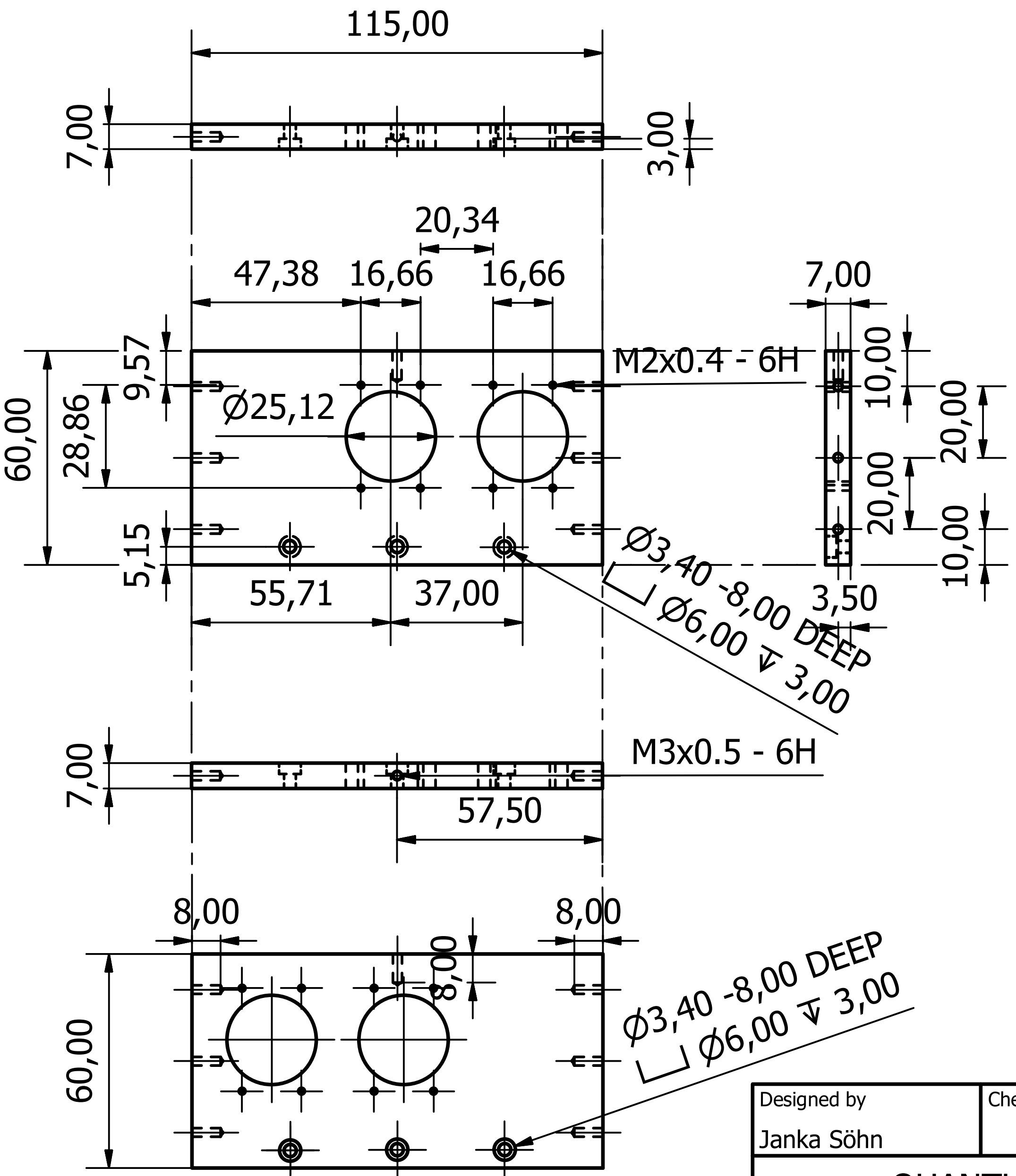

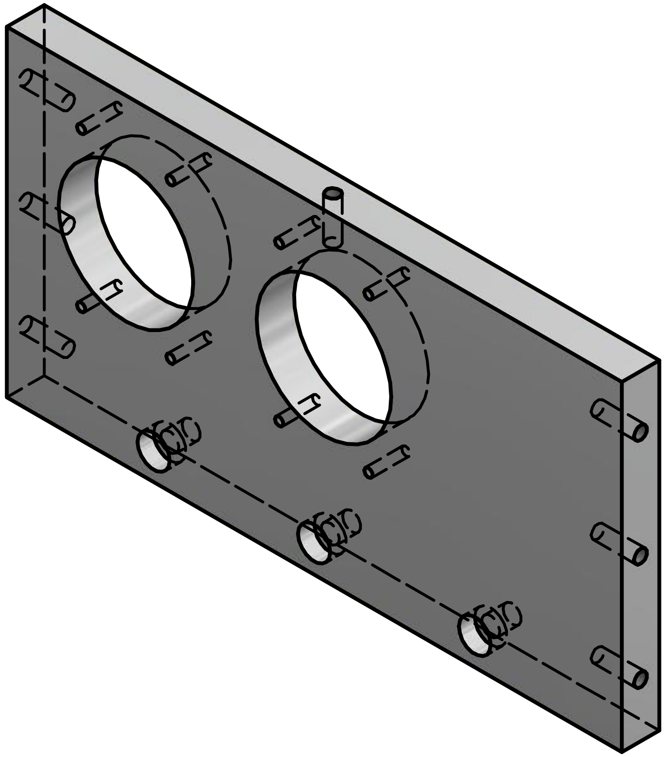

Designed by	Checked by	Approved by	Date	Date
Janka Söhn				19.03.2021

QUANTUM QOQI
Johannes-Gutenberg-Universität
Mainz

Wall 2 of laser box

LaserboxWall2

Edition

Sheet
1 / 1

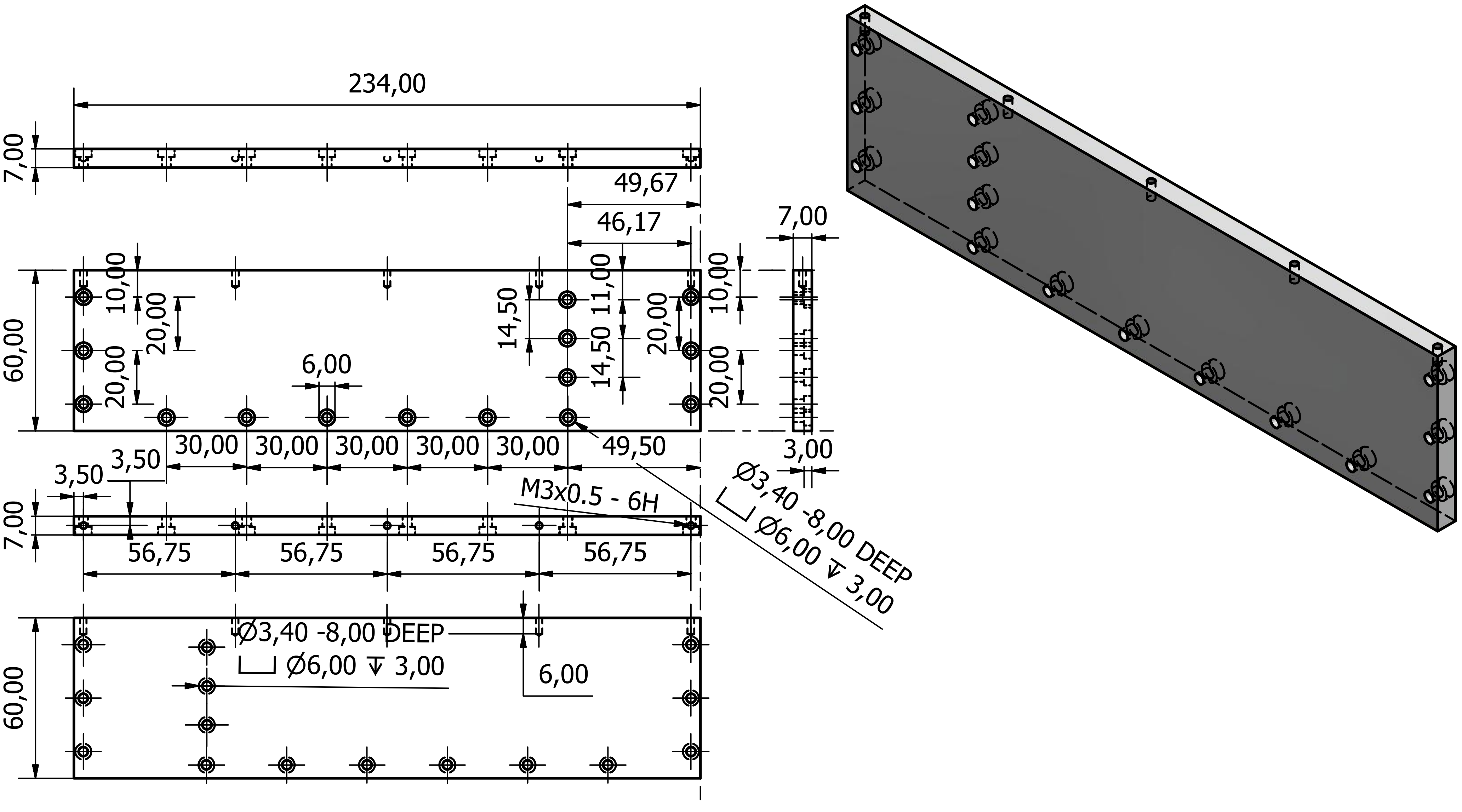

Designed by Janka Söhn	Checked by	Approved by	Date	Date 19.03.2021	
QUANTUM QOQI Johannes-Gutenberg-Universität Mainz			Wall 3 of laser box		
			LaserboxWall3	Edition	Sheet 1 / 1

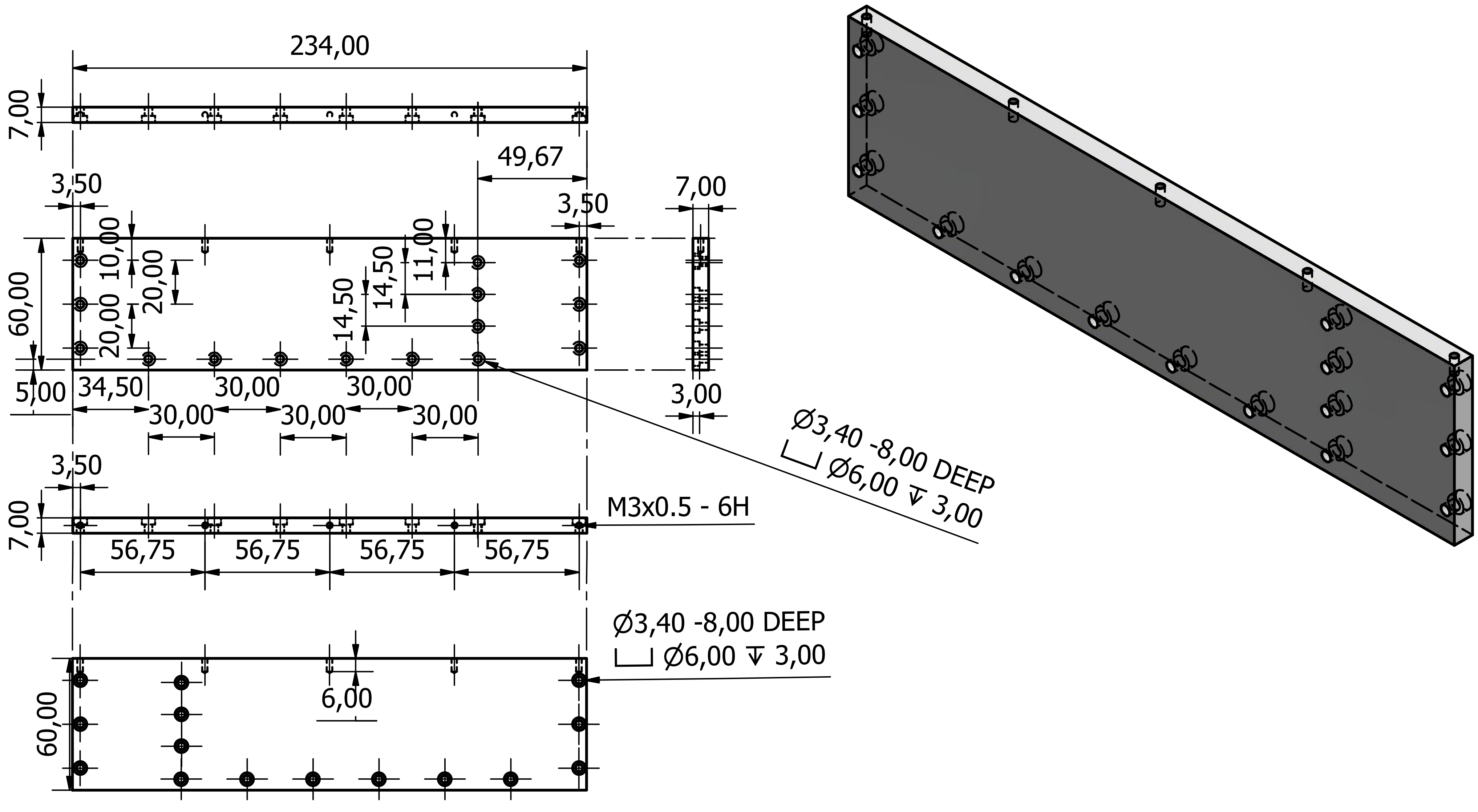

Designed by	Checked by	Approved by	Date	Date
Janka Söhn				19.03.2021

QUANTUM QOQI
Johannes-Gutenberg-Universität
Mainz

Wall 4 of laser box

LaserboxWall4

Edition

Sheet
1 / 1

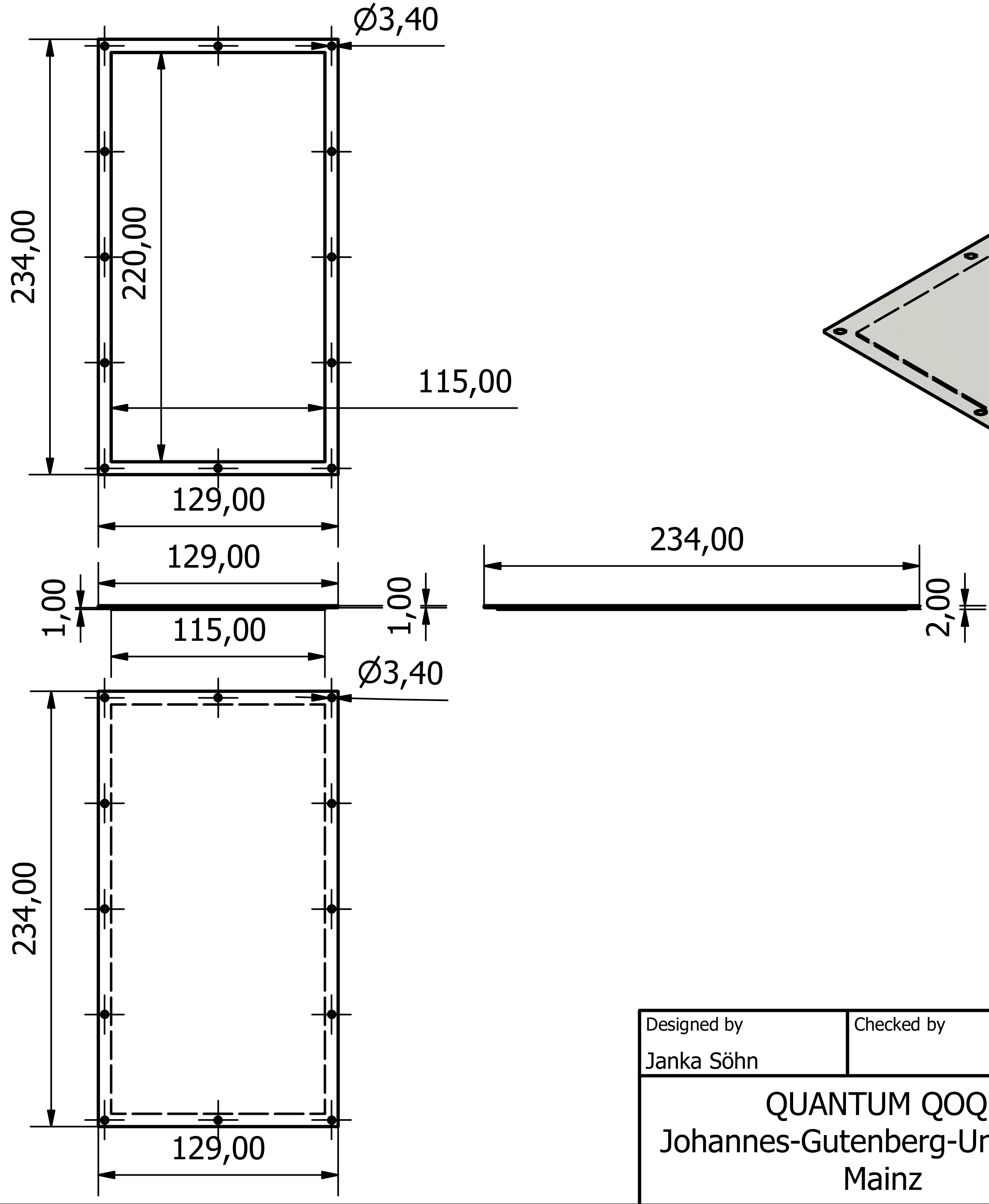

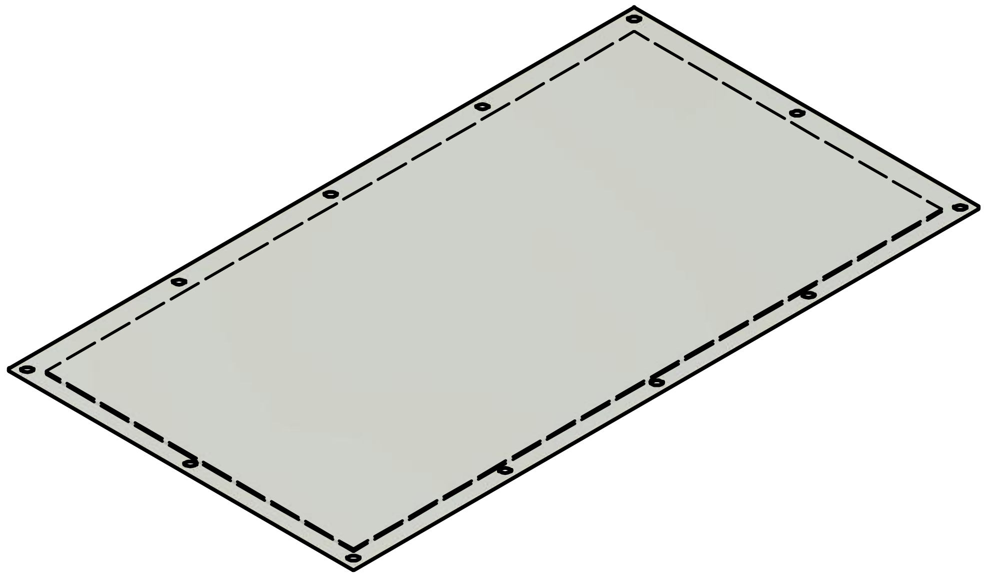

Designed by	Checked by	Approved by	Date		Date	
Janka Söhn					19.03.2021	

QUANTUM QOQI
Johannes-Gutenberg-Universität
Mainz

Lid of laser box

LidLaserboxF

Edition	Sheet
	1 / 1

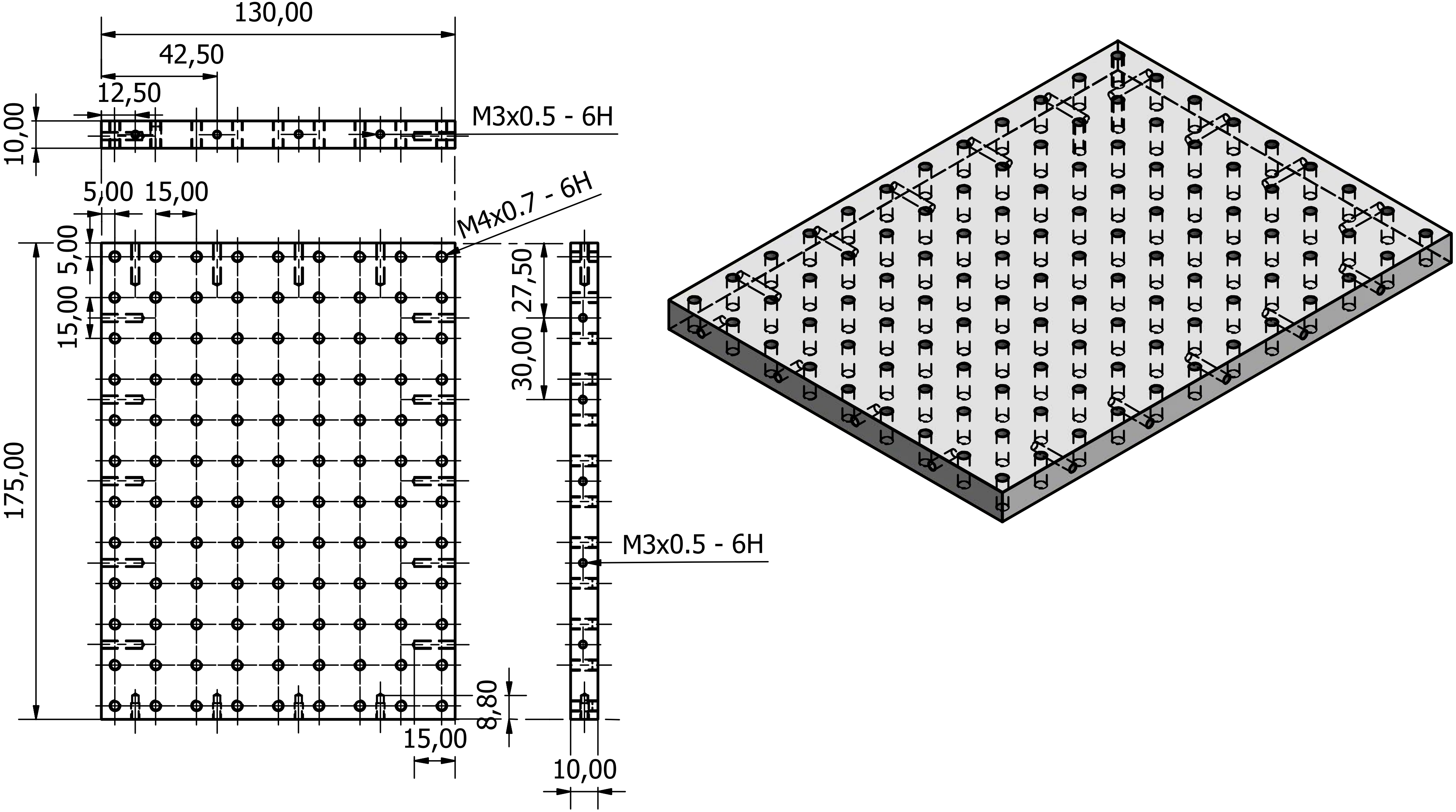

Designed by	Checked by	Approved by	Date	Date
Janka Söhn				22.03.2021

QUANTUM QOQI
Johannes-Gutenberg-Universität
Mainz

Baseplate of spectroscopy box

	Edition	Sheet
BaseplateSpektropart		1 / 1

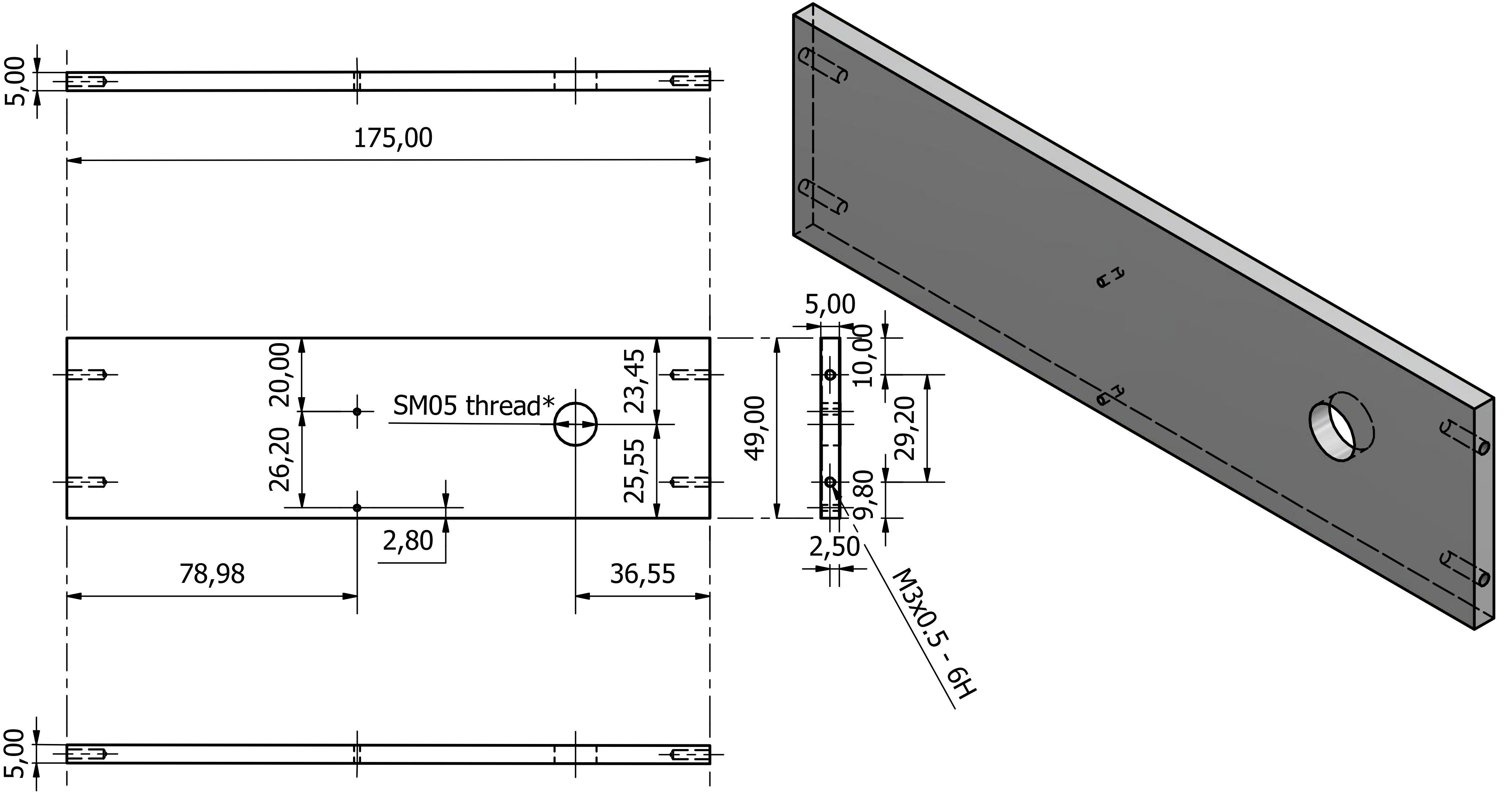

Designed by Janka Söhn	Checked by	Approved by	Date		Date 19.03.2021	*not yet implemented

QUANTUM QOQI
Johannes-Gutenberg-Universität
Mainz

Septum of spectroscopy box

SpektroboxSeptum	Edition	Sheet 1 / 1

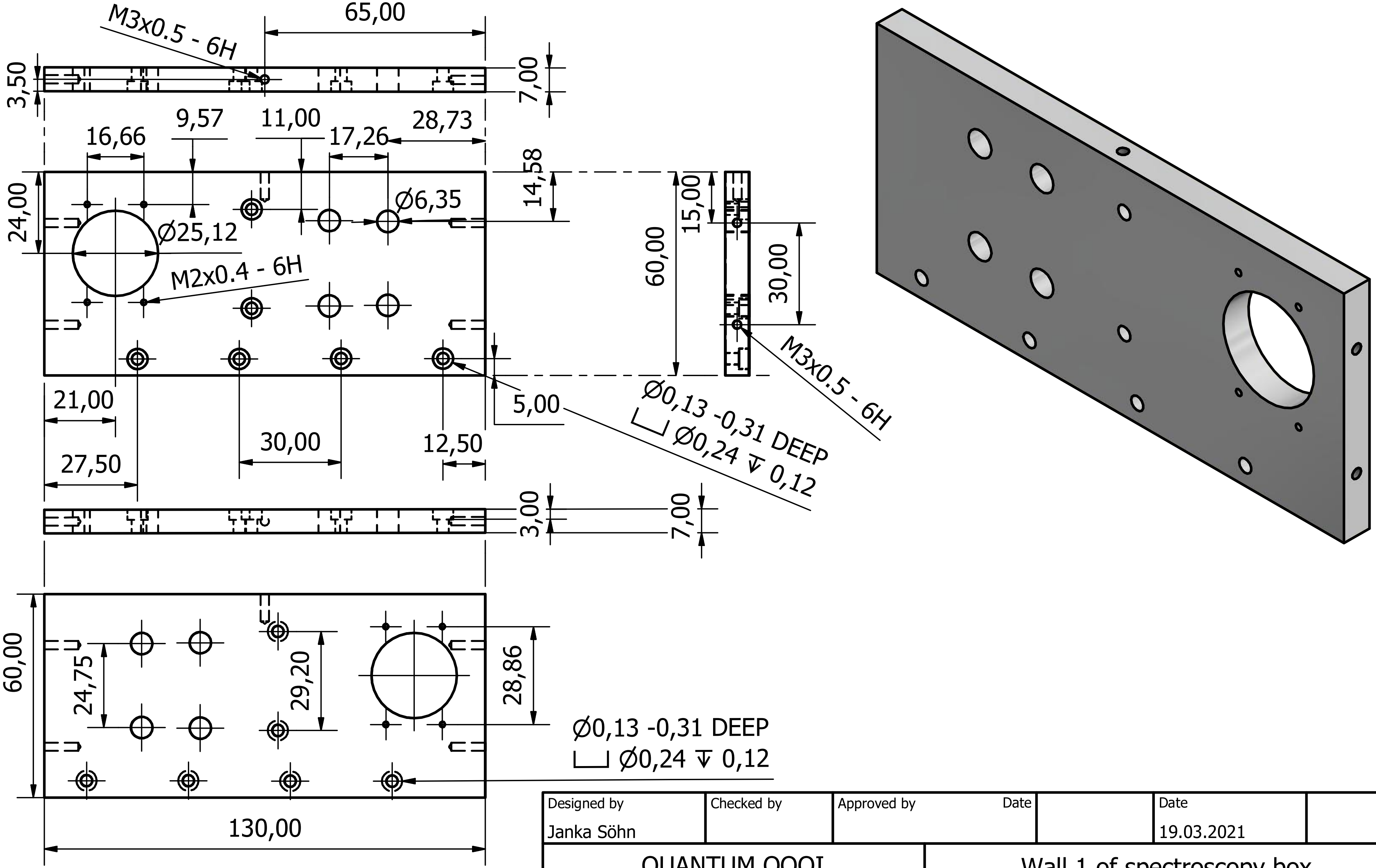

Designed by Janka Söhn	Checked by	Approved by	Date		Date 19.03.2021
QUANTUM QOQI Johannes-Gutenberg-Universität Mainz			Wall 1 of spectroscopy box		
			SpektroboxWall1	Edition	Sheet 1 / 1

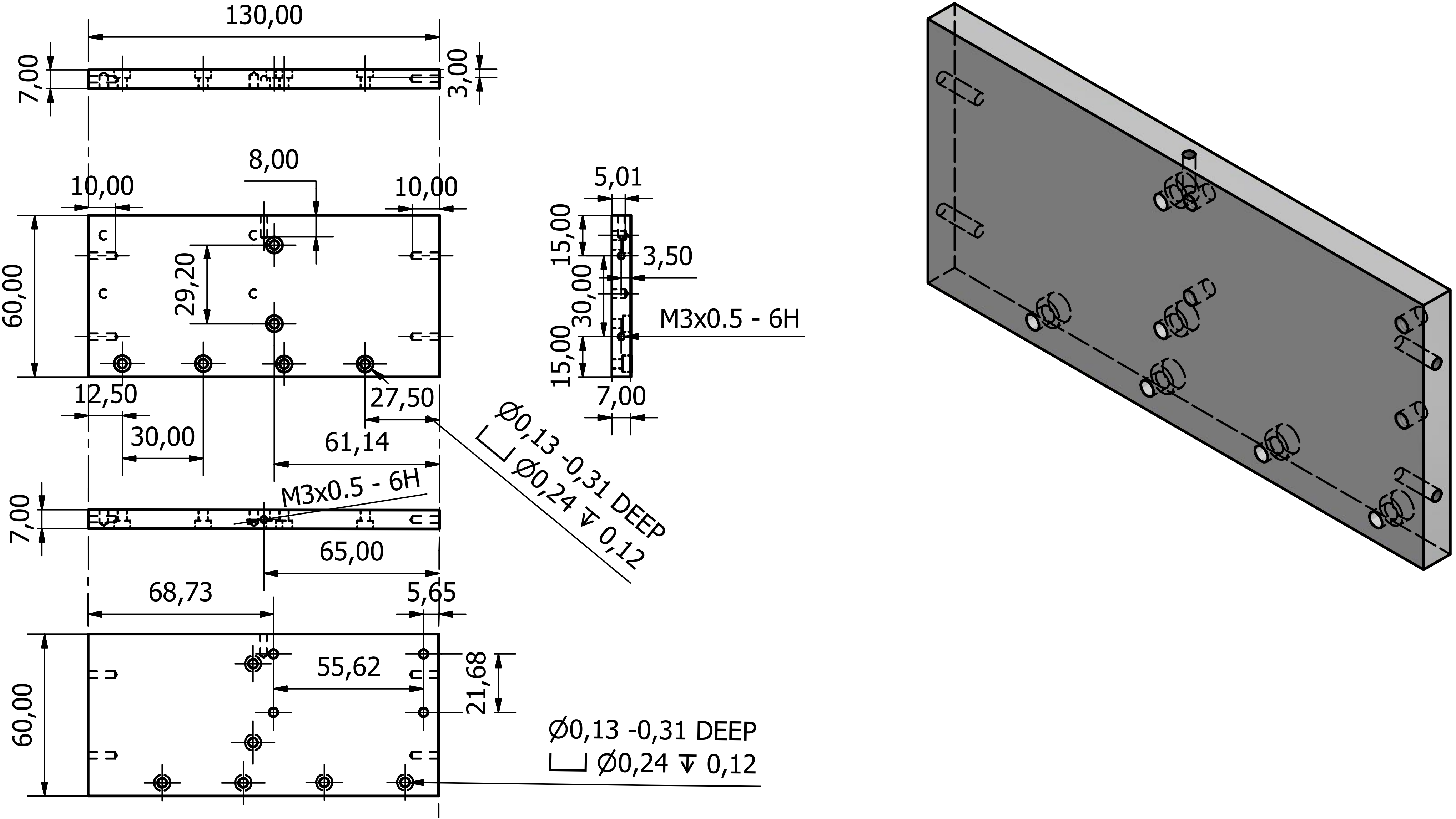

Designed by Janka Söhn	Checked by	Approved by	Date	Date 19.03.2021	
QUANTUM QOQI Johannes-Gutenberg-Universität Mainz			Wall 2 of spectroscopy box		
			SpektroboxWall2	Edition	Sheet 1 / 1

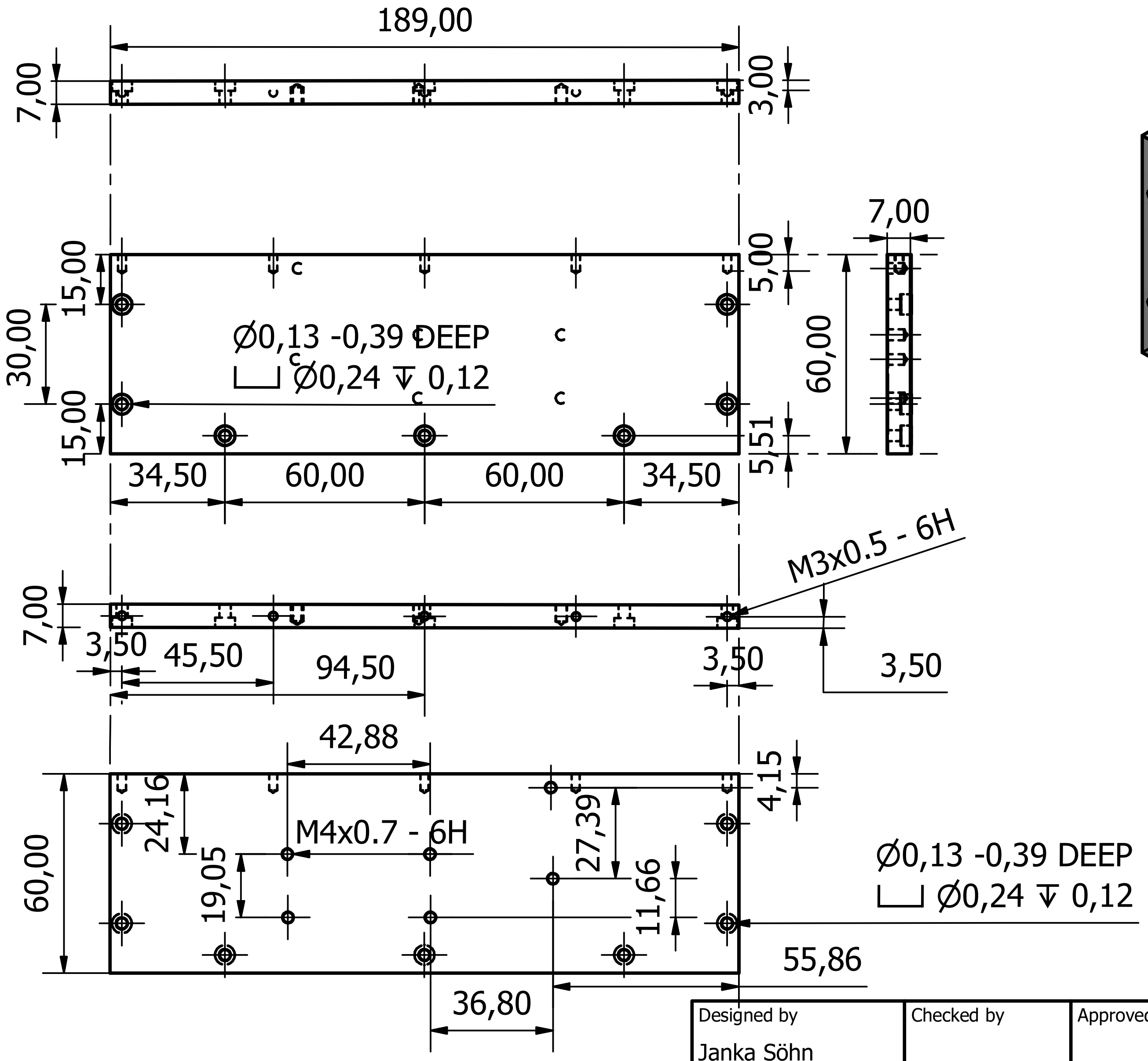

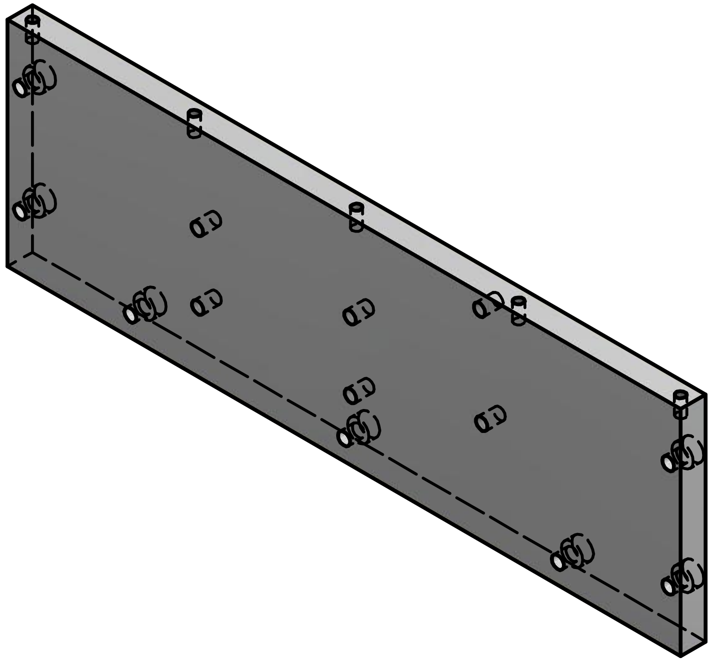

Designed by Janka Söhn	Checked by	Approved by	Date	Date 19.03.2021

QUANTUM QOQI
Johannes-Gutenberg-Universität
Mainz

Wall 3 of spectroscopy box

SpektroboxWall3

Edition

Sheet
1 / 1

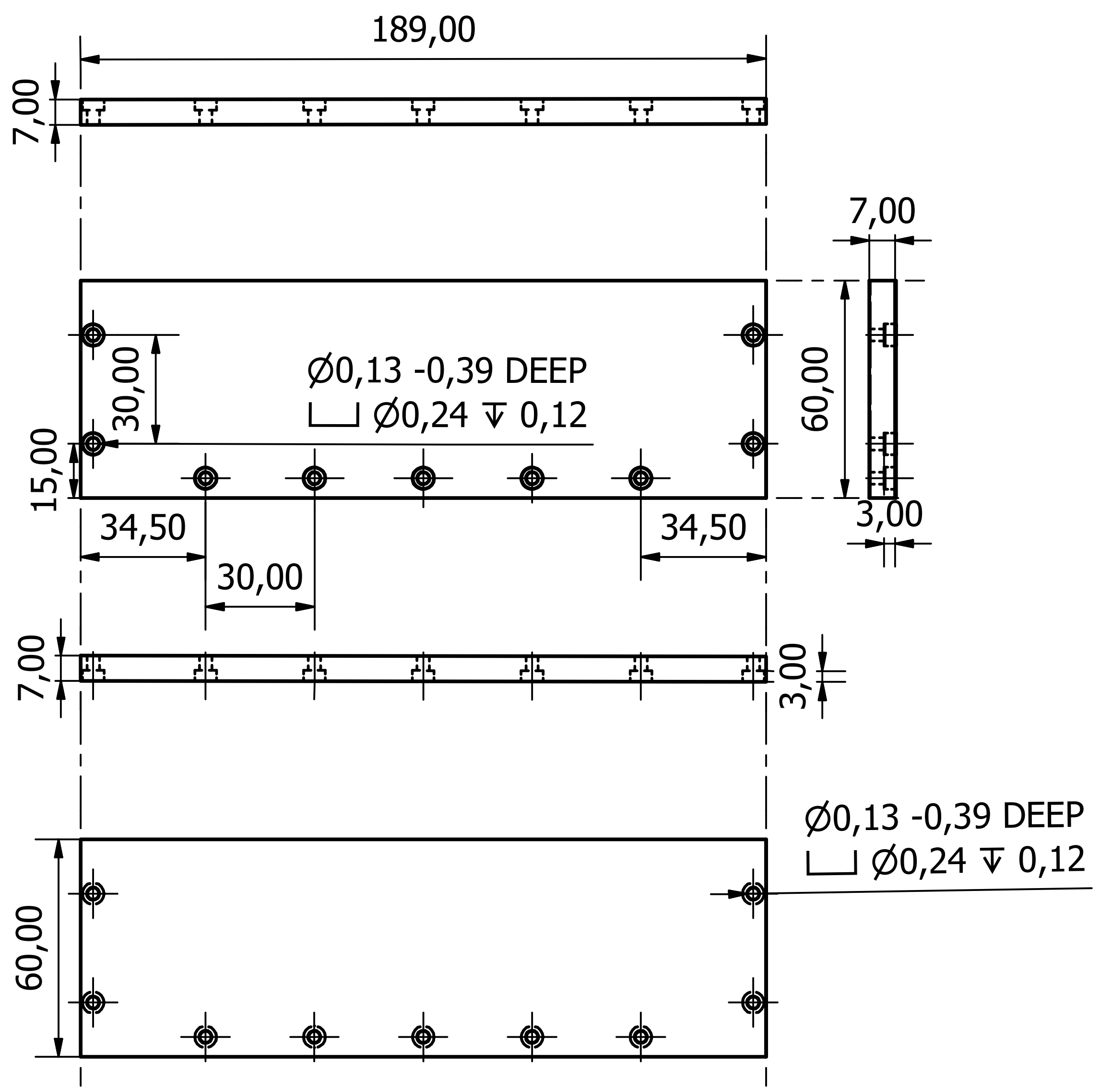

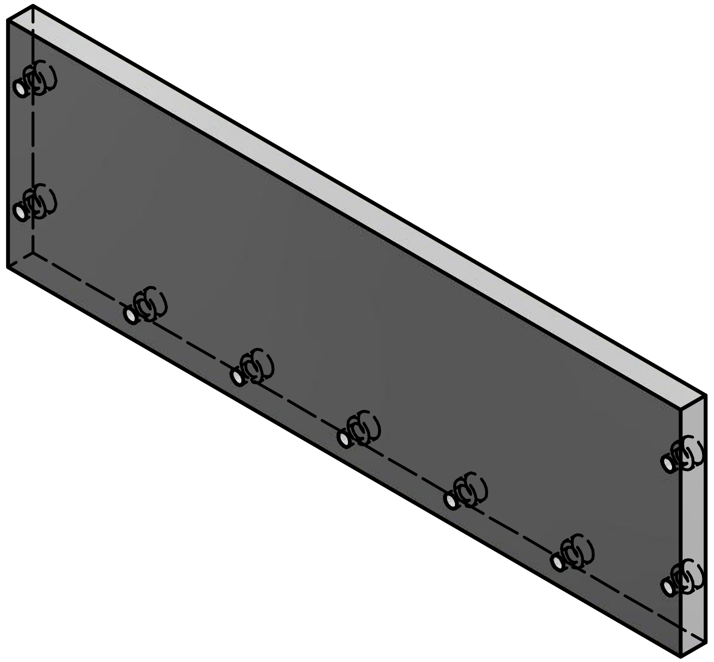

Designed by	Checked by	Approved by	Date		Date	
jsoehn					19.03.2021	

SpektroboxWall4	Edition	Sheet 1 / 1

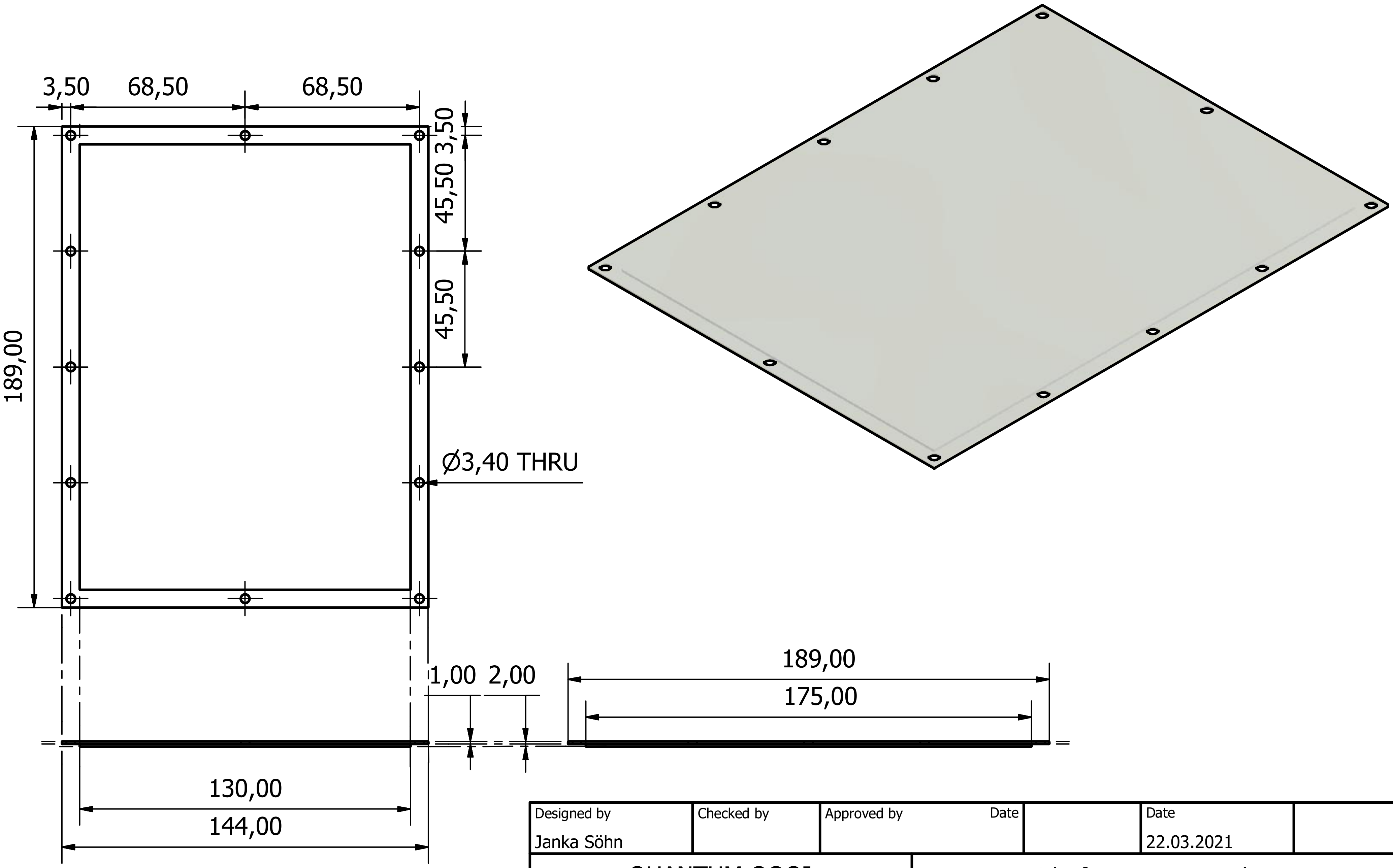

Designed by	Checked by	Approved by	Date	Date	
Janka Söhn				22.03.2021	

QUANTUM QOQI Johannes-Gutenberg-Universität Mainz	Lid of spectroscopy box		
	lidSpektro	Edition	Sheet 1 / 1

References

[1] S.B. Koller et. al.
Transportable optical lattice clock with 7×10^{-17} uncertainty.
Physical Review Letters, 118(073601), 2017.

[2] Hannes Duncker, Ortwin Hellmig, André Wenzlawski, Alexander Grote, Amir Jones Rafipoor, Mona Rafipoor, Klaus Sengstock, and Patrick Windpassinger.
Ultrastable, zerodur-based optical benches for quantum gas experiments.
Appl. Opt., 53(20):4468–4474, 2014.

[3] University of bremen, quantus iv - maius.
`https://www.zarm.uni-bremen.de/research/space-technologies/space-system-design-and-technologies/projects/quantus-iv-maius.html`.
Accessed: 2021-03-22.

[4] W. Demtröder.
Experimentalphysik 3: Atome, Moleküle und Festkörper.
Springer Spectrum, 2018.

[5] External cavity diode lasers (ecdl).
`https://www.newport.com/n/new-focus-tunable-lasers`.
Accessed: 2021-03-11.

[6] Michael G. Littman and Harold J. Metcalf.
Spectrally narrow pulsed dye laser without beam expander.
Appl. Opt., 17(14):2224–2227, 1978.

[7] Tunable diode lasers.
Toptica Photonics, 01(R-199-68A), 2017.

[8] Meena Dasan, Fredy Francis, Kundil Sarath, Elambilayi Dipin, and Talabattula Srinivas.
Optically Multiplexed Systems: Wavelength Division Multiplexing.
2019.

[9] W. Nakwaski B. Mroziewicz, M. Bugajski.
Physics of Semiconductor Lasers.
1991.

[10] J. Whiteaway J. Carroll and D. Plumb.
Distributed feedback semiconductor lasers.
IEE Circuits, Devices and Systems Series 10, 1998.

[11] Toptica Photonics.
Tunable diode lasers - br-199-68a.
`https://www.toptica.com/fileadmin/Editors_English/11_brochures_datasheets/01_brochures/toptica_BR_Scientific_Lasers.pdf`, 2017.
Accessed: 2021-02-16.

[12] Selection rules and transition moment integral.
`https://chem.libretexts.org/Bookshelves/Physical_and_Theoretical_Chemistry_Textbook_Maps/Supplemental_Modules_$%$28Physical_and_Theoretical_Chemistry$%$29/Spectroscopy/Fundamentals_of_Spectroscopy/Selection_rules_and_transition_moment_integral`.
Accessed: 2021-01-24.

[13] M. S. Dresselhaus.
Applications of group theory to the physics of solids.
`http://web.mit.edu/course/6/6.734j/www/group-full02.pdf`, 2002.
Accessed: 2021-02-16.

[14] Daniel A. Steck.
Rubidium 85 d line data.
(revision 2.2.1, 21 November 2019), 2001.

[15] Daniel A. Steck.
Rubidium 87 d line data.
(revision 2.2.1, 21 November 2019), 2001.

[16] W. Demtröder.
Laser Spectroscopy 1 & 2: Basic Principles/Experimental Techniques.
Springer Spektrum, 2013.

[17] Brad E. Schultz.
Measurement of the rubidium D2 natural transition linewidth.
`https://ui.adsabs.harvard.edu/abs/2010PhDT.......145S`, 2010.
Accessed: 2021-03-26.

[18] Prof. J. Brandenberger.
Doppler-free spectroscopy.
MIT Department of Physics, 2012.

[19] W. Demtröder.
Experimentalphysik 1: Mechanik und Wärme.
Springer, 2018.

[20] University of Florida — Department of Physics PHY4803L — Advanced Physics Laboratory.
Saturated absorption spectroscopy (experiment sas).
`http://www.phys.ufl.edu/courses/phy4803L/group_III/sat_absorbtion/SatAbs.pdf`, 2020.
Acsessed:2021-01-19.

[21] Vasant Natarajan Ayan Banerjee.
Saturated-absorption spectroscopy: Eliminating crossover resonances using co-propagating beams.
Department of Physics, Indian Institute of Science, Bangalore.

[22] Robert F. Enscoe and Richard J. Kocka.
Electro-optic modulation: Systems and applications.
`https://www.conoptics.com/wp-content/uploads/2013/09/Accessories_Technical-Data.pdf`.
Accessed: 2021-01-29.

[23] G. C. Bjorklund et al.
Frequency modulation (fm) spectroscopy.
Applied Physics, (32):145–152, 1983.

[24] W. Lenth J. M. Supplee, E. A. Whittaker.
Theoretical description of frequency-modulation and wavelength modulation spectroscopy.
Applied Optics, 33(27):6294–6302, 1994.

[25] Tim Wescott.
Pid without a phd.
EE Times-India, 2000.

[26] Gregory Chong Kiam Heong Ang and Yun Li.
Pid control system analysis, design, and technology.
IEEE Transactions on Control Systems Technology, 13(4):559–576, 2005.

[27] rp photonics.
Pockels cells.
`https://www.rp-photonics.com/pockels_cells.html`.
Accessed: 2021-01-26.

[28] rp photonics.
Electro-optic effect.
`https://www.rp-photonics.com/electro_optic_effect.html`.
Accessed: 2021-01-26.
.

[29] ixblue-nir-mpx800 series.
`https://photonics.ixblue.com/sites/default/files/2021-02/NIR-MPX800-LN$%$20SERIES_6.pdf`.
Accessed: 2021-03-21.

[30] rp photonics.
Electro-optic modulators.
`https://www.rp-photonics.com/electro_optic_modulators.html`.
Accessed: 2021-01-26.

[31] D. J. McCarron et. al.
Modulation transfer spectroscopy in atomic rubidium.
Measurement Science and Technology, 19(105601), 2008.

[32] Bin Wu et. al.
Modulation transfer spectroscopy for d1 transition line of rubidium.
Journal of the Optical Society of America, 35(11):2705–2710, 2018.

[33] Gary W. Johnson.
Wideband bias tee.
`http://wb9jps.com/Gary_Johnson/Bias_Tee_files/Bias_Tee_Design_V2R.pdf`, 2008.
Accessed: 2021-02-16.

[34] APEX Microtechnology.
Datasheet ms03.
`https://www.apexanalog.com/resources/mechdrawings/ms03.pdf`, 2013.
Accessed: 2021-03-19.